

An Assessment of FeOF as Cathode Material for Fluoride-Ion Batteries

Expanding the Horizons of Sustainable Energy Storage

MS53035: Master Project

Paulus Johannes Maria Breed

An Assessment of FeOF as Cathode Material for Fluoride-Ion Batteries

Expanding the Horizons of
Sustainable Energy Storage

by

Paulus Johannes Maria Breed

to obtain the degree of Master of Science
at the Delft University of Technology,
to be defended publicly on Monday July 24, 2023 at 9:00 AM.

Student number: 4655966
Project duration: September, 2022 - July, 2023
Thesis committee: Dr. P. Braga Groszewicz, TU Delft, Daily supervisor
Dr. Y. Gonzalez-Garcia, TU Delft, Faculty supervisor
Dr. Peyman Taheri, TU Delft, Committee member
Faculty: Faculty of Mechanical, Maritime and
Materials Engineering (3mE), Delft

Cover: <https://rmi.org/insight/breakthrough-batteries/>

An electronic version of this thesis is available at <http://repository.tudelft.nl/>.

Acknowledgements

Of everyone I mention here, I want to thank Pedro the most. Not only did he introduce me to this topic, he guided me from start to finish, trying (and succeeding) to teach me something during every meeting we had. The attention, involvement and investment he made can not only be attributed to his amazing skills as a supervisor but also to a wonderful personality that was exactly what I needed during this project.

I would also like to thank Yaiza, mostly for her helicopter view over the whole project. Busy as she is, we had time for in-depth meetings where she observed specifics or details that I overlooked.

Furthermore, I would like to thank Robert and Michel for their never-ending help with the X-ray diffraction, constantly replacing the monochromator, and giving me tips on how to improve the measurements. And the same for Frans and Esther, helping me to set up the experiments and their ability to pull any needed equipment and materials straight from their sleeves when needed.

I want to thank my mum, dad and sister for listening whenever I found out something new, and enthusiastically told them about the next steps I would make with this. But also for listening to the mistakes and misfortunes that occurred during the whole process.

Also don't forget my friends: Robert, Elena and Laura who were with me most of the time in the Tubalkain room. Distracting me when I tried to work on my research, providing me with the much-needed fun and breaks that I needed during my work.

Finally, I would like to thank Peyman Taheri for taking the time to read my report during these sunny summer days and to attend the defence as a committee member.

*Paulus Johannes Maria Breed
Delft, July 2023*

Summary

This study aims to assess the suitability of iron oxyfluoride (FeOF) as cathode material for fluoride-ion batteries based on the electrochemical performance and fluorination capability of ferrous oxide (FeO), as well as the defluorination of FeOF. Due to the pressing demand for electrochemical storage, alternatives to the widespread lithium-ion battery must be sought. One alternative can be the fluoride-ion battery (FIB). By trying to combine the stability of intercalation-based electrode materials and the high energy density of conversion-based materials, oxyfluorides might be the answer, especially if based on an abundant transition metal such as iron. In this report, the suitability of iron oxyfluoride as cathode material was evaluated. This was done by synthesising the electrode composites, evaluating their performance in a custom-made electrochemical cell and investigating the phase transitions of the researched materials. It was found that the ferrous oxide could not be fluorinated in an electrochemical environment and only reached a capacity of 0.75 mAh/g, which is equal to 0.2% of the theoretical capacity. It was also found that the iron oxyfluoride could not be electrochemically defluorinated. Therefore it is concluded that iron oxyfluoride is not suitable as cathode material for fluoride ion batteries.

Keywords: fluoride ion battery, iron oxyfluoride, ferrous oxide, electrode material

Contents

Preface	i
Summary	ii
Nomenclature	ix
1 Introduction	1
2 State of the Art	3
2.1 Battery Concept	3
2.2 Lithium-ion Battery Limitations	5
2.3 Anion-Shuttle Batteries	6
2.4 Fluoride Ion Battery	7
2.5 Fluoride Ion Battery Electrolytes	8
2.6 Anode Materials	9
2.7 Intercalation Cathode Materials	9
2.8 Conversion Cathode Materials	12
2.9 Objective	15
3 Methodology	16
3.1 Pb/PbF ₂ Composite	16
3.2 Ball Milling	16
3.3 Electrolyte Synthesis	17
3.4 FeO Composite	19
3.5 Scanning Electron Microscopy	20
3.6 Iron Oxyfluoride Synthesis	21
3.7 Cell Fabrication	21
3.8 Electrochemical Impedance Spectroscopy	23
3.9 Galvanostatic Charging and Discharging	24
3.10 X-Ray Diffraction	26
4 Results & Discussion	28
4.1 Materials and Synthesis	28
4.1.1 Pb/PbF ₂ Composite and Precursors	28
4.1.2 Electrolyte	31
4.1.3 FeO Composites and Precursors	34
4.2 Electrochemical Performance	39
4.2.1 Symmetrical PbF ₂ Anode	39
4.2.2 PK10 Electrolyte	43
4.2.3 FeO Cathode	45
4.3 Iron Oxyfluoride	47
4.3.1 FeOF Cathode Synthesis	47
4.3.2 FeOF Electrochemical Performance	49
5 Conclusion	52
5.1 Conclusion	52
5.2 Recommendations	53
References	54
A Extra Data	58
A.1 PK10 data	58
A.2 FeO Precursor Data	59

A.3 Pb/PbF ₂ symmetric cells	59
A.4 PK10 Performance	60
B Experimental Method	61
B.1 Electrolyte	61
B.2 FeO Composite	62
B.3 Pb/PbF ₂ Composite	62
B.4 FeOF Composite	63
B.5 Symmetrical Cells	63
B.6 FeO Cells	64
B.7 FeOF Cells	64

List of Figures

2.1	Representation of a battery (Daniell cell) showing the key features of battery operation. Reproduced from [6]	3
2.2	Typical discharge curve of a battery, showing the influence of the various types of polarization. Reproduced from [6]	4
2.3	Simplified Ragone plot of the energy storage domains for the various electrochemical energy conversion systems compared to an internal combustion engine and conventional capacitors. Reproduced from [6]	5
2.4	Timeline of the development of anion-shuttle-based batteries. PC, EC, and DEC represent propylene carbonate, ethylene carbonate, and diethyl carbonate, respectively. Reproduced from [13]	6
2.5	Comparison of theoretical volumetric and gravimetric energy density of different battery technologies. Reproduced from [13]	7
2.6	Electrochemical stability window of the PK10 electrolyte vs PbPbF_2 and the phase equilibria. Reproduced from [21]	9
2.7	K_2NiF_4 type structure of LaSrMnO_4 (left) in comparison to partly fluorinated $\text{LaSrMnO}_4\text{F}$ (middle) and fully fluorinated $\text{LaSrMnO}_4\text{F}_2$ (right). Reproduced from [32]	10
2.8	Schematic illustration of the volume changes and phase transition models during the charging process for (a) $\text{LaSrMnO}_4\text{F}$ and (b) $\text{Sr}_2\text{MnO}_3\text{F}_2$. Reproduced from [40]	11
2.9	Various models for the fluorination of ReO_3 that are considered throughout the text with Re shown in red, oxygen in orange, and fluorine in blue. Reproduced from [41]	11
2.10	Schematic of the proposed mechanism for the fluorination of the starting Bi powder presenting an oxidized surface. Reproduced from [45]	13
2.11	Discharge and charge curves of BiF_3 and BiF_3/C over the potential range between -2.0 and -0.3 V (vs. ref.) in the first cycle. Reproduced from [49]	13
2.12	Crystal structure of BFOF. Bi, Fe, F, and O atoms are represented as purple, blue, red, and green spheres, respectively. Reproduced from [51]	14
2.13	(a) Probable tetrahedral sites and (b) configurations for F intercalation. Reproduced from [5]	15
3.1	Illustration of the milling tools and the principle of operation of a planetary mill. The colored arrows indicate the counter-rotation of the supporting disk (rotd) and the milling beakers (rotb). Reproduced from [52]	17
3.2	Schematic representation of solid-state cell. a) Putting powdered PK10 solid-state electrolyte in cell b) press cell at 50 bar for 5 minutes	18
3.3	Schematic representation of a SEM setup. Reproduced from [56]	20
3.4	Schematic representation of solid-state cell containing all relevant components	21
3.5	Schematic representation of solid-state cell. a)-f) Steps of cell fabrication. g) Short-circuit induced by uneven electrode composite distribution. h) Short-circuit induced by misaligned charge collectors.	22
3.6	a) An equivalent circuit example of electrolyte. b) Nyquist plot of this system. c) Bode plot of this system. Reproduced from [60]	24
3.7	Representation of a voltage-capacity curve. Obtained during this project.	25
3.8	Schematic representation of XRD setup. Reproduced from [62]	26
3.9	Schematic representation of kapton film-covered XRD sample holder	27
4.1	Refinement of the XRD measurement of the lead powder precursor. The red bars indicate cubic lead, while green and purple indicate litharge and massicot respectively, polymorphs of PbO	28

4.2	Refinement of XRD measurement of the lead(II) fluoride precursor. Red bars indicate orthorhombic PbF_2 , green bars indicate the cubic polymorph: Fluorocronite	29
4.3	Refinement of XRD measurement of the first synthesis of the Pb/PbF ₂ composite. Red indicates metallic lead, blue the PK10 solid-state electrolyte, green orthorhombic PbF_2 and orange cubic PbF_2	30
4.4	XRD patterns of Different Batches PK10, synthesised and refined	31
4.5	SEM measurement of pressed PK10 electrolyte pellet, 750x zoom. The scale bar is 20 μm	33
4.6	SEM and EDS measurement of pressed PK10 electrolyte pellet	33
4.7	Refinement of XRD measurement of FeO, obtained from Thermo Fisher. Red bars indicate iron deficient FeO, green bars stoichiometric FeO, blue bars magnetite, Fe_3O_4 and orange bars metallic iron	34
4.8	SEM measurement of FeO, 750x zoom. The scale bar is 20 μm	35
4.9	SEM and EDS measurement of unmodified FeO	35
4.10	X-ray diffraction measurement of electrode composite with FeO, obtained from Thermo Fisher. Red and blue bars indicate the PK10 electrolyte, green bars FeO, and purple bars the PbF_2	36
4.11	Refinement of XRD measurement of electrode composite with FeO obtained from Merck, Red and blue bars indicate the PK10 electrolyte, purple the FeO, green the Fe_3O_4 and lime the α -iron	37
4.12	SEM measurement of FeO composite with Thermo Fisher, 800x zoom. The scale bar is 20 μm	37
4.13	SEM measurement of ball-milled FeO composite with Thermo Fisher, 1300x zoom. The scale bar is 10 μm	38
4.14	Phase diagram of FeO. Reproduced from [65].	38
4.15	Voltage-capacity curve of the discharge of the Pb/PbF ₂ :PK10:Pb/PbF ₂ cells	40
4.16	Refinement of top electrode composites of symmetric Pb/PbF ₂ :PK10:Pb/PbF ₂ cell 4	40
4.17	Refinement of XRD measurement of the bottom electrode composite of symmetric Pb/PbF ₂ :PK10:Pb/PbF ₂ cell 4	41
4.18	Refinement of XRD measurement of the top electrode composites of symmetric Pb/PbF ₂ :PK10:Pb/PbF ₂ cell 3. With red bars being PK10, blue metallic lead, green orthorhombic PbF_2 and orange cubic PbF_2	42
4.19	Refinement of XRD measurement of the bottom electrode composites of symmetric Pb/PbF ₂ :PK10:Pb/PbF ₂ cell 3. With red bars being PK10, blue metallic lead, green orthorhombic PbF_2 and orange cubic PbF_2	42
4.20	Voltage-capacity curve of the discharge of the ECC:PK10:Pb/PbF ₂ cells.	43
4.21	Refinement of XRD measurement of the bottom electrode (Pb/PbF ₂) of the ECC:PK10:Pb/PbF ₂ cells (combined spectrum). CsPbF_3 in red, PbF_2 in green.	44
4.22	Voltage-capacity curve of FeO 1 cell charged to 1.1V	45
4.23	Refinement of XRD measurement of the top FeO electrode of the FeO:PK10:Pb/PbF ₂ cell. Red indicated PK10, blue $\text{Fe}_{0.944}$, black metallic lead, and purple and pink respectively litharge and massicot.	46
4.24	Indexed XRD pattern of the FeOF synthesis. Red bars indicate unreacted FeF_3 , green bars indicate FeOF and pink indicates $\text{FeO}_{0.55}\text{F}_{2.667}$	47
4.25	XRD measurement of the FeOF synthesis according to Zhu et al. using FeF_3 . Red bars indicate reflexes of FeF_3 , blue bars indicate where the FeOF reflexes should have been	48
4.26	Refinement of XRD measurement of the FeOF synthesis according to Zhu et al. using $\text{FeF}_3 \cdot 3\text{H}_2\text{O}$. All reflexes belong to FeF_3	48
4.27	X-ray diffraction pattern characteristic for silica, SiO_2 . Reproduced from [69].	49
4.28	Voltage-capacity curve of FeOF, cut off at 1.8V and capacity of 0.0019 mAh	50
4.29	Voltage-capacity curve of reversed FeOF cell, cut off at 1.2V and capacity of 0.0019 mAh	50
4.30	Voltage-capacity curve of FeOF, cut off at 1.8V and capacity of 0.0019 mAh	51
4.31	Refinement of XRD measurement of top-electrode of FeOF cell. Red bars indicate the PK10 electrolyte, orange and blue PbO and green is metallic lead	51

A.1	Measured Nyquist plots of the PK10 measurements. The x-axis is the real impedance, the y-axis the imaginary impedance	58
A.2	X-ray diffraction measurement of FeO, obtained from Thermo Fisher using a Bruker diffractometer. Red bars indicate Fe _{0.91} O, blue bars FeO, green bars α-iron and purple Fe ₃ O ₄	59
A.3	Impedance measurements of Pb/PbF ₂ :PK10:Pb/PbF ₂ cell. a) Impedance before galvanostatic discharging. b) Impedance after galvanostatic discharging.	59
A.4	Impedance measurements of ECC:PK10:Pb/PbF ₂ cell	60

List of Tables

3.1	Overview of the properties of conversion cathode materials. Values are calculated using the formulas mentioned above and data from the Materials Project [54]	19
3.2	Overview of all prepared composites	20
3.3	Overview and description of all prepared cell types	22
4.1	Overview of the reflexes of metallic lead, litharge and massicot, indexed in figure 4.1	29
4.2	Overview of the reflexes of both polymorphs of PbF_2 , indexed in figure 4.2	30
4.3	Overview of the reflexes of CsPbF_3	32
4.4	Calculated ionic conductivity of the electrolyte in mS/cm per batch, including the experimentally obtained parameters	32
A.1	Rietveld refinement results of the synthesised $\text{CsPb}_{1-x}\text{K}_x\text{F}_{3-x}$ batches, excluding batch 5, no measurement was taken. Batch 1 was obtained from an earlier project.	58

Nomenclature

Abbreviations

Abbreviation	Definition
AIMD	Ab initio molecular dynamics
BIB	Bromine Ion Battery
C ₂ C ₁ im	1-ethyl-3-methylimidazolium
CE	Coulombic Efficiency
CIB	Chloride Ion Battery
CMK	Ordered Mesoporous Carbon
DFT	Density Function Theory
DIB	Dual Ion Battery
EC	Electrochemical Capacitor
EDL	Electrical Double Layer
ESW	Electrochemical Stability Window
EV	Electric Vehicle
FIB	Fluoride Ion Battery
FSB	Fluoride Shuttle Battery
G.I.C.	Graphite Intercalated Compound
ICL	Initial Capacity Loss
IHP	Inner Helmholtz Plane
LIB	Lithium-ion Battery
M13	Escherichia virus M13
MMT	Montmorillonite
NASA	National Aeronautics and Space Administration
NIB	Sodium Ion Battery
NMC	Nickel-Manganese-Cobalt
OER	Oxygen Evolution Reaction
OHP	Outer Helmholtz Plane
ORR	Oxygen Reduction Reaction
OXL	Oxalate
PDF	Pair distribution function
PDMS	polydimethylsiloxane
PEDOT	Poly(3,4-ethylenedioxythiophene)
PK10	CsPb _{0.9} K _{0.1} F _{2.9}
PP	Polypropylene
Primary Battery	Non-rechargeable Battery
SEI	Solid Electrolyte Interface
SEM	Scanning Electron Microscopy
Secondary Battery	Rechargeable Battery
S.H.E.	Standard Hydrogen Electrode
SIB	Sodium Ion Battery
SPAN	Sulfirized-polyacetonitrile
XANES	X-ray absorption near edge structure
XAS	X-ray absorption spectroscopy
XRD	X-ray diffraction

Symbols

Symbol	Definition	Unit
<i>A</i>	Ampere	C/s
<i>C</i>	Coulomb	A · s
<i>eV</i>	Electronvolt	$1.602 \cdot 10^{-19}$ J
<i>F</i>	Faraday Constant	96485 C/mol
<i>G</i>	Gibbs Free Energy	J
<i>I</i>	Current	A
<i>R</i>	Resistance	Ω
η	Polarisation	

Introduction

Over the past decades, our society saw a tremendous increase in both energy production and consumption. This allowed for the great advances made in both lifestyle and technology. While this has many advantages, the burning of fossil fuels, coupled with the ever-increasing population, has a disastrous effect on the climate. The greenhouse gasses released in this process contribute heavily to global warming and climate change, leading to a wide range of negative impacts on different communities all around the world due to an increase in severe weather events, rising sea levels, and causing a threat to food security. Also, the fossil fuel industry on itself does not have a future due to the depletion of these natural resources. Despite all this, the energy demand keeps increasing. Therefore, the global increase in demand for energy, coupled with the need to reduce greenhouse gas emissions to reach a sustainable future, has driven the need for green and renewable energy. However, where fossil fuels can match the energy supply directly with its demand, the intermittent nature of renewable energy makes this nearly impossible. Solar, wind, and tidal energy are not as predictable as coal, gas, and oil, and therefore there is a necessity of developing efficient and affordable energy storage. Only if this is achieved, a secure energy grid can be maintained.

One of the solutions for energy storage lies in the use of batteries. Battery storage systems can help balance the variable output of green energy, improving the reliability and resilience of the power grid all around the world. The role of batteries in the energy transition extends beyond the storage of renewable energy though. As oil and gas are gradually replaced, there is an alternative required as fuel for the whole transportation sector. To facilitate this, batteries are essential to the success of these electric vehicles(EVs). Over the past years, EVs have become increasingly popular as battery costs decline and performance improves, with many car manufacturers committing to phasing out internal combustion engines in favour of electric powertrains. As a result, the demand for EV batteries is growing rapidly. This is valid for batteries in general, their commercial demand has to be met, and the technology needs to be improved.

Currently, lithium-ion batteries(LIBs) are used for energy storage in a wide range of applications. This includes batteries for portable devices, EVs, and small-scale solar energy storage in households. The lithium resources required for those conventional batteries face challenges due to scarcity concerns, along with the cobalt which is used in the cathodes of said batteries. Because of this, alternative charge carriers are a solution to this problem. While the mass of recent research focuses on sodium-ion batteries (SIBs), magnesium-ion batteries(MIBs), and aluminium-ion batteries(AIBs), fluoride-ion batteries(FIBs) have emerged as an attractive alternative as well due to their favourable properties. This includes its monovalency, the small ionic radius, and a high reduction potential. All of this along with its abundance in minerals such as fluorite, CaF_2 . These batteries saw a surge of interest after a novel, fluoride-ion conducting solid-state electrolyte was discovered in 2011 [1]. This became even more relevant after the discovery of PK10 in 2022; a solid-state electrolyte that also functions properly at room temperature [2]. Despite this, practical challenges remain. These include issues such as low ionic conductivity of active materials, volume changes during charge-discharge cycles, and side reactions that cause performance degradation.

It was found that despite the different chemistry of fluoride compared to a lithium cation, similar transition metals have the potential to function as cathode material for FIBs. While historically mostly oxides have been used as intercalation materials for LIBs such as LiCoO_2 , conversion electrodes such as BiF_3 , CuF_2 and FeF_x have been tested over the past years. And results seem promising. When drawing

a parallel to the materials that have been tried and tested in LIBs, it is noticeable that this trend is similar for FIBs as well. While these metal fluorides show excellent capacity, due to their inherent expansion upon fluorination and defluorination, the cyclability of these materials is lacking, as rapid capacity loss is observed upon repeated charging and discharging (cycling). This is caused by the expansion and shrinkage of the solid-state materials, causing loss of contact in the internal components and amorphisation of the crystalline materials.

Therefore interest has gone out to using crystal structures that are focused not only on capacity but also stability. By using a specific type of perovskite structure, a Ruddlesden-Popper phase, several atoms in the crystal maintain the lattice structure upon (de)fluorination. One material that has been tested, is $\text{Sr}_3\text{Fe}_2\text{O}_5\text{F}_2$, an intercalation electrode material that is capable of retaining a capacity of 116.7 mAh/g for 70 cycles. While the stability is higher than that of metal fluorides, the capacity is too low for commercial applications [3]. Therefore alternatives were sought that balance a structurally sound framework, but also have sufficient capacity.

Metal oxyfluorides, also studied for lithium-ion batteries, would be the next logical step in the development of a proper FIB cathode material. Bismuth oxyfluoride and a related oxyfluoride of $\text{Bi}_7\text{O}_5\text{F}_{11}$ have shown promising results already, and Cu_2OF_2 has been demonstrated to yield a capacity of 174 mAh/g for 35 cycles [4, 5]. While these metal oxyfluorides seem promising, the high atomic weight of bismuth and the cost and environmental impact of copper might cause these materials to not be feasible on an economic scale. Therefore other transition metal oxyfluorides should be investigated.

That is why this research will be pioneering the assessment of iron oxyfluoride. By attempting to combine the high cycle life and stability of intercalation electrodes, and the high energy density of conversion electrodes, while also using more abundant and cheap materials, FeOF will be investigated as potential cathode material for fluoride ion batteries. This is done by evaluating the electrochemical performance and material characteristics to provide a thorough evaluation of the viability of this material. This assessment of iron oxyfluoride contributes to the development of sustainable and efficient energy storage by employing the abundance of iron and fluorine resources to support a greener future.

2.1. Battery Concept

Electrochemical batteries are a type of electrochemical energy storage. They use reduction and oxidation reactions to provide energy. They contain an anode, cathode and electrolyte. Oxidation occurs at the anode, and reduction occurs at the cathode. The electrolyte carries the ions between the two electrodes. It is important to note that batteries are closed systems: the cathode and anode actively participate in the redox reactions. This also means that energy storage and conversion occur in the same components. The battery depicted in figure 2.1, uses ions as charge carriers between the electrodes during operation. Compared to fuel cells, another form of electrochemical energy storage, these ions are not hydroxides or protons, but metal ions. The electrolyte between the cathode and anode is present to conduct the ions involved in the reactions and prevent short-circuiting.

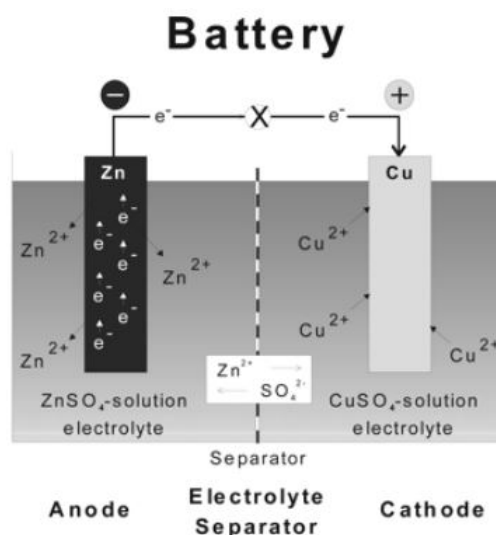


Figure 2.1: Representation of a battery (Daniell cell) showing the key features of battery operation. Reproduced from [6]

The electrolyte is generally a liquid, but can also be a solid ion conductor. It is important that this compound is chemically stable during storage and operation. The voltage range in which the electrolyte can operate is the electrochemical stability window (ESW); exceeding this causes the battery to degrade and stop functioning properly. This limits the voltages at which the battery can be operated, reducing the possible redox combinations. The most interesting type of battery is rechargeable. Compared to primary batteries, secondary batteries must abide by more criteria and be engineered to be more robust and enduring than primary ones. This leads to a higher price and lower storage capabilities.

The amount of energy a battery can provide depends on the active mass, which is the material that will be chemically converted during the redox reactions. It also depends on the redox potential between the cathode and anode, and the number of electrons transferred, and on the internal resistance or impedance. The maximum energy a battery can release is found when looking at the thermodynamics of the system. The net useful energy available from a given reaction in the cell in electrical terms is

given by:

$$\Delta G = -nFE$$

Where n is the number of electrons transferred per mole of reactant, F is the Faraday constant in coulombs per mole, and E is the voltage of the cell. From there one can see that the available energy increases as the redox potential increases, and the number of transferred electrons increases. To increase the gravimetric energy density of a battery, the molecular weight of this active material should be as low as possible compared to the number of electrons available for the reaction. This is better shown in the equation for the specific energy of the cell [7]:

$$\text{Specific energy} = \frac{\text{Voltage}(V) \times \text{Capacity}(Ah)}{\text{Weight}(kg)}$$

Battery function is also dependent on polarisation effects. It reduces the operation voltage and with that the energy that is available for usage. There are three types as depicted in figure 2.2: activation polarisation related to interfacial reactions at the electrode/electrolyte interface. This potential difference is beyond the equilibrium value needed to generate a current. It is dependent on the activation energy of the redox reaction. The formula for this would be:

$$\eta = a - b \log\left(\frac{I}{I_0}\right)$$

Where a and b are constants, I is the current flow, and I_0 is the exchange current density which is material specific. Ohmic polarisation comes from the intrinsic resistance to the charge flow, which results in a voltage loss. There is a linear relation between the polarisation and the ohmic resistance with the current flow:

$$\eta = IR$$

There is also concentration polarisation. This arises from the mass transport limitations caused by limitations in diffusion. This happens as the active material runs out, and the reaction cannot be sustained properly. For limited diffusion the concentration polarisation can be expressed as:

$$\eta = \frac{RT}{n} \ln\left(\frac{C}{C_0}\right)$$

Where C is the concentration at the surface of the electrode, and C_0 is the bulk concentration. Considering all these kinetic effects is an integral part of understanding such a battery's life cycle. However, a proper battery is defined by other characteristics.

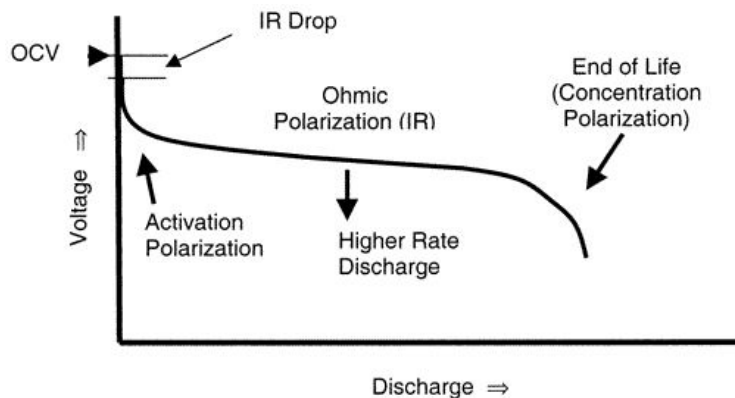


Figure 2.2: Typical discharge curve of a battery, showing the influence of the various types of polarization. Reproduced from [6]

To be viable for a particular application, a battery must supply a steady voltage over a long time while having a good energy density. But above all a battery must be stable. Safety is essential in every commercial product and should always be considered. Both mechanical and chemical stability are required, as the breakdown of the battery can cause significant problems especially if the casing is breached. The temperature also plays a role as lower temperatures generally give rise to higher internal

resistance and worse reaction kinetics. In the case of a liquid-based electrolyte battery, freezing might destroy the battery, while at higher temperatures the chemicals might decompose or give rise to side reactions. This can result in self-discharge, which is a criteria in itself too. Batteries slowly lose capacity when unused, an issue in various applications. Secondary batteries can also lose permanent capacity due to cycling. This is the act of charging and discharging the battery, which is considered worn-out when it has lost >20% of its initial capacity due to cycling. Therefore the cycle life is a significant factor in the lifespan of a battery. Another factor affecting the lifespan of a battery is the charge time. Consumers prefer a charge time as short as possible, though fast charging can decrease the lifespan as it stresses the electrodes, affecting their function. External factors such as overcharging or over-discharging also affect the lifespan and should be avoided in any battery. The final relevant criterion in batteries is the cost. This determines whether the battery is suitable for commercial use and is the most significant factor for the end-users of the device [6].

Due to the good energy density and sufficient power output, coupled with the low maintenance and adaptability in voltage, current and size batteries are suitable for many applications, especially in EVs, portable devices and energy storage for the energy transition. This is the reason why the focus of this study will be on this topic. The lithium-ion battery is currently most prevalent in our society, which is why this is considered a baseline in battery development [8]. Figure 2.3 shows that a combination of high specific capacity or high specific power is not possible on the same level as combustion engines. And while the figure implies that fuel cells are more suitable for most storage applications, this type of cell has a very low volumetric density as opposed to batteries, which is why electrochemical battery cells are the storage method of choice in portable devices.

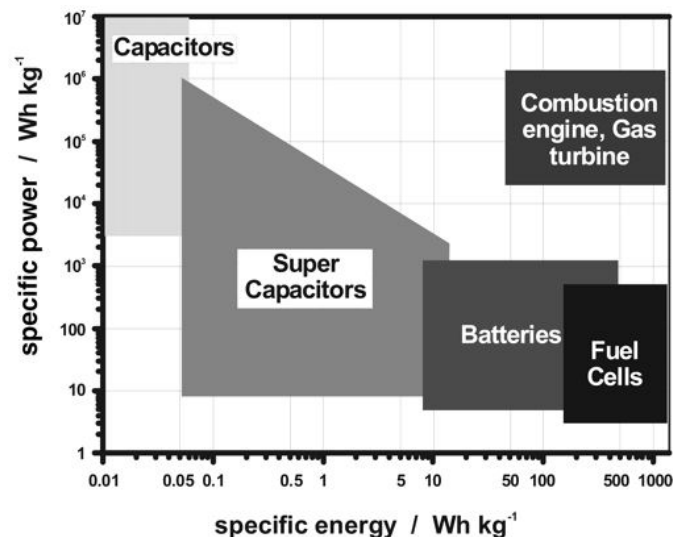


Figure 2.3: Simplified Ragone plot of the energy storage domains for the various electrochemical energy conversion systems compared to an internal combustion engine and conventional capacitors. Reproduced from [6]

2.2. Lithium-ion Battery Limitations

While lithium is seen as the baseline in battery development now, several issues are present for this battery type. One of these is the scarcity of lithium. Currently, the supply of lithium is barely enough to satisfy commercial demands, and it is estimated that the demand will see an increase of 400% by 2050 [9]. While the supply of lithium metal already seems problematic, predictions concerning the cobalt supply indicate deficits as early as 2030. The fact that 60% of the world cobalt production takes place in the Democratic Republic of Congo is also troublesome, as the political climate can negatively affect the cobalt production even further, increasing the scarcity even more. Efforts are made to break free from the cobalt dependence in electrochemical storage devices; examples are the introduction of high-manganese or high-nickel cathodes [10, 11]. Also other materials have gained traction in the battery research field. This includes sulfur-based batteries, but also so-called lithium-air batteries, where the lithium has a redox-reaction with oxygen, and subsequently the involved electrons will be used.

Several alternative battery technologies have been proposed to replace LIBs as a whole as a parallel option, though only some are good enough. The possibilities include magnesium and aluminium due to their high theoretical densities, or sodium and zinc due to their chemistry being similar to lithium and easy to use [12]. Instead of lithium as charge carrier, other elements such as sodium, magnesium and aluminium are also being looked at. Anion-based batteries are also researched using Cl^- , I^- and F^- as carriers. Here different operation mechanisms come into play, such as rocking-chair batteries that use just one atom type as charge carrier similar to the conventional lithium battery.

2.3. Anion-Shuttle Batteries

Modern versions of the anion-based batteries use small ionised halogens as charge carriers, which are very suitable for conversion such as iodide, bromide, chloride and fluoride [13]. Due to having an anion carrying the charge, the anodes and cathodes work differently as well. At the cathode a metal-halogen gets reduced, $\text{MX}_n + n\text{e}^- \rightleftharpoons \text{M} + n\text{X}^-$, and at the anode a metal gets halogenated, $\text{M}' + n\text{X}^- \rightleftharpoons \text{M}'\text{X}_n + n\text{e}^-$. And as the electric movements in these cells go in the opposite direction of the anion, the observed effect is the opposite of LIBs. Employing elemental halogens in a battery cell is difficult due to it being in a highly reactive and gaseous form, but using it bound to a metal and in ionic state, it was rather manageable. As fluorine is the lightest and most electronegative halogen, this was used first in a working cell. This caused a chlorine- and subsequently a bromine-shuttle battery to be realised as displayed in figure 2.4.

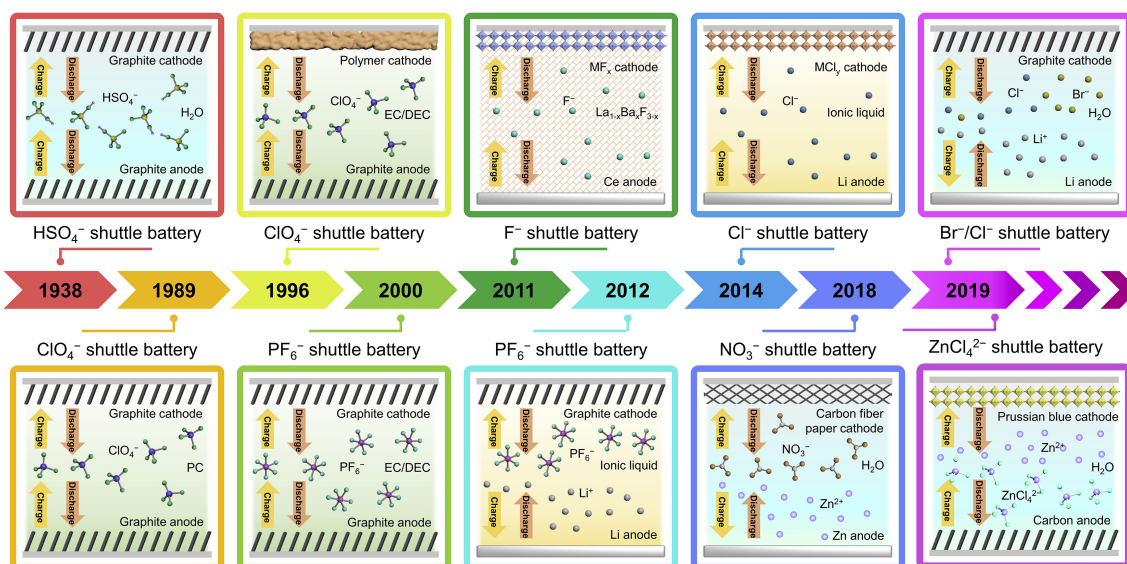


Figure 2.4: Timeline of the development of anion-shuttle-based batteries. PC, EC, and DEC represent propylene carbonate, ethylene carbonate, and diethyl carbonate, respectively. Reproduced from [13]

Fluoride ion batteries (FIBs) gained ground in 2011 when a suitable $\text{LaF}_3\text{-BaF}_2\text{-KF}$ derived solid-state electrolyte, $\text{La}_{0.9}\text{Ba}_{0.1}\text{F}_{2.9}$ became available to form the first FIB cell using BiF_3 that yielded a capacity from 131 mAh/g to 50 mAh/g after 50 cycles [14, 15]. Due to fluoride ions being relatively conductive in several compounds and being able to produce high potentials, these cells immediately attracted more attention. It also opened the door to further research on different halogens as well.

The emergence of the FIB in 2011 prompted the development of a similar chloride ion battery (CIB) in 2014 [16]. The key challenge here was finding ion-conducting materials as well, and while the cubic CsSnCl_3 has an ionic conductivity of 1mS/cm at 100°C, the electrochemical stability is lacking. Therefore using BiCl_3 and a mix of organic electrolytes was used to obtain a usable discharge capacity of 120 mAh/g in the first cycle, and 60 mAh/g in the third. The CIB was improved over time, and 7 years later, an aqueous cell capable of more than 4000 cycles using a zinc anode and graphite paper as the cathode, with a capacity of 200 mAh/g at 2.0V [17]. Adding lithium fluoride increases the cycle life to 10'000. A solid-state cell was manufactured using BiCl_3 as cathode, lead (Pb) as anode, and $\text{Pb}_{0.98}\text{K}_{0.02}\text{Cl}_{1.98}$ as electrolyte [18]. This cell was able to cycle over 30 times at 187 mAh/g, which was

better than previous reported solid-state CIBs, and was hampered mostly by the electrolyte which was not stable enough to function properly.

Later research also enabled the development of the rechargeable bromine ion battery (BIB). In 2020 a proper BIB was realised that could have a capacity from 175 mAh/g to 141 mAh/g after 3000 cycles [19]. Using zinc foil as the anode and carbon black as the cathode, this was one of the first aqueous cells to harness adsorbed bromine with an NH_4Br ethylene glycol electrolyte. This was one of the first demonstrations of using an adsorption mechanism to enhance the operation of halogen-shuttle batteries, preventing elemental bromine from being formed while still using the higher energy of this material.

Of all these examples using anion-shuttle batteries, FIBs seem the most promising, having the most abundant halogen, highest electronegativity and best possible diffusivity. As seen in figure 2.5, this all gives rise to this battery-type to exhibit theoretical volumetric energy densities past the scope of lithium and post-lithium batteries currently under consideration [20]. This is a reason to look deeper in this technology and due to even more relevant breakthroughs in room-temperature electrolyte material for this battery in 2021, research will be even more focused on this promising battery type [21].

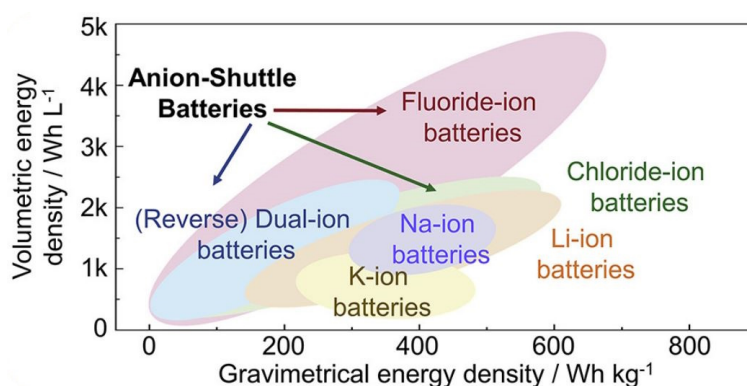


Figure 2.5: Comparison of theoretical volumetric and gravimetric energy density of different battery technologies. Reproduced from [13]

2.4. Fluoride Ion Battery

Fluoride-ion batteries (FIBs), also called fluoride shuttle batteries (FSBs), were just discussed as being a promising post-lithium alternative battery. This is not only due to the current issues and limits of current lithium-based batteries, but also because other alternatives suffer from ionic transport issues (Mg^{2+} Al^{3+}), have a low volumetric capacity (M-Sulfur), are too reactive and dangerous (lithium-metal) or suffer from cycling issues (Metal-air) [22, 23, 24, 25]. Since the fluoride shuttle based battery was reported in 2011, it gained much interest [26]. Not only for the fact it retained the elements that made LIBs so successful, but also because it is not dependent on the same technology to be lucrative. To sketch an image of the properties that make FIBs so attractive as high energy density battery, keep the following in mind [27].

First of all, where lithium is a strongly electropositive element, fluorine is the most electronegative element in the periodic table. This makes that most reactions utilising these elements often yield significant changes in the Gibbs free energy, and redox reactions are accompanied by high potentials. These high voltages contribute to the energy density of the material. Due to the electronegativity, fluorine also has a high oxidative stability, allowing high-temperature operation without unwanted oxidation. This also contributes to the safety of FIBs, as high temperatures are dangerous for most LIBs. There is also no other property that makes fluoride more dangerous compared to others. The small ionic radius contributes to its high ionic conductivity in a wide array of materials. It is also easy to intercalate or insert in host materials without causing significant stress to host materials. This small size also allows multiple fluoride ions to bind with multivalent metals simultaneously, allowing for high energy density per metal atom. Finally there is the abundance, which is fifty times that of lithium. This eliminates concerns about

future supply as well as availability, as the main raw material for fluoride is Fluorspar (CaF_2), and most of the world reserves for this are present in Mexico, China, South Africa, Mongolia, and Spain [20, 28]. Due to all these advantages, FIBs seem to have a high potential and since the first validation of this battery in 2011, many have worked to evaluate different electrode materials and electrolyte materials for this concept.

2.5. Fluoride Ion Battery Electrolytes

To utilise fluoride in a battery cell, a proper electrolyte is needed. This means sufficient conductivity at room temperature, a wide electrochemical stability window and preferably no rare earth metals used. While in the 1980s a solid-state galvanic cell was made using a fluoride-conducting electrolyte, only in 2011 a proper secondary battery cell was realised showing reversibility at 150 °C [26]. This was done using LaBaF_3 [14]. This material had a Tysonite structure, (MF_3 , $M = \text{La, Ce}$), as these are known for their fast fluoride conducting properties of 10^{-6} S/cm at room temperature along with Fluorite (MF_2 , $M = \text{Ca, Sr, Ba}$). However, this conductivity is only found in single crystals, and poly-crystalline structures of this material were only able to achieve a conductivity up to 10^{-8} S/cm. Doping these Tysonite structures with Ca^{2+} , Sr^{2+} and Ba^{2+} enhanced the ionic conductivity substantially. And it was found that $\text{La}_{0.9}\text{Ba}_{0.1}\text{F}_{2.9}$ was capable of a conductivity of $2.8 \cdot 10^{-4}$ S/cm at 160 °C [14]. This decreased to $2.6 \cdot 10^{-6}$ S/cm at room-temperature. This was a big step forward in the development of FIBs, as this opened the possibility to investigate the other components of the battery cell.

Until 2017 improvements were made on the Tysonite structure, which yielded $\text{La}_{0.95}\text{Ba}_{0.05}\text{F}_{2.95}$, sintered at 800 °C for 20 h. This $\text{M}_a\text{M}_b\text{F}_x$ solid solution was capable of a ionic conductivity of $1.26 \cdot 10^{-4}$ S/cm at 60 °C [1]. This was probably due to lesser impurities and better growth of the Tysonite phase. This resulted in better capacity retention of the cells, and a lower voltage hysteresis compared to cells using ball-milled electrolyte mentioned earlier. Then in 2018 for the first time a room temperature solid electrolyte was demonstrated using tetragonal BaSnF_4 [29]. This material was synthesised using ball-milling, and exhibited a conductivity of $3.5 \cdot 10^{-4}$ S/cm at room temperature. This is comparable to the conductivity of the LaBaF_3 electrolyte at 60 °C. It is interesting that these materials, along with PbSnF_4 , were not investigated earlier as their ionic conductivity was known for at least ten years by then [29].

Despite these impressive results, the ESW seems to be insufficient to work properly in a Sn/BiF_3 cell however. Along with these solid-state developments, liquid electrolytes were also researched, due to their intrinsically higher conductivity and these materials are more able to accommodate for the huge volume changes induced in the electrode materials upon reaction. The biggest issue for these liquid electrolytes is the fact that fluoride salts tend to dissolve in non-aqueous solvents and aqueous solvents are not stable enough due to H_2 and O_2 evolution, as well as HF_2^- formation [30]. Fluorohydrogenate ionic liquids have been reported in 2021 with a conductivity of 0.1 S/cm that were able to obtain a capacity from 444 mAh/g to 167 mAh/g for 20 cycles, while another cell in 2021 using aqueous KF was able to demonstrate 218 mAh/g to 90 mAh/g after 1000 cycles [30]. Both of them suffer from capacity loss due to dissolution of the material into the electrolyte or degradation of the electrodes due to the conversion reactions.

However, in 2022 an article was released demonstrating the properties of $\text{CsPb}_{0.9}\text{K}_{0.1}\text{F}_{2.9}$, also called PK10 [21]. This is a compound combining a high electronic conductivity of $1.23 \cdot 10^{-3}$ S/cm at room temperature with an ESW with a width of 1.8V, as depicted in figure 2.6. The conductivity is twice that of previously known electrolytes, and the ESW almost 4 times as large. Despite the fact this material contains cesium, more expensive than gold, the PK10 electrolyte opened the pathway to new development in FIBs, and this will be exploited as much as possible.

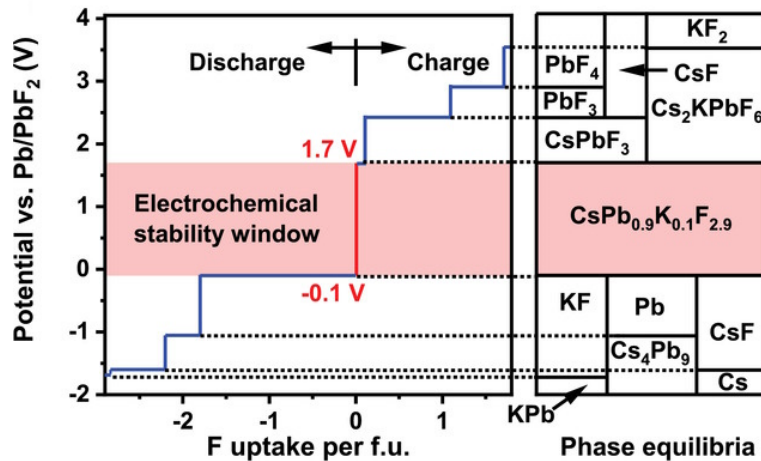


Figure 2.6: Electrochemical stability window of the PK10 electrolyte vs Pb/PbF_2 and the phase equilibria. Reproduced from [21]

2.6. Anode Materials

Possible conversion anode materials for FIBs are generally metal fluorides [20]. This comprises of CeF_3 , MgF_2 , CaF_2 , PbF_2 , ZnF_2 , and MnF_2 . Most of these materials are capable of conducting fluoride ions and are composed of electropositive metals. They are also at least divalent, as this inhibits the solubility of the metal ion in the electrolyte. Properties of these materials are further explained below.

The initial 2011 experiments with FIBs used cerium metal as anode [26]. This is mostly due to the Tysonite structure which facilitates the fluoride conduction due to its vacancy-mediated mechanism. The high melting point of cerium, 795 °C also makes this material a good option for high temperature applications. Further applications have been tried, although most applications of these materials seem to be electrolyte oriented as well as for LaF_3 . It does suffer from a volume expansion of more than 56%, which makes it less ideal [31].

Most new cathodes or electrolytes are currently tested with a lead anode, which has been studied frequently [32, 33]. This is because PbF_2 conducts fluoride ions properly, and it has a low melting point which prevents formation of amorphous crystallite structures that hamper this conductivity [34]. What makes the lead also a good anode material, is its non-polarizing electrode behaviour, as the potential is constant due to the two-phase routine of the reaction. However, this is true for most metal fluorides opposed to intercalation electrodes such as LiCoO_2 and LiC_6 [35]. It also shown that instead of using a pure lead anode, a composite consisting of both Pb and PbF_2 shows better reversibility, higher voltage and higher capacity [36]. This should be taken into account when designing a full electrode as well. In the end, it is disputable whether lead is a proper anode material for commercial FIBs. While the properties are favourable, lead is harmful to the environment. Despite this, lead is used in this project due to its consistent behaviour.

2.7. Intercalation Cathode Materials

Intercalation cathodes have the advantage of having a more stable host structure. This generally leads to higher reversibility, better cycling stability and better transport kinetics, but comes at a lower capacity cost. It has to be noted that the search for proper intercalation cathodes for FIBs has been a struggle, as the intercalation mechanism of anions is inherently different from the more studied intercalation of cations, as in LiCoO_2 . The most relevant progress concerning intercalation cathodes for FIBs has been made in the past 5 years [20]. Starting with lanthanum-based materials with a perovskite structure, after which in later years different options were explored with tunnel-like structures, pyrochlore and MXenes.

Shortly after the release of the LaBaF_3 based FIBs, a setup using $\text{BaFeO}_{2.5}$, a perovskite, was tried [37]. The structure and oxidation of this material was well-understood and therefore chosen to attempt. The

material was experimentally fluorinated using F_2 gas to provide evidence it was possible electrochemically fluorinate this material. While the gaseous reaction was successful, the electrochemical reaction was only yielding a reversible capacity of 5 mAh/g. This indicates that a small part of the intercalated fluoride ions could be extracted. The maximum capacity of this materials was also very low, only 55 mAh/g.

This study was followed by using $LaSrMnO_4$ as intercalation material for FIBs [36]. It showed a step-wise intercalation reaction, like in figure 2.7. First $LaSrMnO_4F$ was formed, and then $LaSrMnO_4F_{2-x}$. It was capable of a reversible capacity of 20 mAh/g, which is still relatively low considering the theoretical capacity is 155 mAh/g, but still better than the $BaFeO_{2.5}$. One of the culprits for unsatisfactory discharge capabilities is the higher discharge overpotential needed for proper defluorination. The carbon additives in the anode are also speculated to be at fault for this. This study also has several other interesting points, due to the manganese in this structure being oxidised. It is demonstrated that more than one fluoride can be intercalated per active transition metal (Mn), a phenomenon rarely observed in lithium-intercalation systems. This possibly opens the path for more efficient intercalation systems. A later study using La_2CoO_4 demonstrated an even higher capacity of 32 mAh/g of the theoretical 133 mAh/g with 25% capacity retention after 50 cycles [38]. The structure of this material is a so-called Ruddlesden-Popper type. This being a form of a perovskites, is known for its low-temperature fluorination chemistry. An even more improved version of this structure replacing cobalt with nickel obtained a cycle life of >200 cycles [39]. This was partially due to setting cut-off charge and discharge capacities, preventing the core-structure from being damaged as much.

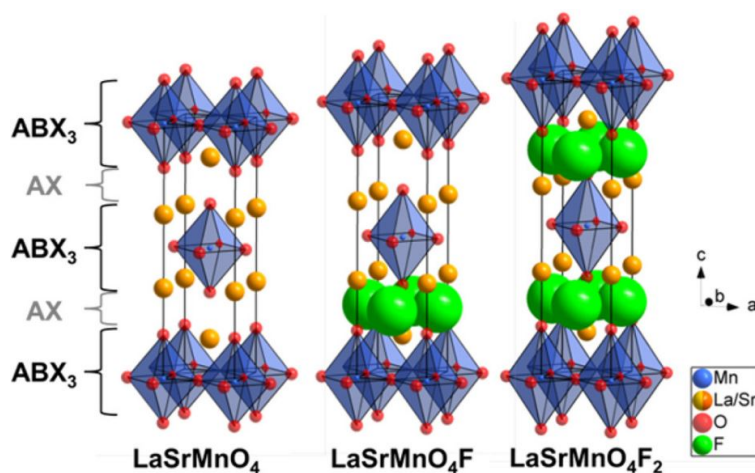


Figure 2.7: K_2NiF_4 type structure of $LaSrMnO_4$ (left) in comparison to partly fluorinated $LaSrMnO_4F$ (middle) and fully fluorinated $LaSrMnO_4F_2$ (right). Reproduced from [32]

The SEI formation plays an equally important role as demonstrated by Wang et al. [40]. This was known for other compounds and electrode materials already, but maybe adding an artificial SEI might be a big solution in obtaining more capacity from the currently tested materials. This interface is directly affected by volume change of the intercalation material itself. This is why last year in 2022 another Ruddlesden-Popper structure was tried. Sr_2MnO_3F . The lower volume expansion of this material, 3% opposed to the 6.2% of the $LaSrMnO_4$, prevents a damaged SEI formation this leads to a better power density overall. Another factor is the fluorination mechanism itself. Where $LaSrMnO_4$ follows a two-phase reaction, the Sr_2MnO_3F is fluorinated forming a solid solution. This reaction expands more smoothly due to homogenisation of the surface as seen in figure 2.8. Due to the favourable properties, this type of intercalation reaction is favoured over the two-phase reaction observed in other intercalation materials as well.

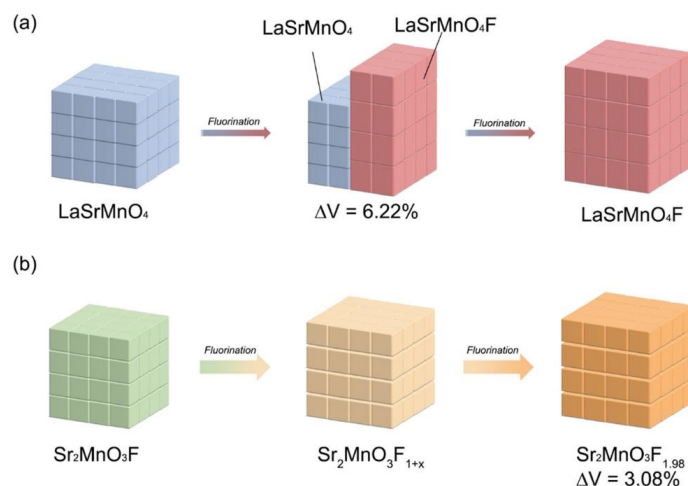


Figure 2.8: Schematic illustration of the volume changes and phase transition models during the charging process for (a) $\text{LaSrMnO}_4\text{F}$ and (b) $\text{Sr}_2\text{MnO}_3\text{F}_2$. Reproduced from [40]

Finally it has to be noted that not every perovskite is suitable as cathode material. Not due to a low potential that would make it more suitable as anode material, but due to a total structural transformation that occurs as the fluoride ions are not able to intercalate in the expected sites in the structure. One example is ReO_3 , where the fluoride anions do not intercalate solely in the A-site as seen in figure 2.9, but also in the X-site, causing it to form tet- FReO_3 [41]. This was observed using X-ray absorption spectroscopy and neutron scattering. This type of intercalation is not reversible, and these types of structural transformation should be taken into account when considering a new intercalation anode for FIBs by using DFT calculations beforehand to avoid these materials.

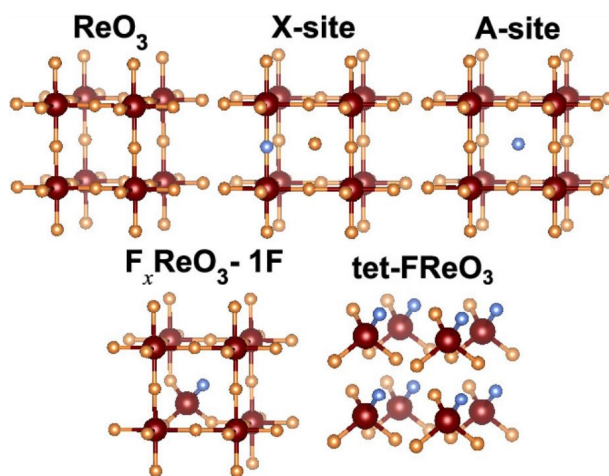


Figure 2.9: Various models for the fluorination of ReO_3 that are considered throughout the text with Re shown in red, oxygen in orange, and fluorine in blue. Reproduced from [41]

To further increase the current knowledge about potential intercalation materials, other research has been carried out [42]. Using tunnel-like structures, Zaheer et al. demonstrated reversibility of a FeSb_2O_4 structure. Almost total fluorination with the help of XeF_2 could be achieved, oxidizing most iron atoms from +2 to +3. Using X-ray spectroscopy and XANES, it could be observed that this process proceeded homogeneously through the whole material. Defluorination using n-butyllithium was able to fully defluorinate the structure afterwards. This shows that theoretically this structure should be able to function as anode material. Another benefit of this research allows assessing the potential of a material to be a suitable electrode for FIBs without building a full cell. This lets the experimental procedures not depend on a proper counter-electrode, providing higher clarity whether the functioning of the material is just dependent on itself.

Other relevant developments include exploration of defect structures such as defect pyrochlore CsMnFeF_6 [43]. As pyrochlores are known for high ionic conductivity but ordered anionic vacancies. This should facilitate fluoride intercalation. The material was synthesized in three different manners: Hydrothermally, ceramically and mechanochemically. It was observed that hydrothermal material cycled very poorly, the ceramic material cycled poorly and only the mechanochemical material yielded near theoretical capacity. This is interesting as these particles did have the biggest deviation in size. Understanding how the fabrication method affects the morphology and thereby the performance of the materials is modified. Also interesting in this study was the structure change from pyrochlorite to a more orthorhombic arrangement. This did not significantly affect the properties however, and XAS indicated that the iron and manganese still were able to be active during cycling. It is unclear however how this structure transformation did not change the conductivity, despite lattice sites changing along with the discharge profile.

Finally MXenes are explored, two-dimensional materials that consist of thin layers of transition-metal carbides, nitrides and carbo-nitrides [44]. The structural formula of these materials is M_{n+1}X_n where X indicates carbon or nitrogen. These materials are known for their impressive mechanical flexibility, significant strength and high conductivity. They have proven themselves to be promising electrode materials for LIBs, but this was not investigated for FIBs until 2022. Then Yang et al. used computational methods to assess the viability of this material. Looking at the maximum adsorption concentrations for the fluoride ions on the surface of the tested material, Ti_2CH_2 and V_2CH_2 , it was found that the respective capacities were 488 mAh/g and 462 mAh/g. These were comparable to the capacity of adsorbing lithium ion on similar carbides. Of these materials, the diffusion barrier was also evaluated and was found to be 0.31 eV for both materials, which is better than that of LiCoO_2 , with 0.4 eV. Both DFT and ab initio molecular dynamics (AIMD) demonstrated that not only the fluorinated counterparts of the tested materials would be stable up to 500K, but also that the mechanical strength seems sufficient at accommodating volume change stresses in the material. And while this material has not been physically tested yet, just as the intercalation anode materials, it seems to have promising properties to be used as cathode material for FIBs, but much research has to be done to do a better prediction of the future of this material in FIB electrodes.

From these recent developments in the field of intercalation cathodes for FIBs it can be concluded that current research is mostly focused on exploring different types of materials first, and trying to understand the underlying mechanisms instead of trying to improve the existing materials. This is mostly due to the relatively low cycle lives and CE that is observed in the tested materials, but also due to the fact that the capacities of the tested materials are not very high. This trend is likely to be observed for the coming few years until a suitable material is found that can have potential as FIB intercalation cathode. The increasing attention that FIBs get over time should also be considered, as this will accelerate the research intensity in this topic, leading to a higher likelihood of finding better materials in short term.

2.8. Conversion Cathode Materials

As cathode material for FIBs both metal fluorides and metal oxyfluorides have been researched and tested. This is slightly different from LIBs where the focus lies mostly at the metal oxides and only recently on metal oxyfluorides as well. Just like the other electrode materials, conversion cathode materials for fluoride ion batteries have gained increasing popularity over the last years. As BiF_3 , CuF_2 and FeF_3 have been tested in lithium ion batteries, they have also been tried in FIBs due to their promising results in the other battery type. Naturally earlier experiments used a material that was known for its reversibility and XRD detectability, therefore the cell made in 2011 by Reddy and Fichtner was made using bismuth fluoride (though CuF_2 was also tested) [15]. With a theoretical capacity of 302 mAh/g, 38 cycles were achieved where the capacity faded gradually from 190 mAh/g to 50 mAh/g. It was interesting to note that a BiF_3 solid solution performed better with an initial discharge capacity of 190 mAh/g, while a composite BiF_3 only yielded 126 mAh/g. A higher fluoride conductivity in the solid solution might be an explanation. Later research on this material pointed out that not only the redox couple BiF_3/Bi is active, but that through the retained oxygen in the bismuth particles also oxyfluorides were formed upon fluorination in a gradient seen in figure 2.10 [45]. As this oxyfluoride is conductive to fluoride ions, this does not seem to affect the cyclability of this material significantly. It might even contribute to the reversibility by allowing a higher degree of fluorination according to quantitative PDF

analysis and computational methods. Even more, this research opened the path to look at oxyfluorides as electrode materials for FIBs.

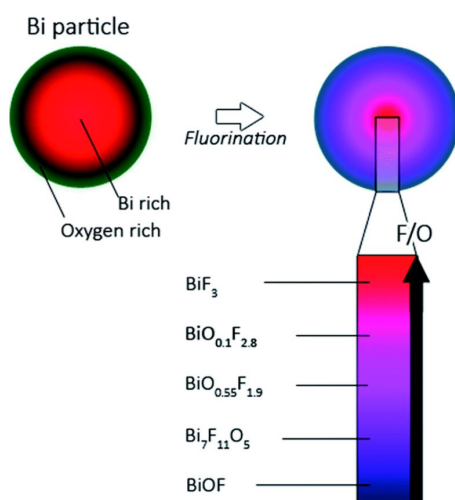


Figure 2.10: Schematic of the proposed mechanism for the fluorination of the starting Bi powder presenting an oxidized surface. Reproduced from [45]

BiF_3 seems to have several issues however, it seems to react with certain types of electrolyte, and the volume expansion of 134% upon fluorination is not favourable at all, calling for methods to mitigate effects of this [46]. This material was tried in DIBs as well, where it yielded varying results, and the formation of oxyfluorides was observed there as well with XRD [47, 48]. The performance of this electrode was enhanced in 2019 by using carbon additives. This not only facilitated conductivity, but the preparation method caused smaller particles, that significantly enhanced the cycling capabilities of the material as well. This would then be used in subsequent electrode materials as well, as it doubled the capacity and smoothed the voltage plateau as seen in figure 2.11 [49]. And as follow-up on that research an electrode using a highly-binding binder was used, this improved the material properties even further, enhancing the cycle performance [50]. It has to be noted that all these methods tried to improve the currently existing BiF_3 , which makes sense from a perspective where one would try to understand the behaviour of metal fluorides. But while BiF_3 is easily detectable using X-ray techniques, the high mass and low theoretical capacity are not practical in commercial applications.

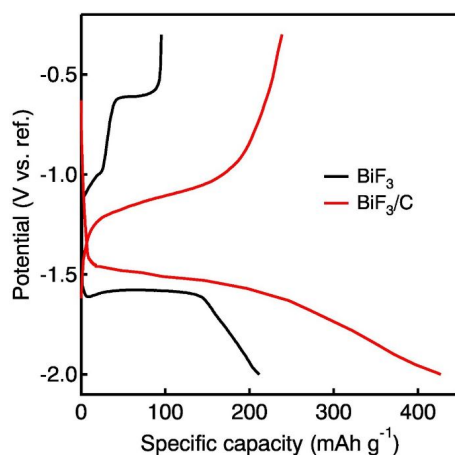


Figure 2.11: Discharge and charge curves of BiF_3 and BiF_3/C over the potential range between -2.0 and -0.3 V (vs. ref.) in the first cycle. Reproduced from [49]

As demonstrated by Grenier et al. in 2017, oxyfluorides formed during cycling of the bismuth fluoride cathode do not hamper the functioning of the cell [45]. On the contrary, it seems that the multiple oxyfluoride phases present the material actually seem to facilitate the processes in the cell, as the

oxyfluorides exhibit a greater fluoride ion conduction than the metal fluorides. It has to be noted that the oxygen atoms do not diffuse, which is a very important aspect, as that means that this material can actually be used as an electrode material itself. A ternary fluoride $\text{Bi}_{0.7}\text{Fe}_{1.3}\text{O}_{1.5}\text{F}_{1.7}$ was synthesized

and used as cathode material for FIBs, which is depicted in figure 2.12 [51]. This has a theoretical capacity of 166 mAh/g, although a charge and discharge capacity of respectively 225 mAh/g and 360 mAh/g were observed, which are probably caused by (de)fluorination of acetylene black. No further cycles could be measured. Also other bismuth oxyfluorides have been investigated. And one of these is $\text{Bi}_7\text{O}_5\text{F}_{11}$ [4]. This has the benefit of being 5 times more electronically conductive as the normal bismuth fluoride as was demonstrated earlier, $1.6 \cdot 10^{-4}$ S/cm. This material has a theoretical capacity of 168 mAh/g and could be cycled up to 50 times where the capacity decreased to 113 mAh/g from 178 mAh/g. This was almost three times as much retention as a similar cell with BiF_3 as cathode material. This is comparable with results that were obtained with the PK10 electrolyte and Ag/Pb/PbF₂ electrodes [21]. This would be considered an indication for oxyfluorides being a promising class of materials for electrode materials, the decent cycling stability.

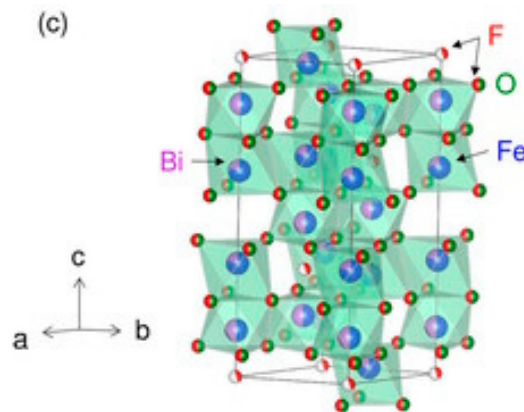


Figure 2.12: Crystal structure of BFOF. Bi, Fe, F, and O atoms are represented as purple, blue, red, and green spheres, respectively. Reproduced from [51]

As mentioned before, bismuth is a relatively heavy metal, and a higher atomic weight is tied with a lower gravimetric capacity. That is why another option has been explored: Cu_2OF_2 [5]. This material has a theoretical capacity of 296 mAh/g, and the cubic lattice has a high copper content, which is active redox material. It was demonstrated that the first discharge capacity was 174 mAh/g which faded to 103 mAh/g after 35 cycles. It is unclear how this material evolves during the conversion. It is known that the fluoride ions probably first take up the space in the tetrahedral site of the Cu-fcc sub-lattice, demonstrated in figure 2.13a. But four structures can form, seem probable according to calculations, figure 2.13b. The issue is that none of these are thermodynamically stable, which would imply that Cu_2OF_2 would convert back to CuF_2 and CuO when it is formed. The XAS spectra taken at the experiment do not eliminate the possibility of such a phase forming, and upon further cycling the material might fully lose its oxygen, converting to sole CuF_2 . This is something that should be studied in further experiments.

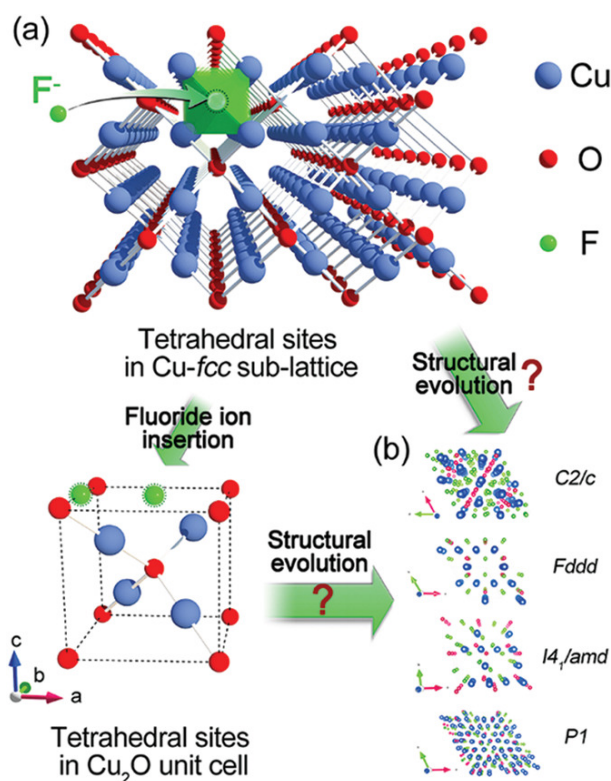


Figure 2.13: (a) Probable tetrahedral sites and (b) configurations for F intercalation. Reproduced from [5]

Where in LIBs the possibilities of BiF_3 , CuF_2 and $\text{FeF}_2/\text{FeF}_3$ were tried, a similar line of materials was observed in recent FIB developments. The same for oxyfluorides, where BiOF and Cu_2OF_2 have been explored. However, in LIBs iron oxyfluorides have been explored already, and have shown good cyclability, stability and they seem like promising materials. This material has not been tested on fluoride ion batteries yet, despite the promising properties such as high abundance, low cost and higher potentials compared to the earlier tested Cu_2OF_2 . One iron oxyfluoride material that has been tested, is $\text{Sr}_3\text{Fe}_2\text{O}_5\text{F}_2$. This material uses the redox-reactions of iron from $\text{Fe}^{2+}/\text{Fe}^{3+}$, which is the same as would be used with FeOF . There are a few differences however, as FeOF is a conversion electrode with a theoretical capacity of 295 mAh/g, $\text{Sr}_3\text{Fe}_2\text{O}_5\text{F}_2$ is an intercalation electrode with a theoretical capacity of 118 mAh/g, significantly lower. Although it was capable of retaining a capacity of 116.7 mAh/g for 70 cycles, the capacity is too low for commercial applications [3]. Therefore, due to the higher capacity caused by a lower amount of structural atoms, FeOF is a more promising material.

2.9. Objective

The main goal of this research is to evaluate the eligibility of FeO as cathode material for fluoride ion batteries. To do so, the material must be able to be fluorinated and defluorinated for a significant part of their theoretical capacity. To investigate whether this is feasible, the following research questions are posed:

- To what degree can FeO be electrochemically fluorinated in a solid-state battery cell environment?
- Find an adequate and feasible route for the synthesis of FeOF
- What is the influence of the Pb/PbF_2 anode and PK10 solid-state electrolyte that are used in conjunction with the iron oxides or iron fluorides?
- What is the effect of any side-phases present in the materials?
- To what degree can FeOF be electrochemically defluorinated in a solid-state battery cell environment?

Methodology

3.1. Pb/PbF₂ Composite

The cathode material will vary, and therefore a constant anode material is used throughout the project. This concerns a lead-lead(II)fluoride composite as this has been reported several times already, and seems to provide a consistent performance. The precursor materials consisted of PbF₂ (Merck, 99% purity) which was combined with elemental lead powder (Alfa Aesar, 99.9% purity) and ground in a mortar for 10 minutes with carbon nanotubes (Merck, 98% purity) and the PK10 electrolyte in a weight ratio of 15:15:10:60 for Pb:PbF₂:carbon:PK10. This active material composite was fabricated up to five times with consistent quality. Having a capacity of 0.03 mAh/mg. The PK10 electrolyte is added in the composite to ensure proper ionic conductivity of the electrode, as the active material itself has a low ionic conductivity. The carbon nanotubes are added to ensure sufficient electronic conductivity to perform the electrochemical defluorination of the lead fluoride component. Due to the presence of lead metal, this same composite is also used for the defluorination of the synthesised FeOF material.

To ensure no changes occurred during production of this active composite material, and the precursors were pure, the structure of the active material and precursors was characterised using XRD. No monochromator was needed for these measurements due to the absence of iron.

3.2. Ball Milling

To synthesise a material, different techniques can be used. However, most of these conventional methods are limited by the products they can yield; often only thermodynamically stable compounds can be fabricated. Several meta-stable ceramic materials exist with desired properties such as nanocrystallinity or non-equilibrium local structures. This is commonly necessary in solid-state electrolytes and specifically fluoride-ion conducting materials [52]. To access these special materials, mechanochemical synthesis is one of the methods that can be used, specifically ball milling. This is used in this project for solid-state electrolyte synthesis, mainly PK10: CsPb_{1-x}K_xF_{3-x}.

The operation of a planetary ball mill, a common type of high-energy ball mills, involves the counter-rotation of the supporting disk and the ball mill jars, placed on independently rotating disks as seen in figure 3.1. The milling tools, jars and balls, are made of materials that resist degradation and contamination such as hardened steel, zirconium dioxide, or tungsten carbide balls. The machine needs to be capable of speeds up to at least 500 rpm for the synthesis. There are two types of ball milling available; wet and dry milling [52]. The latter is commonly used in the synthesis of solid-electrolytes.

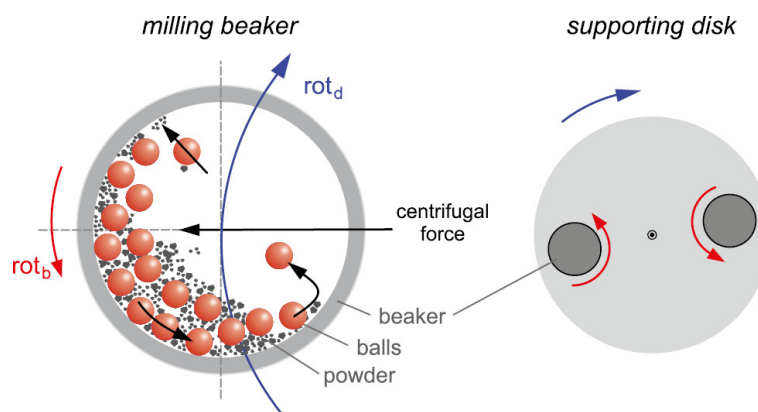


Figure 3.1: Illustration of the milling tools and the principle of operation of a planetary mill. The colored arrows indicate the counter-rotation of the supporting disk (rot_d) and the milling beakers (rot_b). Reproduced from [52]

The process of ball milling itself involves the mechanical treatment of several starting materials in high-energy ball mills [53]. The centrifugal forces produced by the rotating beakers and counter-rotating supporting disk accelerate the milling balls, causing them to move across the beaker and impact the opposite side. This high-impact force grinds and erodes the starting material through shear and friction forces. The individual particles of the starting material undergo continuous size reduction, resulting in increased surface area and the formation of defects, as the irregular and fast movement of the milling balls generates spots of high pressure and temperature for a very short duration. While the milling is carried out at room temperature and ambient pressure, these localised hot-spots resemble high synthesis temperatures or pressures. Therefore, thermodynamically unfavourable structures can be formed, and the corresponding properties of high-temperature or high-pressure phases can be preserved in the synthesised product.

The selection of milling conditions, including milling time, rotation speed, milling jar material, and the number and material of the balls, all affect the outcome of the final product [53]. Longer milling times can close miscibility gaps and yield solid solutions that are otherwise challenging to prepare. In crystalline materials it also reduces grain size. However, after a certain milling time, the particles get so small, they start clustering, which leads to unfavourable effects in some materials. The ability to access non-equilibrium phases and unique local structures is particularly beneficial for materials with enhanced properties and functionalities. The rotation speed should be sufficient to allow the balls to impact with enough energy to induce synthesis of the desired material. Too high rotation speeds also start eroding the milling tools, and should be avoided to prevent contamination of the final product.

3.3. Electrolyte Synthesis

Currently, several solid-state electrolytes are available for FIBs. While $PbSnF_4$ is capable of reaching a conductivity of $1.6 \cdot 10^{-3}$ S/cm at room temperature, the electrochemical stability window (ESW) is very small. Therefore the electrolyte used in this project is $CsPb_{1-x}K_xF_{3-x}$ with $x = 10$, also known as PK10 [2]. This is a compound combining a high electronic conductivity of $1.23 \cdot 10^{-3}$ S/cm at room temperature with an ESW with a width of 1.8V. The conductivity is twice that of previously known electrolytes, and the ESW almost 4 times as large. Despite the fact this material contains cesium, more expensive than gold, the PK10 electrolyte is an outstanding solid-state electrolyte.

A total of five batches of this material were prepared through ball milling of this material. The starting materials were CsF (VWR, 99.5% purity), KF (VWR, 99%) and PbF_2 (Merck, 99% purity). These precursors were dried and stored in a MBRAUN UNIlab glovebox filled with 1 atm (Linde) argon. A mixture of 1488 mg CsF, 2162 mg PbF_2 and 56 mg KF was put in yttrium-stabilised ZrO_2 ball mill jars (45 ml) at a ball to powder ratio of 1:20 using 10mm balls of the same material under the argon atmosphere. The milling was conducted using a planetary mill (FRITSCH, Pulverisette 7 premium line). First the material was milled at 100 rpm for 10 minutes, mixing the material. After this, the material was ball milled at 500 rpm alternating 10 minutes milling with 10 minutes rest, completing 48 cycles. This

results in a total milling time of eight hours. The electrolyte was extracted and stored in the glovebox under an argon atmosphere.

To assess both the electrochemical impedance and the electrochemical performance, an experimental custom solid-state cell is used. It consists of two stainless steel disks with holes for impedance measurements. The centre of these disks contains a socket for a stainless steel current collector cylinder. A non-conducting, tubular sleeve with an inner diameter of 10 mm encases the current collectors, and this whole system is bolted together with three non-conducting bolts. The material to be tested is located within the sleeves, between the current collectors. The assembly of this system is dependent on whether a full cell, or just electrolyte is tested. The procedure for electrolyte testing is schematically depicted in figure 3.2.

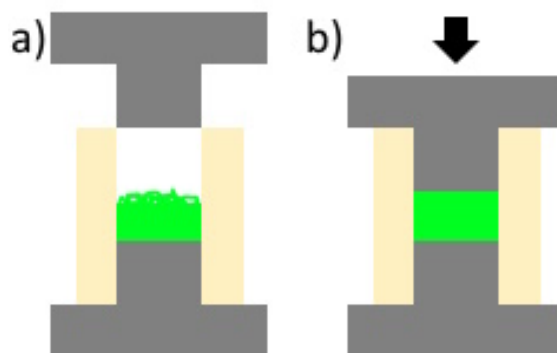


Figure 3.2: Schematic representation of solid-state cell. a) Putting powdered PK10 solid-state electrolyte in cell b) press cell at 50 bar for 5 minutes

The ionic conductivity of the electrolyte material was assessed using EIS. To do so, still under an argon atmosphere, 200 mg of the material is pressed into a pellet into the experimental solid-state cell using a Syrio Dental P400 hydraulic press. First the pressure was ramped up to 50 bars over the course of 2 minutes. After that, the pressure was kept at 50 bar for 5 minutes after which the bolts were tightened. As the cell is airtight, it could be removed from the glovebox and an EIS measurement could be conducted. For this, an Autolab PGSTAT302N potentiostat was used and the electrolyte resistance, R_{∞} was determined as well as the combined electrolyte plus electrode resistance, $R_p + R_{\infty}$. This is explained in section 3.8. The structure of this material and its precursors was subsequently characterised using XRD.

After this, the pellet thickness is measured using a Mitutoyo Digital Thickness Gauge ID-C112B. Using the pellet's thickness, its impedance and diameter, the electronic conductivity of the material can be calculated using the formula of $\sigma = l/R_p \cdot A$. With σ being the conductivity of the electrolyte in mS/cm, l the thickness of the pellet, R_p the electrochemical impedance of the electrolyte and A the surface of the sample in cm^2 . A is in this project always 0.785 cm^2 as the surface of the current collectors has a fixed diameter of 1 cm.

Using this procedure, the electrolyte composition and ionic conductivity will be obtained. This is needed to determine whether the synthesised material is suitable to be used as electrolyte in a full cell. This is also to compare the impedance, and therefore ionic conductivity, of a full cell with the virgin electrolyte.

To obtain information regarding the electrochemical stability window (ESW), a composite was constructed in a similar manner as the Pb/PbF₂ composite, except that the active material is the PK10 itself. Therefore, PK10 was ground in a mortar for 10 minutes with carbon nanotubes (Merck, 98% purity) with a ratio of PK10:carbon of 90:10. All of this was prepared in a MBRAUN UNIlab glovebox filled with 1 atm (Linde) argon. This composite will be referenced in this work as the electrolyte carbon composite (ECC).

3.4. FeO Composite

The investigated active materials are ferrous oxide, FeO, and iron oxyfluoride, FeOF. A composite containing was also tested to assess its charging potentials along with evaluating the stability of the electrolyte and the use of different preparation methods to form the composite material needed for cell construction. The FeO will be investigated to assess its possibility to be fluorinated, while the FeOF will be attempted to be electrochemically defluorinated in this study. Both materials are incorporated in composites with solid-state PK10 electrolyte materials and carbon nanotubes to enhance the ionic and electronic conduction of the electrode.

The FeO composite is fabricated in a similar manner as the Pb/PbF₂ composites. For FeO three batches were synthesised. The first batch used FeO from Merck, 99.9% purity, the two later batches used FeO from Thermo Fisher, 99.5% purity. Characterisation pointed out that Thermo Fisher supplies FeO in higher purity. The other precursor materials consisted of carbon nanotubes (Merck, 98% purity), and a PK10 electrolyte. The materials were added to, and ground in a mortar for 10 minutes in a weight ratio of 30:10:60 for FeO:carbon:PK10. This was done under argon to protect the PK10 electrolyte and prevent reactions with moisture and oxygen in the air. To enhance the ionic contact between the iron particles, one other composite was synthesised using ball-milled (6 hours, 250 RPM) FeO. This same protocol, except ball-milling was followed for the iron oxyfluoride, and the FeO is replaced with the synthesised FeOF. One batch was made of the FeOF composite.

To calculate the capacity and open circuit voltage (OCV) of the synthesised composites, two calculations were used. To calculate the specific capacity in mAh/g of the material, the following equation is used:

$$\text{Specific capacity} = \frac{n \cdot F}{3.6 \cdot M}$$

Where n is the amount of electrons, and therefore F^- ions transferred, F is the Faraday constant in sA/mol, 96485, and M is the molar mass of the material in (g/mol). These values are displayed in table 3.1. To obtain the capacity of the composite, this value is multiplied by the fraction of active material in the composite. 0.3 for the FeO(F)-based composites, and 0.15 for the lead-based composite.

To obtain the OCV of these materials, Gschwind et al. used thermodynamic calculations using the heat of formation of the involved metal fluorides [31]. This is because the voltage corresponds to a difference in the chemical potential of fluorine in the different metal fluorides: MF_x and $M'F_y$. This is described using the following equation:

$$\text{OCV}(MF_x, M'F_y) = \frac{\frac{1}{x}\Delta H_f(MF_x) - \frac{1}{y}\Delta H_f(M'F_y)}{e}$$

Where the heat of formation for the respective fluorides is used, and e is the elementary charge of an electron. The results of calculations for the different used materials is depicted in table 3.1. The heat of formation is derived from the Materials Project [54]. Iron fluorides have also been included as there is residual α -iron present in the FeO precursors. This might lead to a different OCV than expected.

Electrochemical reaction	OCV (V vs Pb/PbF ₂)	Specific capacity (mAh/g)	Supplier (Purity)
FeO \longrightarrow FeOF	-0.273	373.0	Merck (99.9%) Thermo Fisher (99.5%)
FeOF \longrightarrow FeO	0.273	295.0	Synthesised
Pb \longrightarrow PbF ₂	0	258.7	Alfa/Aesar (99.9%)
PbF ₂ \longrightarrow Pb	0	218.6	Merck (99%)
Fe \longrightarrow FeF ₂	0.043	959.8	Merck (99.5%)
Fe \longrightarrow FeF ₃	-0.177	1439.7	Merck (99.5%)
PK10 \longrightarrow CsPb _{0.9} K _{0.1}	-	205.4	Synthesised

Table 3.1: Overview of the properties of conversion cathode materials. Values are calculated using the formulas mentioned above and data from the Materials Project [54]

An overview of all synthesised composites is tabulated in table 3.2. The capacity is depicted in mAh/mg to make the calculated amounts put into the cells more clear. The lead/lead(II) fluoride composited is listed twice, as it can both be fluorinated and defluorinated.

Composite Name	Active Material	Capacity (mAh/mg)	Batches Created
ECC	PK10	184.86	1
Pb/PbF ₂	Pb	38.31	5
	PbF ₂	32.71	
FeO 1	FeO	111.90	1
FeO 2	FeO	111.90	1
FeO BM	FeO	111.90	1
FeOF	FeOF	487.7	1

Table 3.2: Overview of all prepared composites

3.5. Scanning Electron Microscopy

To obtain information about particle size of the active material used in the battery cells, or the morphology of the composites, a scanning electron microscope (SEM) can be used [55]. This device utilises electromagnetic lenses to focus an electron beam on the surface of a sample as seen in figure 3.3. This surface is subsequently scanned to detect the low-energy (<50 eV) secondary electrons that are emitted from the k-shell of the specimen atoms at the surface. They are collected by a grid, and detected by a scintillator where the signal is converted and amplified to obtain an image of the surface. The observed contrast is caused by the variations in signal intensity, which is not only dependent on the topography of the surface, but also on the phase composition of the observed material. This allows distinguishing between different phases by contrast in some compositions.

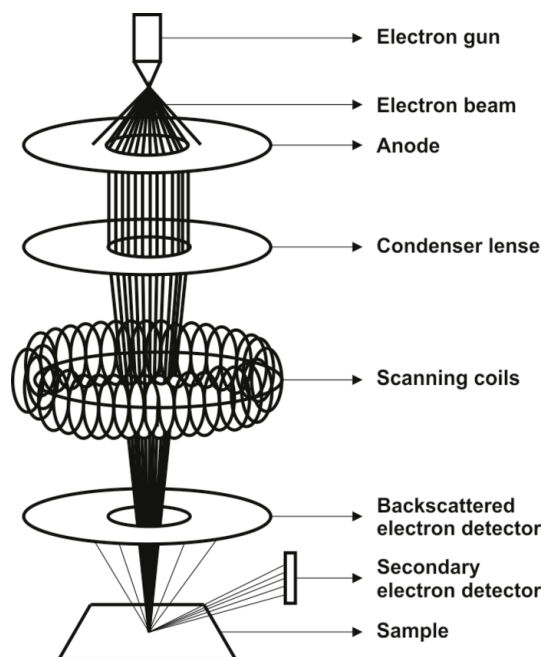


Figure 3.3: Schematic representation of a SEM setup. Reproduced from [56]

In conjunction with the SEM, energy-dispersive X-ray spectroscopy (EDS) is often used [57]. This enables elemental analysis of the sample by detecting the characteristic X-rays emitted by the sample when it is hit by the high-energy electron beam. Using these characteristic X-rays, the elemental composition can be determined for a point, line or area of the sample. Elemental mapping, to obtain an overview which part of the samples contain specific elements, is also possible. This will be used to verify the composition of the particles of the active materials and composites, as this composition can affect the electrochemical behaviour.

To validate the structure of the composite, SEM was used in combination with EDS. A SEM and EDS image was taken of the rough FeO, the FeO composite, ball-milled FeO and a pressed, used PK10 pellet. To do so, a scanning electron microscope, SEM (JEOL JSM 6500 F) equipped with an energy-dispersive X-ray spectroscopy (EDS) system (JEOL IT100LA) was used for this. The sample in powder form was applied on a polydimethylsiloxane (PDMS) composite specimen platform and adhered using specialised conductive tape. The electron acceleration voltage for SEM analysis was 15 kV, for EDS this was 20 kV. Measurements were taken at a magnification of both 750x and 4500x. The EDS was used to identify the separate particle grains observed in the SEM images. Operation of the machine was according existing protocols.

3.6. Iron Oxyfluoride Synthesis

Ferrous oxide, FeO, can be acquired from chemical suppliers, but this is not true for FeOF. This material can be synthesised according to two methods, either a solvothermal method, or a modified one.

Method 1 [58]: A modified solvothermal method that involves methanol (Merck, 99.8% purity) and 1-pentanol (Merck, 99% purity) as co-solvent. 66.8 mg of $\text{FeF}_3 \cdot 3\text{H}_2\text{O}$ (Merck, 32.3-34.6% Fe) was added to 2 mL of methanol and stirred until a transparent solution was obtained. This was added to a 45 mL Teflon-lined stainless steel autoclave, 4744 General Purpose Vessel. 24 mL of 1-pentanol was added and the vessel was heated for six hours at 200 °C. After cooling down to room temperature, the resulting ochre powder was collected and washed with pure ethanol and dried under vacuum for twelve hours at 80 °C. This method did not seem to obtain the proper results which is why a second method was attempted.

Method 2 [59]: This involved 66.8 mg $\text{FeF}_3 \cdot 3\text{H}_2\text{O}$ being added with 27 mL of 1-propanol (Merck, 99.5% purity) in a 45 mL Teflon-lined stainless steel autoclave, 4744 General Purpose Vessel. The mixture was stirred for five minutes until most powder dissolved, and heated to 200 °C for twenty-four hours. After being cooled down to room temperature the product was washed several times with pure ethanol and dried overnight at 50 °C under vacuum.

From both methods, the resulting powder was recovered, dried and stored in a MBRAUN UNIlab glove-box filled with 1 atm (Linde) argon. Subsequent XRD analysis and Rietveld refinement are conducted to assess the purity of the synthesised material.

3.7. Cell Fabrication

To determine the properties of the materials, and subsequently galvanostatically charge or discharge this, a full solid-state electrochemical cell must be fabricated. The empty cell consists of several parts including a PEEK cylindrical sleeve, two stainless steel current collectors and three non-conducting metal bolts. The current collectors have custom-fitted slots to attach wires needed for attachment to the galvanostat and to the EIS device. This is all seen in figure 3.4.

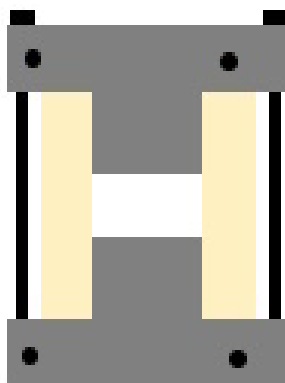


Figure 3.4: Schematic representation of solid-state cell containing all relevant components

Preparing the full cell is depicted in figure 3.5. 200 mg of the PK10 electrolyte is put into the cell (a), spread out, and pressed at 50 bar for 5 minutes (b). After this, the respective anode and cathode composites are placed above and below a layer of PK10 electrolyte (c-e) and the cells were put at 50 bars for 10 minutes to ensure sufficient contact throughout the whole electrochemical system (f). The pressure was increased incrementally over 2 minutes to prevent damage to the internal parts of the cell.

Despite careful preparation, errors can occur during fabrication. The most important error is breaching of pressed electrolyte pellet, figure 3.5g-h. In this case the cell short-circuits and is not suitable for testing. This can occur during the closing of the full cell, but also upon applying pressure. In this case, uneven distribution of the electrode composite powders will cause stresses that break the pellet, figure 3.5g. A misaligned current collector can also cause this, figure 3.5h, which can also cause the pellet to break, short-circuiting the cell. Because of this, the EIS behaviour of the individual cells is evaluated to ensure no short-circuiting occurred between the cathode and anode composite of the cell due to cracking or breaching of the solid electrolyte layer. As the cells are prone to short-circuiting, these results are not relevant, and these results are not evaluated further.

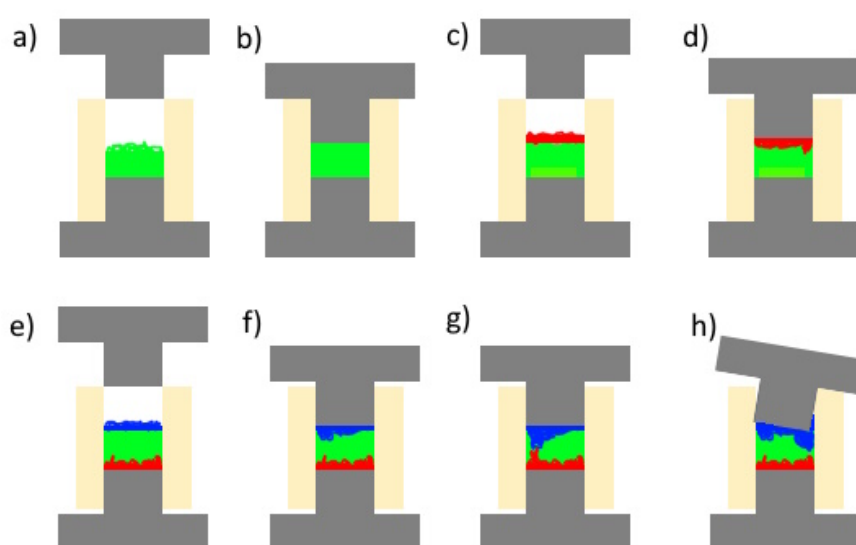


Figure 3.5: Schematic representation of solid-state cell. a)-f) Steps of cell fabrication. g) Short-circuit induced by uneven electrode composite distribution. h) Short-circuit induced by misaligned charge collectors.

Several types of cells were constructed to evaluate the electrochemical performance of the separate materials, they are displayed in table 3.3. The symmetric Pb/PbF₂ cells were fabricated to evaluate whether lead/lead(II) fluoride is a suitable counter-electrode material to test the performance of other materials against. The ECC cells were made to evaluate the ESW of the cells, to determine whether the solid-state electrolyte is stable in the voltage region that the FeO is supposed to react according to the thermodynamic calculations in section 3.4. Then two types using the different FeO composites, wherein FeO of two separate suppliers is evaluated. Finally a cell that contains a composite of the synthesised FeOF.

Cell Name	Significant Note	Cells Created	Cells Succeeded
Pb/PbF ₂ cell	Symmetric Cell	6	4
ECC cell	90% PK10 10% carbon	2	2
FeO 1	Merck	2	0
FeO 2	Thermo Fischer	2	1
FeOF	Synthesised	2	1

Table 3.3: Overview and description of all prepared cell types

3.8. Electrochemical Impedance Spectroscopy

Electrochemical impedance spectroscopy (EIS) can be used to probe the physical and chemical state of solid state battery components or the full cell. The information obtained from the measurement include the ionic conductivity of a material, as well as the ionic transport mechanisms present. This can be quantified by differentiating between the different contributions to this conductivity by these mechanisms.

The EIS functions by applying a small perturbation voltage $E(t)$ to a an electrochemical system, like the the solid-state cells used in this project, and the resulting linear current density $j(t)$ is measured [60]. This will have the same frequency as the voltage, but its phase and amplitude may differ. The frequencies used in this project vary between 10 and 10^7 Hz. The ratio between these values is the impedance, described as:

$$Z(t) = \frac{E(t)}{j(t)}$$

There are two types of EIS: potentiostatic EIS (PEIS) where the input is an alternating voltage, and galvanostatic EIS (GEIS) where the input is an alternating current. By varying the frequency of the perturbation, EIS allows for the observation of different processes occurring at different timescales. Higher frequencies highlight faster processes such as ion migration, while lower frequencies reveal slower phenomena like diffusion. In PEIS, the alternating voltage input ($E(t)$) can be expressed as

$$E(t) = |E| \sin(\omega t)$$

With $|E|$ represents the peak voltage amplitude, ω is the angular frequency, and t is time. It is crucial to ensure that the perturbation amplitude remains small (<50 mV) to maintain linearity and enable simplified data analysis by avoiding higher harmonic terms and minimising irreversible changes in the electrochemical system. Subsequently, current density can be represented as:

$$j(t) = |\Delta j| \sin(\omega t + \Delta t)$$

With $|\Delta j|$ being the amplitude of the current density, Δt the phase difference and $\omega t + \Delta t$ the phase angle (φ). The quantities, $E(t)$, $j(t)$, and $Z(t)$ can be represented as complex numbers, with $Z(t)$ having real and imaginary components referred to as $\text{Re}(Z)$ and $\text{Im}(Z)$ or Z' and Z'' , respectively [60]. These complex representations provide information about the magnitude and phase relationship between the voltage and current responses. These can be plotted in two different manners as seen in figure 3.6, b) a Nyquist plot, and c) a Bode plot. An "equivalent circuit" describes the behaviour of the electrochemical system as well as possible, by representing internal interfaces as a combinations of capacitors and resistors. In this case of an electrolyte, where R_0 describes the resistance of the wires and contacts of the system, the R_1 and C_1 elements describe the interface between the electrode and electrolyte, and C_2 describes a dielectric material.

It has to be taken into account, that the C_1 element is generally composed to several resistances [60]. One of those is the electrolyte resistance, and the other is either Warburg resistance, represented by a 45° line on the right side of the Nyquist plot, because due to the ion-blocking effect, one resistance part grows bigger linearly, while the capacitance doesn't change. This would only be the case in a one-dimensional system however. In a multi-dimensional system this Warburg impedance is replaced by a constant phase element (CPE). It's physical meaning is poorly understood, but it helps making proper fits to simulate the electrochemical system.

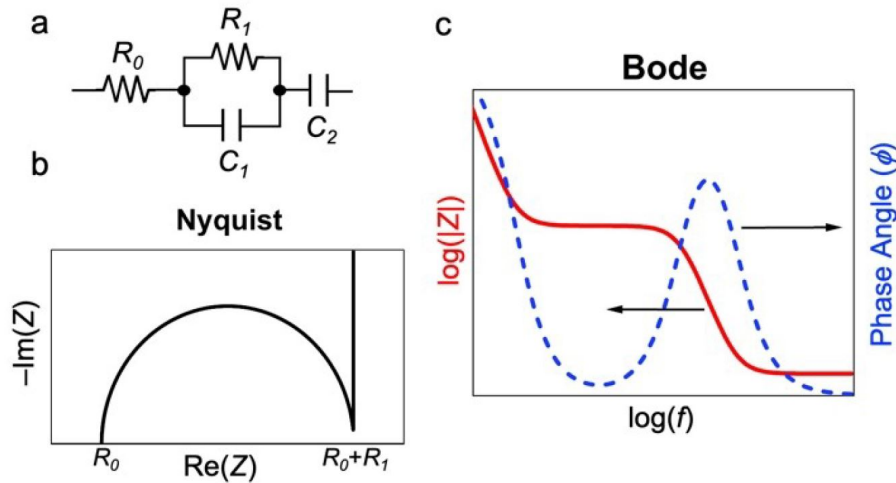


Figure 3.6: a) An equivalent circuit example of electrolyte. b) Nyquist plot of this system. c) Bode plot of this system. Reproduced from [60]

The Nyquist plot in figure 3.6 puts the imaginary impedance ($\text{Im}(Z)$) against the real impedance ($\text{Re}(Z)$) in a graph. One can observe a symmetrical arc offset from the origin on the x-axis. This offset corresponds to the resistance, R_0 , which includes resistances from wires and contacts. The impedance at the end of the semicircle provides an estimation of the electrolyte resistance, while the actual R_1 will be used in final calculations for the ionic conductivity of the electrolyte. This plot is most commonly used to derive useful data from the EIS measurements.

The Bode plot has the $|Z\Omega|$ and phase angle ϕ against the frequency of the pulses. A plateau followed by a slope is equal to a semicircle in the Nyquist plot. It is important to note that a Bode plot generally presents EIS measurements in time, instead of providing static information about the system. This facilitates relating impedance contributions to their temporal state.

The resistance obtained from the Nyquist plot can be used to calculate the ionic conductivity of the electrolyte, as the real part of the impedance gives the resistance of the material. Combined with the thickness and surface of the sample, this yields:

$$\sigma = \frac{L}{R \cdot A}$$

Where σ is the ionic conductivity in mS/cm , L is the thickness of the sample in cm , R is the resistance obtained from the EIS and A is the surface of the sample in cm^2 .

Electrochemical impedance spectroscopy can be used not only to determine the ionic conductivity as described in section 3.8, but also to study the electrochemical behaviour. To do so, the electrochemical cell is hooked up to the ECM10I Autolab using NOVA 2.1 and using a frequency response analysis (FRA) in a range from 10^7 to 10^1 Hz. The presence of one semicircle plus a 45° line is characteristic for a cell containing solely electrolyte, while the presence of a second semicircle indicates a second process happening in the cell. These systems are studied after measurement using the NOVA software to generate an equivalent circuit and a subsequent electrochemical circle-fit. Where the separate elements of the electrochemical circuit imitate the observed semicircles and lines in the Nyquist plot.

3.9. Galvanostatic Charging and Discharging

A commonly used and straightforward technique to assess the electrochemical behaviour of a battery cell is galvanostatic cycling. This destructive technique involves monitoring the voltage and charge evolution during repeated charge and discharge cycles, with the current incrementally increased. This

cycling protocol allows for the extraction of various important parameters for battery characterisation, including capacity and coulombic efficiency. Additionally, polarisation, hysteresis, and overvoltage phenomena can be observed to estimate the battery's performance.

To gain a more detailed understanding of electrochemical processes occurring during (dis)charging, it is common to utilise a potential vs. capacity representation, particularly focusing on an isolated cycle. This representation serves as a useful starting point for analysing the relationship between the electrode potential and the corresponding capacity changes, providing valuable insights into the electrochemical behaviour of the system. Especially as this curve provides insights into phase changes that occur during (dis)charging.

A voltage capacity curve consists of several regions of interest. These are displayed in figure 3.7. This includes the Ohmic drop at (1), which is an overpotential occurring at the beginning of charging [61]. It is the sum of all internal resistances of the cell, including electrolyte, electrode materials, cell components and the whole setup. Region (2) is the voltage plateau. Here the redox reaction of the cell happens, and a phase change is occurring. This can be used to determine both the capacity and efficiency of the cell. Then there is region (3), where the curve drops off. Here the active material in the cell is depleted. Allowing the (dis)charging to continue at this stage, will start affecting the electrolyte and carbon additives present in the cell, causing irreversible damage.

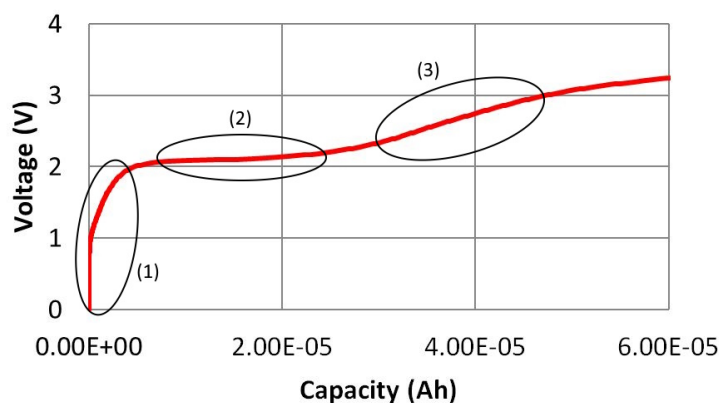


Figure 3.7: Representation of a voltage-capacity curve. Obtained during this project.

Throughout this report, the term "charged" will be used when electrons migrate from the top to bottom electrode, and "discharged" for electrons moving from the bottom to the top electrode. This indicates that oxidation occurs in the top electrode, and reduction occurs in the bottom electrode during charging. This is reversed in a discharge scenario.

In every cell, the electrode under study will have a calculated 1 mAh capacity, the other electrode always 2mAh (=61.2 mg) of the Pb/PbF₂ composite. This was done to facilitate the analysis and allow easier comparison of the separate voltage-capacity curves.

A MACCOR 4000a Automated Test System is used for galvanostatic (dis)charging of the electrochemical solid-state cells. Before operation, a program must be written to indicate the cut-off voltage, the current and charge mode. The cells are then hooked on the galvanostat and galvanostatically charged or discharged, depending on the cell composition, at 10 μ A, up to predetermined voltages. A voltage-capacity curve is the main outcome of this type of testing. It describes the amount of charge in mAh that has been used to charge or discharge the cell. This data is plotted against the necessary voltage needed to keep the current at a constant 10 μ A.

After the galvanostatic (dis)charging, a second impedance was taken to evaluate changes within the cell, and subsequently the relevant electrode composite was studied using X-ray diffraction. This is to obtain information about the cell composition.

3.10. X-Ray Diffraction

To analyse the structures in a non-destructive manner, X-ray diffraction (XRD) is used in this project. This method characterises mostly crystalline materials based on the lattice parameters, as this will give information about the involved structures and therefore the composition, as different materials have different crystal structures [62].

The device consists of an X-ray tube, that generates X-rays at an energy of generally 40 kV, which are subsequently directed at a powdered sample figure 3.8. The generated X-rays in the setup used copper as basis. The generated copper radiation consists of two wavelengths. The $K\alpha$ and $K\beta$ radiation. The β radiation has a much lower intensity with a wavelength of 1.39222 Å, which is why the $K\alpha$ radiation is used. This does consist of $K\alpha_1$ and $K\alpha_2$ however, with a ratio of 2:1. It has to be noted that their wavelengths are almost similar, 1.54056 Å and 1.54439 Å, which manifest themselves as some double-peaked patterns. Using a Ni-based monochromator, the $K\alpha_1$ and $K\beta$ radiation can be filtered out. Fluorescence can occur when a material absorbs photons of a particular wavelength and re-emits photons at a longer wavelength that overlaps with the copper X-rays. This emission interferes with the measurement and therefore the monochromator helps to filter out the other wavelengths to prevent said fluorescence.

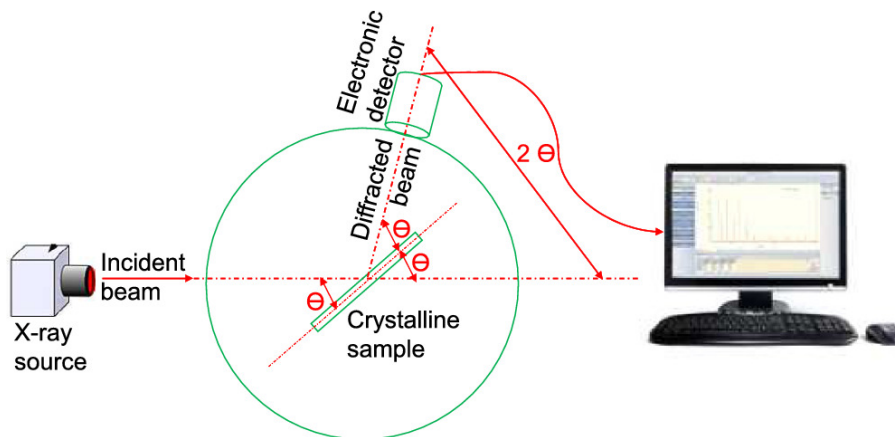


Figure 3.8: Schematic representation of XRD setup. Reproduced from [62]

The XRD technique used in this report is powder X-ray diffraction, the most commonly used and versatile technique that is capable of characterising multi crystalline samples [62]. Despite the easier sample preparation, if the sample contains multiple phases, there is often a significant peak overlap, which makes exact peak determination more difficult. Also in powder XRD, the incident X-rays interact with the individual crystalline particles, resulting in a scattering of intensity that forms cone-shaped patterns. The detector records these scattered intensities as rings with varying intensities. To identify the crystals present, we compare the peak intensity and d-spacing of the diffraction pattern with the information in an existing library. Using diffraction, the d-spacings are determined using Bragg's law:

$$n \cdot \lambda = 2 \cdot d \cdot \sin(\theta)$$

Where n is an integer corresponding to the order of reflection, λ is the wavelength of the X-ray in meters, d is the interplanar spacing in meter, and θ is the angle between the incoming X-ray and the horizontal surface of the sample. When the sample is measured over a large 2θ range, reflexes appear at angles where there is constructive interference. This will then yield a pattern that can be match with a library. For this, the Match! software will be used.

This technique is not flawless, and the errors associated with preparation and type of sample, and operation of XRD instrument contribute majorly towards peak analyses errors [63]. Two common errors are as follows:

Preferred Orientation Error: Preferred orientation error occurs when crystalline regions in a powder exhibit a stronger tendency towards a particular orientation compared to others. Random sample orientation is necessary for accurate identification of phases based on peak intensities. The presence of

preferred orientation introduces systematic errors in peak intensities. To minimize the variability caused by this, a rotating sample stage can be used.

Sample Displacement Error: Sample displacement error occurs when the movement of the sample causes X-ray diffraction (XRD) beams to miss the aperture of the detector. In figure 3.8, the displacement of a sample is created when the sample would be placed slightly to the top-left or bottom-right. This displacement leads to incorrect reporting of peak positions by the instrument. The displacement error (s) can be identified using the relation:

$$\Delta 2\theta = -\frac{2 \cdot s \cdot \cos(\theta)}{R}$$

Where R is the goniometer radius. For example, a displacement of $s = 0.30$ mm corresponds to a peak shift of 0.16° at $R = 200$ mm and $2\theta = 28.6^\circ$. The internal calibration and proper use of the sample stage generally help to avoid this problem.

During this study two different diffractometers were used. The samples were either measured using $K\alpha_1$ and $K\alpha_2$ radiation from a copper X-ray tube in a PANalytical X'Pert pro X-ray diffractometer at 45 kV and 40 mA, or a Bruker D8 Advance diffractometer with Bragg-Brentano geometry. Also using Cu $K\alpha$ radiation at the same voltage of 45 kV 40 mA. A divergence slit is used: V12. The diffracted beam filter is nickel-based, soller slit of 2.5 deg. It also uses a LynxEye position-sensitive detector with the settings of LL=0.19 W=0.06.

The samples consisting of the battery cell pellet used for EIS and galvanostatic cycling was extracted under an argon atmosphere and placed in an airtight XRD sample holder. Kapton film was used to cover the sample as seen in figure 3.9. The sample was measured for a duration depending on the presence of iron. If any $Fe_xO_xF_z$ was present in the electrode composition, the measurement was done overnight (8 hours) and a beam monochromator was used to filter out the iron fluorescence. The measurement time for a regular sample was half an hour. Both types of measurement scanned the 2θ range of 5° - 90° .

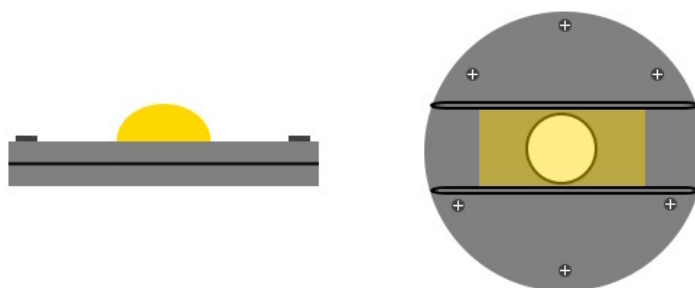


Figure 3.9: Schematic representation of kapton film-covered XRD sample holder

The XRD patterns obtained from the diffraction were analysed using the Match! software developed by Crystalimpact in combination with the Crystal Open Database (COD). This software was also used for cell refinement using the integrated FullProf Rietveld refinement. This software also allowed for a Le Bail fit of the obtained pattern, which is initially used to find the lattice parameters in the sample, as well as the lowest possible χ^2 and R^2 obtainable by Rietveld refinement.

Results & Discussion

In this results section, first the Pb/PbF₂ will be discussed, to evaluate whether this will function as a suitable counter- and reference electrode. After that the PK10 electrolyte will be tested to find whether it is sufficiently conductive and stable, and lastly the FeO itself will be tested. Of these separate components, first the materials will be evaluated, followed by their electrochemical performance. After this, the iron oxyfluoride will be assessed on performance.

4.1. Materials and Synthesis

To perform the necessary experiments, the cathode and anode composites were synthesised, as well as the PK10 electrolyte, see section sections 3.1, 3.3 and 3.4. This is because these materials are not commercially available. X-ray diffraction measurements were taken of all precursors and synthesised materials to validate the composition. This is done by Rietveld refinement and/or phase composition analysis based on the reference intensity ratio, I/I_c (c = corundum).

4.1.1. Pb/PbF₂ Composite and Precursors

The Pb/PbF₂ composite has been synthesised and subsequently analysed as described in section 3.1. This composite is used as counter electrode in every solid-state cell fabricated during this project, and by XRD analysis of the composite and its precursors, the electrochemical changes in the material can be understood. Rietveld refinement was conducted on the XRD patterns to find the composition of the material.

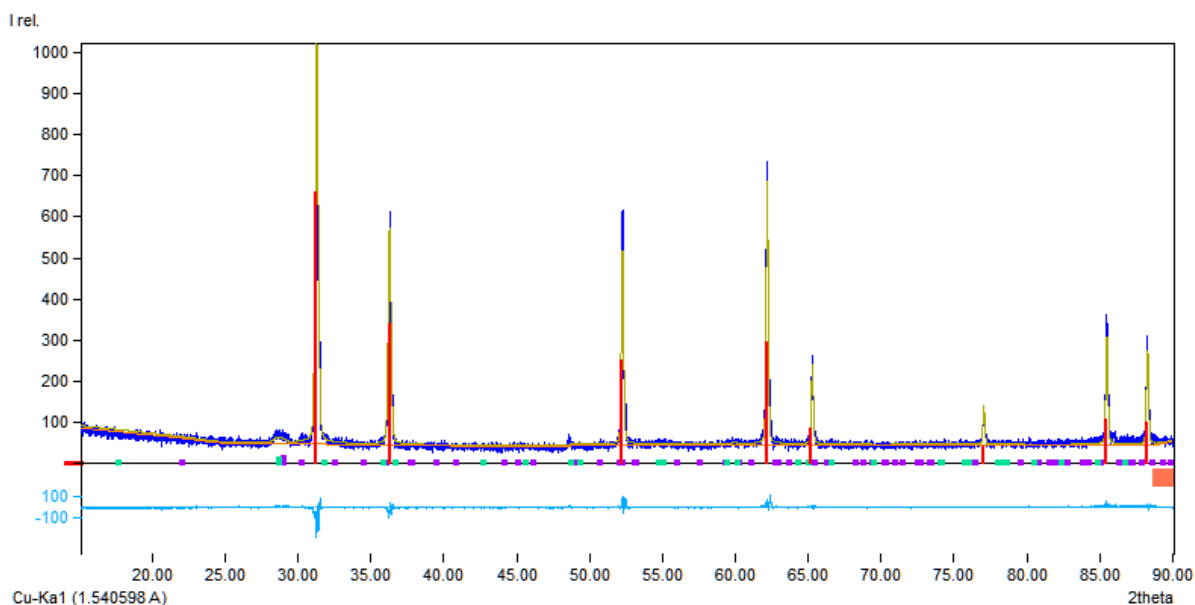


Figure 4.1: Refinement of the XRD measurement of the lead powder precursor. The red bars indicate cubic lead, while green and purple indicate litharge and massicot respectively, polymorphs of PbO

In figure 4.1, the XRD pattern of metallic lead (Alfa/Aesar, 99.9% purity), precursor for the Pb/PbF₂ composite, and its refinement is shown. We expect to see only the peaks belonging to cubic lead,

displayed in table 4.1 with three more peaks at higher angles. This pattern would indicate a phase-pure cubic lead phase (COD entry: 96-153-1229), indicated in figure 4.1 by red bars. Despite this, we also find other significant reflexes, seen in table 4.1. Matching and subsequent refinement found that these peaks belong to two polymorphs of lead(II) oxide. Namely litharge, orthorhombic space group $Cmma$, depicted by the green bars (COD entry: 96-901-2697), and massicot, orthorhombic space group $Pbcm$, depicted by the purple bars (COD entry: 96-900-7711).

Phase + COD entry	2θ angle ($^{\circ}$)	hkl index
Metallic lead 96-153-1229	31.3	(111)
	36.3	(200)
	52.2	(202)
	62.2	(311)
	65.2	(222)
Litharge and Massicot 96-901-2697 and 96-900-7711	28.6	
	29.1	
	30.3	
	31.9	
	32.6	
	48.6	

Table 4.1: Overview of the reflexes of metallic lead, litharge and massicot, indexed in figure 4.1

The presence of these phases is most likely caused by the oxidation of the metallic lead. The amount of massicot and litharge, respectively 2.5% and 1.6%, are low; 95.9% of the cubic lead phase remains. This will most likely not affect the properties significantly. However, as the oxides are often present on the outside of the particles, this might inhibit the ionic and electronic conductivity of the material, which then would cause capacities to be lower than expected.

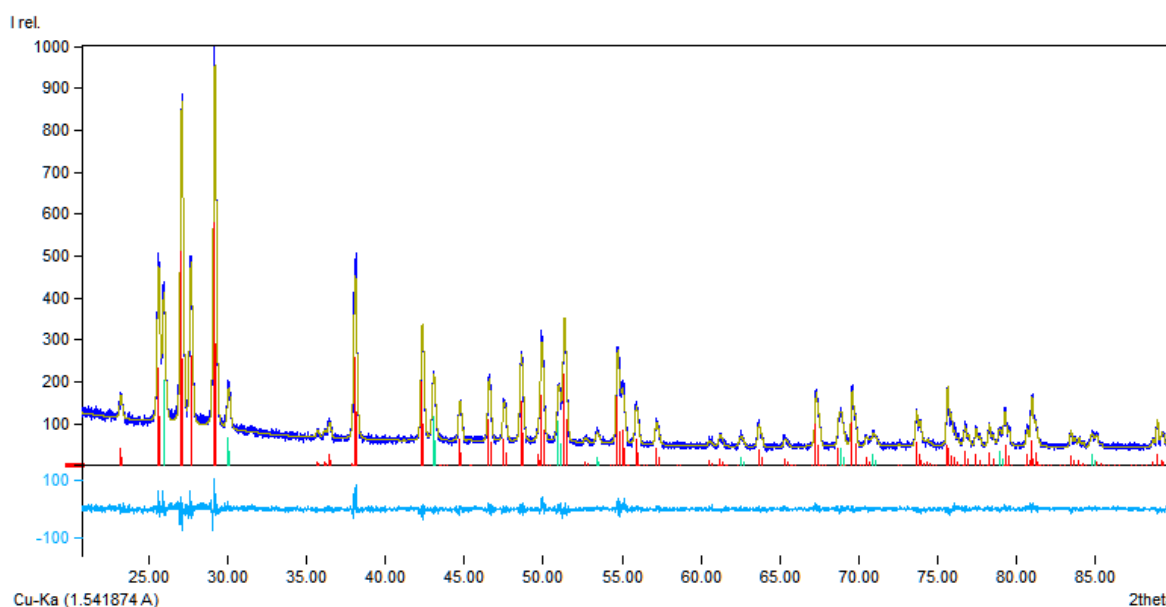


Figure 4.2: Refinement of XRD measurement of the lead(II) fluoride precursor. Red bars indicate orthorhombic PbF_2 , green bars indicate the cubic polymorph: Fluorocronite

Figure 4.2 is the refined XRD pattern of PbF_2 (Merck, 99% purity), used as precursor for the Pb/PbF_2 composite, as well as the PK10 electrolyte. This material is found in two polymorphs with either an orthorhombic or cubic structure, therefore we expect to see both of them. The main reflexes of the orthorhombic lead(II) fluoride are stated in table 4.2 in decreasing intensities. Reflexes are found at

these exact locations, and attributed to the orthorhombic PbF_2 phase using red bars (COD entry: 96-231-0347). For the cubic lead reflexes are expected as stated in table 4.2, also at decreasing intensities. These are again indexed and indicated with green bars (COD entry: 96-901-4558). In this diffractogram, the $\text{K}\alpha_2$ radiation has not been removed, causing the doublets.

Phase + COD entry	2θ angle ($^\circ$)	hkl index
Orthorhombic PbF_2 96-231-0347	29.2	(111)
	27.1	(102)
	25.6	(001)
	27.7	(200)
Cubic PbF_2 96-901-4558	26.0	(111)
	43.0	(220)
	51.0	(331)
	30.1	(200)

Table 4.2: Overview of the reflexes of both polymorphs of PbF_2 , indexed in figure 4.2

It is clear that in figure 4.2 no peaks are present that do not belong to either orthorhombic or cubic PbF_2 . The ratio between orthorhombic:cubic is 86.5:13.5. This is a relevant observation, as this will be used to verify which lead(II) fluoride polymorph is more likely to react, and which polymorph is more likely to form upon electrochemical fluorination of the metallic lead.

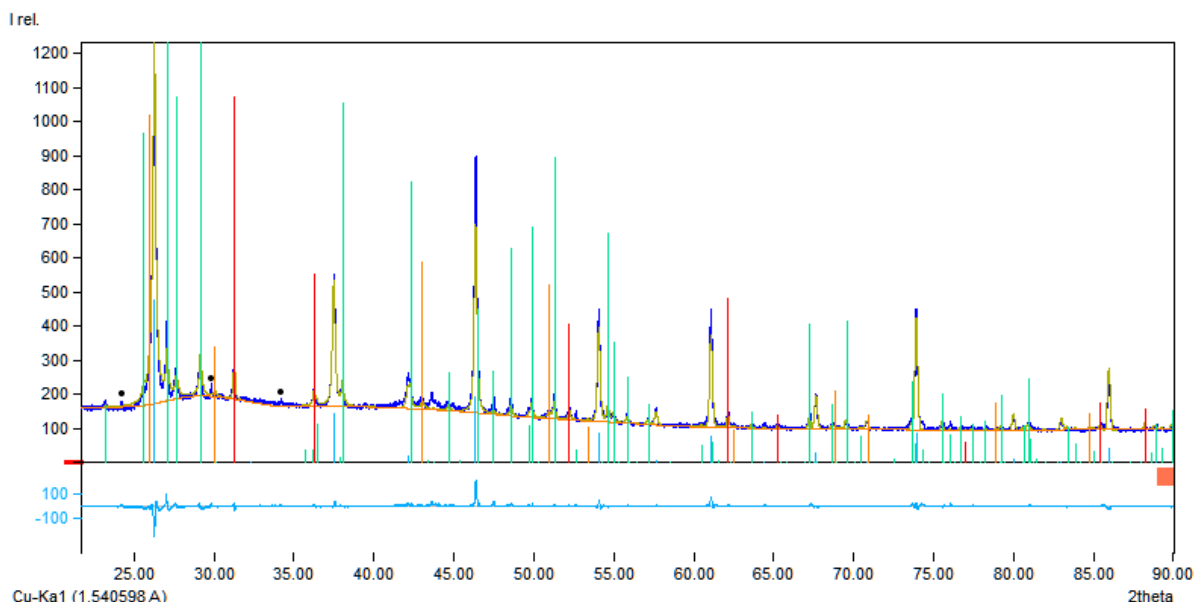


Figure 4.3: Refinement of XRD measurement of the first synthesis of the Pb/PbF_2 composite. Red indicates metallic lead, blue the PK10 solid-state electrolyte, green orthorhombic PbF_2 and orange cubic PbF_2

Figure 4.3 shows the refined XRD pattern of the synthesised Pb/PbF_2 composite. The reflexes of both the orthorhombic and cubic polymorph of PbF_2 are present, respectively green and orange bars. Also cubic lead is present, denoted by red peaks. Massicot is also detected, grey bars, but the litharge is in such a low concentration, no traces of this phase could be found. All of these phases are described above, and their presence is expected. In addition to this, there are also peaks present at $2\theta = 26.3^\circ$ (101), $2\theta = 46.4^\circ$ (211) and $2\theta = 37.5^\circ$ (200) in decreasing intensity. These, and a few other peaks at a higher 2θ range belong to the PK10 electrolyte, blue bars. Three other small unidentified reflexes have been observed at $2\theta = 24.2^\circ$, $2\theta = 29.8^\circ$ and $2\theta = 34.2^\circ$, marked with black circles. Also, according to the refinement, the phase composition is equivalent to 54:6:40 for PK10:Pb: PbF_2 . This is deviating from the composition used for synthesis of the composite, namely 60:15:15:10 for PK10:Pb: PbF_2 . The composition of the lead(II) fluoride polymorphs, orthorhombic:cubic, is the similar to the virgin lead

fluoride, 82:18. A broad bump in the XRD pattern starting at $2\theta = 25^\circ$ sloping down to $2\theta = 60^\circ$ is also observed.

The lead precursors are phase-pure enough to be used in the synthesis of the Pb/PbF₂ composite. However, upon synthesis of the composite, Rietveld refinement yielded a phase composition of 54::6:40 for PK10:Pb:PbF₂. While deviation of PK10 is understandable, the balance between lead and lead(II) fluoride is not. The most likely explanation is that during grinding of the material, the lead became amorphous due to its high malleability and forces present during the grinding. This is confirmed by the presence of the bump between $2\theta = 25^\circ$ and $2\theta = 60^\circ$. This might affect its electrochemical performance, but as for these purposes generally an excess of composite is used, a lower fraction should still be able to provide enough capacity to function as anode. This is even more true for the lead(II) fluoride part of the composite, which is more than able to release enough fluoride ions to fluorinate the FeO anode. While the initial composition should have a cathode capacity of 32.8 mAh/g, PbF₂ + 2e⁻ → Pb⁰ + 2F⁻, the capacity according to the refinement is 87.4 mAh/g. That should cause no complications when this material is used as cathode. If the composite is used as anode however, with a reaction of Pb⁰ + 2F⁻ → PbF₂ + 2e⁻, this is not the case. Instead of an expected capacity of 38.8 mAh/g, only 10.3 mAh/g would be available. This means a significantly higher amount of composite should be used. This will be confirmed during electrochemical testing.

4.1.2. Electrolyte

CsPb_{0.9}K_{0.1}F_{2.9}, abbreviated as PK10, was used as electrolyte in this research. A total of six batches was utilised in total, to be used as electrolyte on itself and in the production of electrode composites. Of these, one batch was synthesised by another researcher in the group, while the other four batches were synthesised during this project [64]. The older sample exhibited a conductivity of 0.36 mS/cm and was used to create the first few electrode composites and cells. The other four batches of PK10 were all mechanically synthesised and X-Ray diffraction, electrochemical impedance spectroscopy, and thickness measurements were performed as described in section section 3.3. This is done to validate the material. The measurements will be discussed and evaluated here.

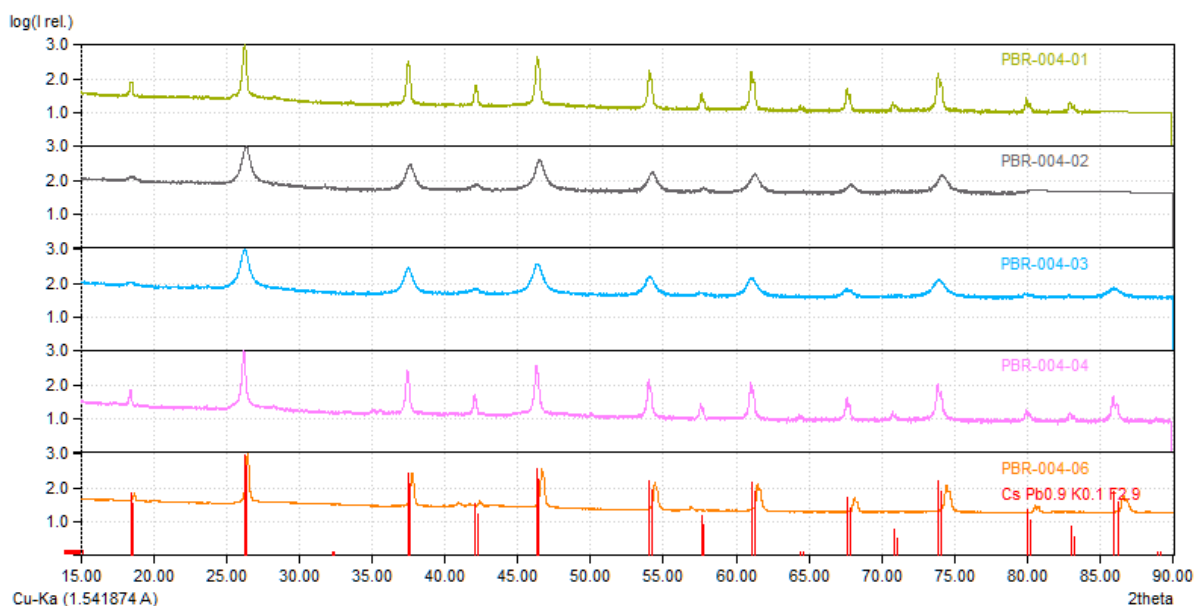


Figure 4.4: XRD patterns of Different Batches PK10, synthesised and refined

The XRD diffraction data and refinement of the different batches of the synthesised PK10 solid state electrolyte is displayed in figure 4.4. The main reflexes of this material are present as stated in table 4.3. The structure of this material is cubic, with space group Pm $\bar{3}$ m. While an existing reference exists (COD entry: 96-152-5673), this is for CsPbF₃. Therefore a modified reference was created with modified occupancy of potassium, lead and fluoride and varying bise parameters to accommodate for the vacancies. Using this for refinement yields the results in figure 4.4. Refinement yields a different

lattice parameter compared to normal CsPbF_3 , see table A.1 in appendix A. This is due to potassium doping at the lead sites in the perovskite structure. But as this is just 10% potassium, the crystal structure does not change, only the lattice parameter has been reduced from 4.798Å to 4.794Å [2]. It has to be noted that the peak at $\theta = 18.49^\circ$ is absent in batch 3, denoted in figure 4.4 as PBR-004-03. Refinement of this structure concluded that this phase is actually $\text{CsPb}_{0.99}\text{K}_{0.01}\text{F}_{2.99}$, PK01.

Phase + COD entry	2 θ angle ($^\circ$)	hkl index
Cubic $\text{CsPb}_{0.9}\text{K}_{0.1}\text{F}_{2.9}$ 96-152-5673	26.18	(101)
	37.40	(200)
	46.28	(211)
	53.98	(202)
	61.00	(302)
	73.48	(321)

Table 4.3: Overview of the reflexes of CsPbF_3

The synthesised PK10 was pressed into a pellet in a solid-state cell to measure the impedance as mentioned in section 3.3, and Nyquist plots are obtained plotted in figure A.1, found in appendix A. The thickness of the pellet was measured and averaged over 5 different locations on the pellet. The impedance data was fitted using an electrochemical circle-fit as described in section 3.8, and using the formula stated in section 3.8, the ionic conductivity could be obtained. This is tabulated in table 4.4.

PK10	Impedance (Ω)	Thickness (cm)	σ (mS/cm)
Batch 1	212	0.601	0.36
Batch 2	305	0.602	0.25
Batch 3	1020	0.493	0.06
Batch 4	287	0.505	0.22
Batch 5	290	0.569	0.25
Batch 6	202	0.570	0.36

Table 4.4: Calculated ionic conductivity of the electrolyte in mS/cm per batch, including the experimentally obtained parameters

Table 4.4 contains the impedance, the $R_{\text{electrolyte}}$, as well as the thickness measurements, and the resulting conductivity. Batch 1 and batch 6 have the highest ionic conductivity of 0.36 mS/cm. Batch 2, 4 and 5 have a slightly less ionic conductivity, but this is still close to the BaSnF_4 that has been used in earlier research with fluoride ion batteries [29]. Therefore these batches are also considered successful. Batch 3 has an ionic conductivity of just 0.06 mS/cm however. This is attributed to the low potassium content, inducing not enough fluoride vacancies in the perovskite structure. Insufficient fluoride vacancies lead to a significantly worse ionic conductivity compared to materials with a higher potassium content. Therefore this material is deemed unsuitable to be used as solid-state fluoride ion conductor, and is the only failed electrolyte synthesis.

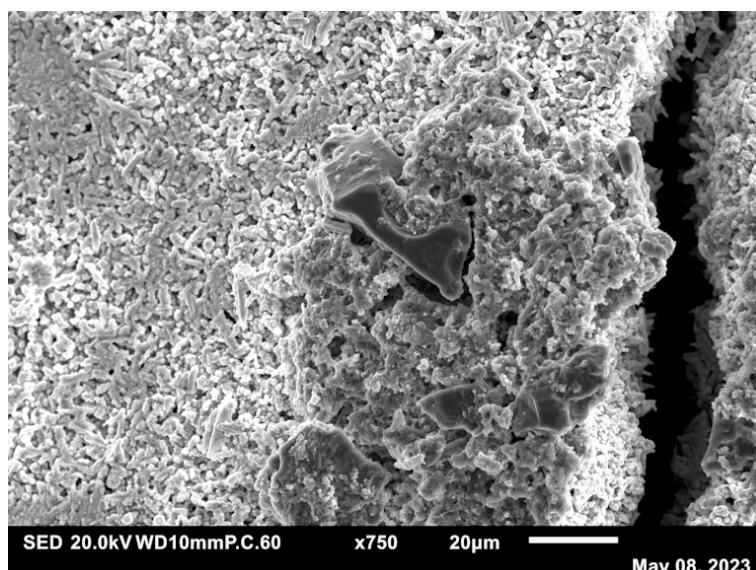
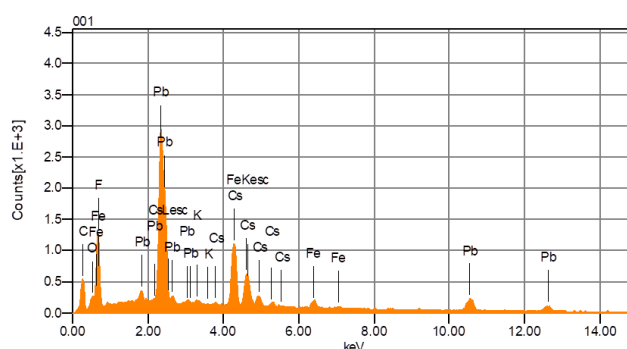
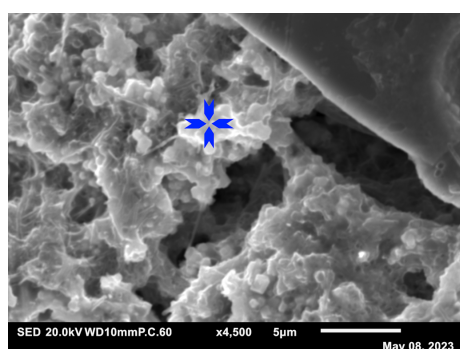


Figure 4.5: SEM measurement of pressed PK10 electrolyte pellet, 750x zoom. The scale bar is 20 μm

SEM was used to determine the particle size of the ball-milled PK10, part of a used pellet is displayed in figure 4.5. During cell fabrication, this pellet has been pressed up to 50 bar. This caused the individual PK10 particles to agglomerate and make sufficient contact to allow ionic conductivity. Analysis of the surface of the pellet resulted in an observed particle size of 0.4 μm with a low size distribution. This is in accordance with earlier reports of this material, which recorded regularly sized particles of 0.35 μm [2]. As mentioned there, the relatively large size of the particles is probably beneficial for the ionic conductivity, as inter-crystallite ionic transport is generally considered difficult.



(a) SEM measurement of pressed PK10 electrolyte pellet, 4500x zoom. **(b)** EDS analysis of a pressed PK10 pellet, plotting the counts against the X-ray energy, measured at the blue indicator
The scale bar is 5 μm

Figure 4.6: SEM and EDS measurement of pressed PK10 electrolyte pellet

Figure 4.6 shows a zoomed in version of the SEM measurement as well as a EDS measurement at that location. Reflexes are seen of Cs, Pb, F and K as expected. The carbon present is of the adhesive tape, while the iron and oxygen present are there due to this pellet being part of a FeO cell, and this side was attached to the FeO composite. Part of the FeO can be seen top right in figure 4.6a. The composition according to EDS measurements of Cs:Pb:K:F is 1:1.21:0.06:2.96. While this is a higher content of lead compared to cesium, the potassium and fluoride have expected values.

Six batches of the PK10 electrolyte have been synthesised. Rietveld refinements were performed on the $\text{CsPb}_{1-x}\text{K}_x\text{F}_{3-x}$ batches to obtain the lattice parameter and potassium content of every electrolyte used. This can be used to justify the ionic conductivity of the different batches. As observed, there is a correlation between lattice parameter and potassium content, which is as expected. It is noticeable that batch 3 has a significant lower concentration and higher lattice parameter compared to the other

batches. This is more similar to PK00 than PK10, that already agrees with the lower conductivity observed in the EIS measurements. Furthermore, broader peaks and an enhanced background can be observed in batch 2 and 3. While the peak broadening can be related to crystallite size, the ball-milling time and other preparatory actions were identical to the other preparations. This is then attributed to the measurement errors mentioned in section section 3.10.

The impedance and conductivity measurements conducted, agree with the phase purity and composition observed in the XRD measurements and Rietveld refinement. A conductivity of 1.23 mS/cm was obtained originally by Wang et al. [21]. While this is almost 4 times as high, a conductivity of 0.22 mS/cm is still sufficiently conductive to obtain reliable measurements at room temperature. As seen in the SEM image, the packing of the individual electrolyte particles is good, and suitable as solid-state ion conductor. The EDS measurement detected a higher lead content compared to cesium. This is different from the XRD refinements. As the XRD measures a significantly larger part of the sample, and refinement of this measurement does not show such significant deviations from the expected stoichiometry, the EDS results are attributed to local variance. Despite this, all batches except batch 3 are fully suitable to be used as solid-state electrolyte for the purpose of this report.

4.1.3. FeO Composites and Precursors

Different FeO composites were synthesised and the FeO precursor was obtained from two different suppliers as described in section 3.4. The FeO precursors were analysed using XRD and refined to obtain the proper phase composition. These composites were later used to evaluate the fluorination behaviour of the FeO using galvanostatic charging.

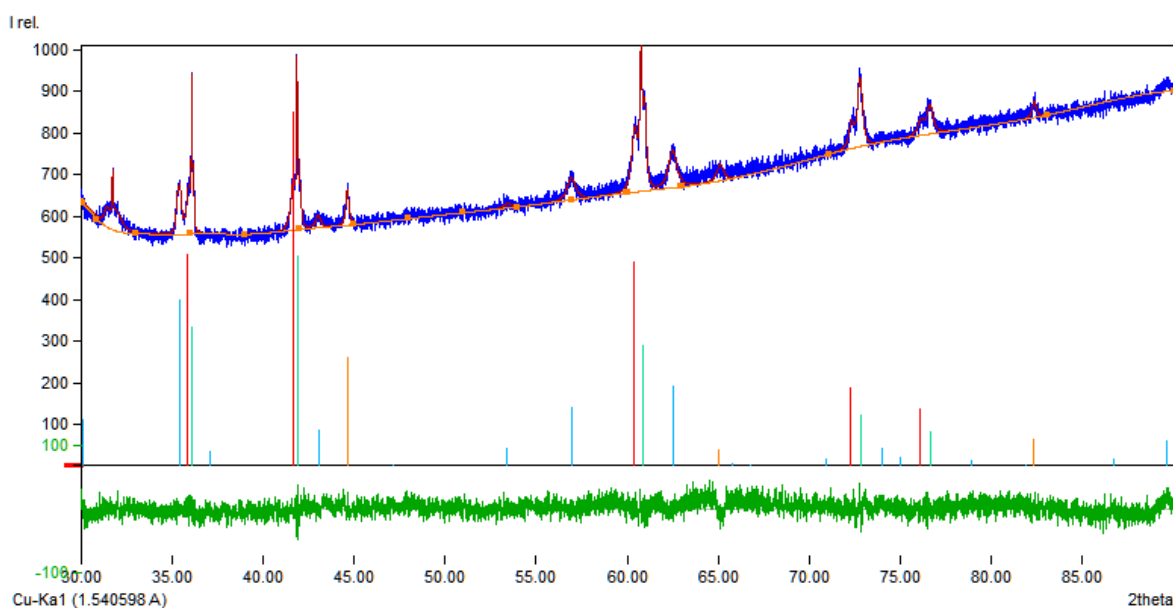


Figure 4.7: Refinement of XRD measurement of FeO, obtained from Thermo Fisher. Red bars indicate iron deficient FeO, green bars stoichiometric FeO, blue bars magnetite, Fe_3O_4 and orange bars metallic iron

Figure 4.7 shows the XRD pattern and subsequent refinement of the FeO precursor (Thermo Fisher, 99.5% purity), and the subsequent refinement. This being ferrous oxide, it is a cubic crystal with a space group of $\text{Fm}\bar{3}\text{m}$. The main reflexes of this material would be $2\theta = 42.30^\circ$ (200), $2\theta = 36.11^\circ$ (111) and $2\theta = 60.79^\circ$ (202), in decreasing intensity. These are indeed observed, and FeO is found (COD entry: 96-101-1199). However, a shifted pattern of this is found as well. This matches with iron deficient wüstite, $\text{Fe}_{0.924}\text{O}$ (COD entry: 96-152-3719). Besides this, other peaks are observed as well. At $2\theta = 35.53^\circ$ (131), $2\theta = 62.71^\circ$ (404), $2\theta = 57.12^\circ$ (151) and $2\theta = 30.47^\circ$ (202) in decreasing intensity. These belong to magnetite, Fe_3O_4 (COD entry: 96-900-6195). This was found along iron (COD entry: 96-900-0658) with peaks at $2\theta = 44.63^\circ$ (101), and $2\theta = 82.36^\circ$ (211). This fully indexes the XRD pattern, refinement of the pattern find that this substance contains FeO, Fe_3O_4 and α -iron in a weight ratio of 74:20:6. This is more than suitable to evaluate whether FeO can be fluorinated or not.

The FeO obtained from Thermo Fisher was compared to the FeO obtained from Merck (99.9% purity), see appendix A. There it was found that this substance contains a significant amount of Fe_3O_4 , Fe and Fe_2O_3 compared to FeO. This in a ratio of 56:1:9:34. As this material contains only 34% of FeO, its capacity is significantly, and more of the side phases will be involved in the reaction. Therefore this material is less suitable to evaluate the fluorination behaviour of FeO. Despite that, both materials were made into a composite as described in section 3.4.

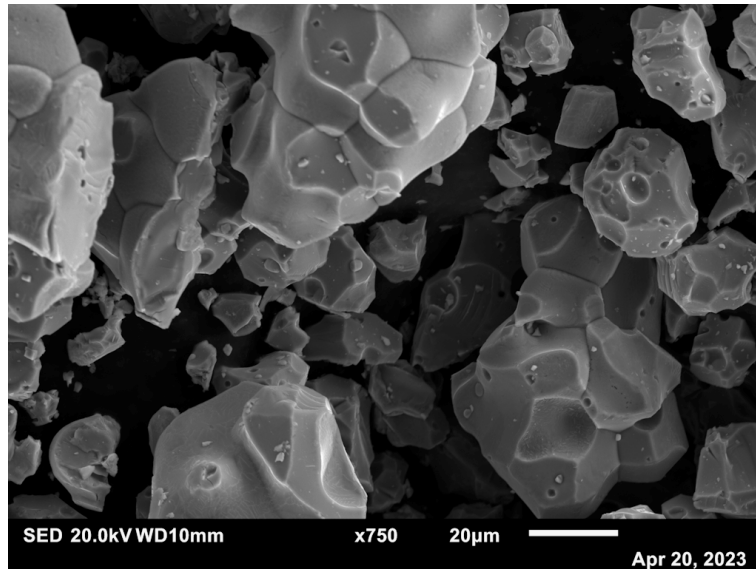
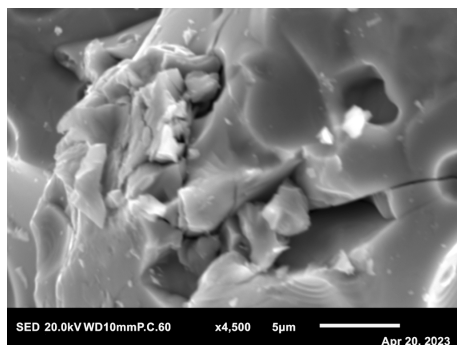
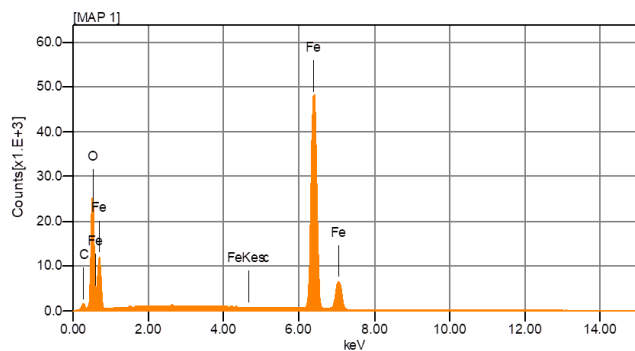


Figure 4.8: SEM measurement of FeO, 750x zoom. The scale bar is 20 μm

The FeO from Thermo Fisher was also studied using SEM and EDS as seen in figures 4.8 and 4.9. These are the particles of FeO that have been ground. As seen in the image above, the particle size of the individual FeO grains is not uniform. The size varies from 5 to 50 μm , or even smaller. This is relatively big, and has been taken into account when synthesising the composite, as this large size might hamper fluorination when the cell would be galvanostatically charged due to low fluoride-ion conductivity in the FeO lattice.



(a) SEM measurement of FeO, 4500x zoom. The scale bar is 5 μm



(b) EDS analysis of the FeO precursor, plotting the counts against the X-ray energy, measurement encompasses the whole picture

Figure 4.9: SEM and EDS measurement of unmodified FeO

Figure 4.9 shows a higher zoom of the FeO precursor as well as an EDS measurement of the full image, not just one point. This was done to gain insight in the full outside of the FeO grain. As expected, a low amount of carbon is present, whose X-rays are detected due to interaction with the surroundings. Also, there is an atomic Fe:O distribution of 62.1:37.9. This implies that there is more iron than oxygen present on the surface of this grain. Therefore the outside composition is not a stoichiometric FeO,

but rather a polymorph that is significantly less oxidised. But this is just observed in the outside of this particles, and XRD measurements would imply that the inside would have a higher oxygen content.

As described in section 3.4, either material was mixed with PK10 electrolyte and carbon nano-tubes in a 30:60:10 weight ratio. These composites were also studied with XRD. This concerns a composite using the FeO obtained from Thermo Fisher, figure 4.10, and a composite using the FeO obtained from Merck, figure 4.11.

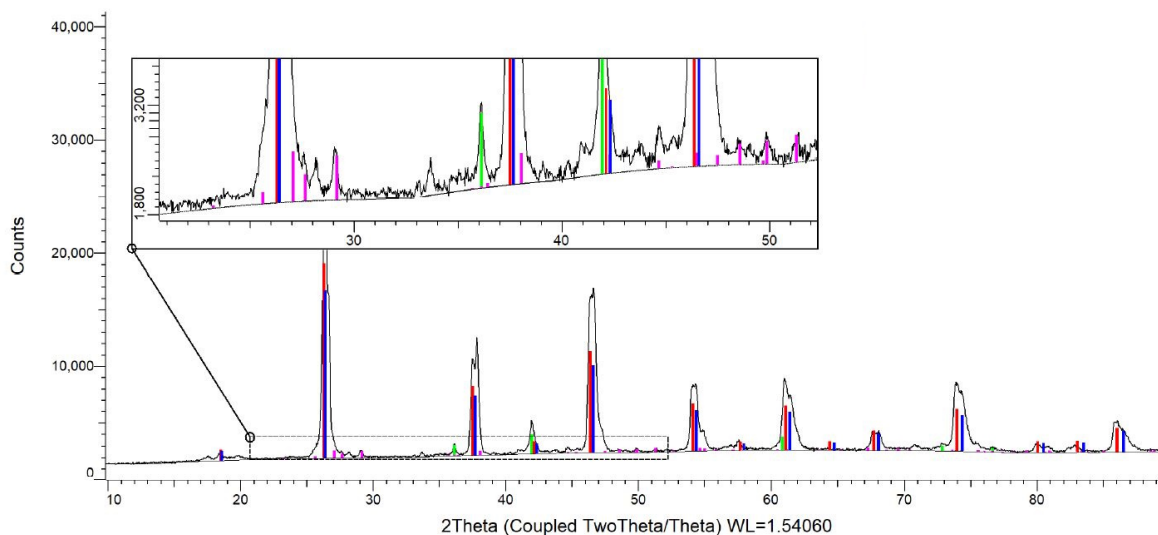


Figure 4.10: X-ray diffraction measurement of electrode composite with FeO, obtained from Thermo Fisher. Red and blue bars indicate the PK10 electrolyte, green bars FeO, and purple bars the PbF₂

An XRD measurement was taken of the composite synthesised with FeO from Thermo Fisher, called FeO 1, as seen in figure 4.10. No quantitative analysis was possible, although the XRD pattern seems to neatly indicate two types of the PK10 electrolyte, one with a slightly different lattice parameter. There also seems to be PbF₂ present, an amount in the range of a few percent at most. While the general composition of this composite aligns with the reflexes of the precursors, the presence of PbF₂ is surprising. The lead(II) fluoride will not be able to participate in the electrochemical reactions when this composite is fluorinated. Especially as the PbF₂ is present in a very low quantity, and the reaction potential lies above the ESW of the electrolyte. Apart from this anomaly, the composition of this composite is suitable to be used in an electrochemical solid-state cell.

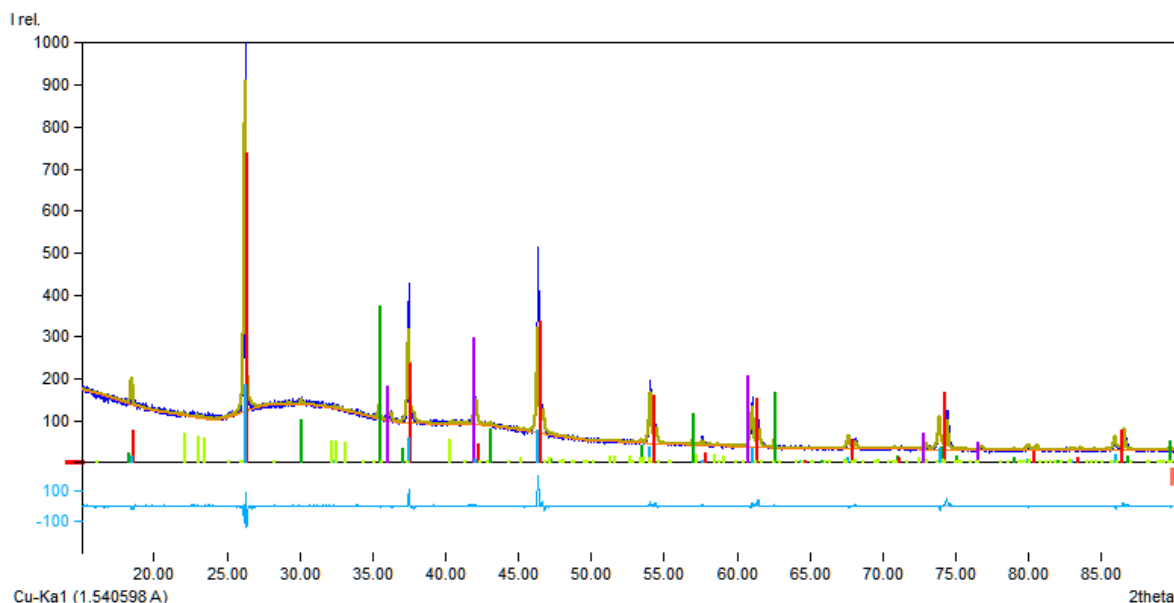


Figure 4.11: Refinement of XRD measurement of electrode composite with FeO obtained from Merck, Red and blue bars indicate the PK10 electrolyte, purple the FeO, green the Fe₃O₄ and lime the α -iron

As seen above, the composite with FeO obtained from Merck, called FeO 2, contains, according to the XRD and Rietveld refinement, about 11% FeO. This agrees with the composition of the precursor, which contains 34% FeO. Apart from this, the composite does not contain any peaks that deviate from the precursors. As seen, it does contain a few very broad low peaks, from a log angle up to $2\theta = 25^\circ$, and from there to $2\theta = 50^\circ$. This is related to the carbon in the sample, and contributes in this way to the background of the sample. Due to the low FeO content, it is disputable whether this can be sufficiently used as cathode material in a solid-state cell.

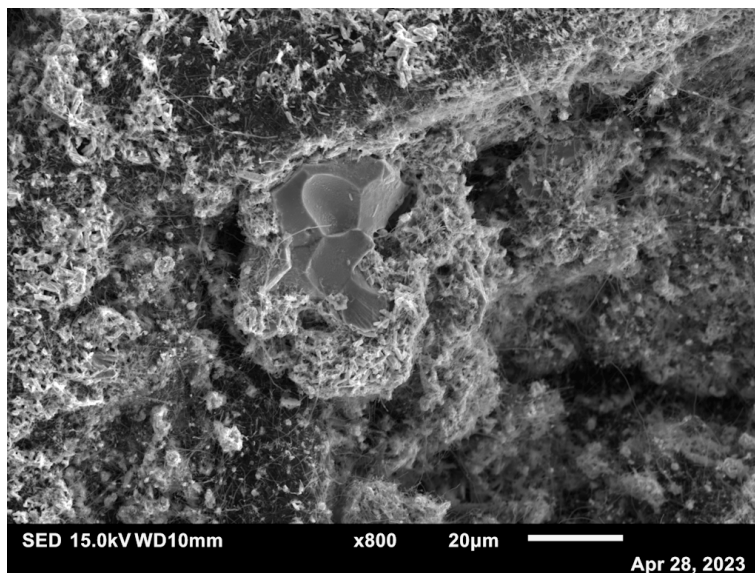


Figure 4.12: SEM measurement of FeO composite with Thermo Fisher, 800x zoom. The scale bar is 20 μm

In figure 4.12, the prepared composite is depicted. As observed, the grains of FeO are very large. Due to this small surface area compared to bulk volume of the material, this may be very detrimental for the electrochemical performance, as the fluoride-ions will have difficulty penetrating into the FeO lattice. Therefore the FeO underwent ball-milling as described in section 3.4. This yielded figure 4.13, and is called FeO BM, the FeO composition did not change during the ball-milling, appendix A.

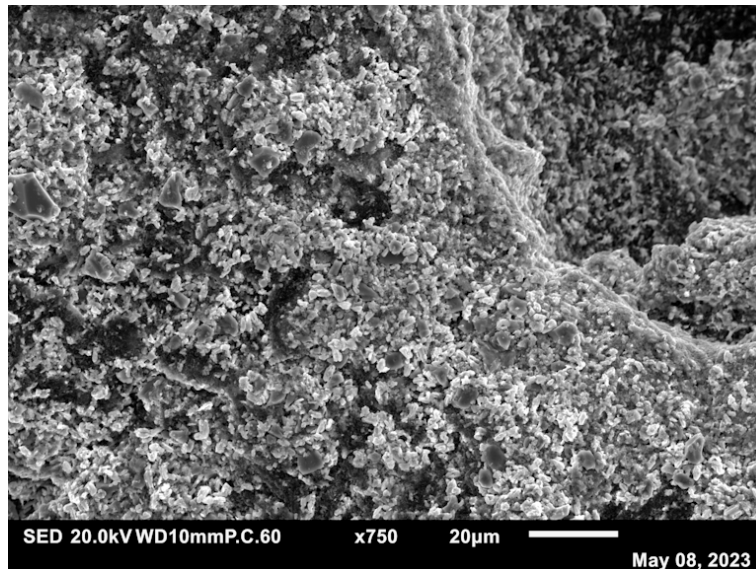


Figure 4.13: SEM measurement of ball-milled FeO composite with Thermo Fisher, 1300x zoom. The scale bar is 10 µm

As seen in figure 4.13, the particle size of the PK10 and particle size of the FeO particles are now more similar. This should enhance the contact between the iron oxide particulates and both the PK10 electrolyte and carbon nanofibers. The XRD and subsequent refinement of this composite, found in appendix A, show no presence of different phases. Therefore this composite is most suitable to be used as composite for the solid-state cells, and will be used.

The FeO composites that have been synthesised are all capable of being used in an electrochemical solid-state cell to evaluate whether FeO can be fluorinated. Both suppliers of the ferrous oxide indeed do contain FeO, but the FeO obtained from Merck has significantly more contaminants than the FeO obtained from Thermo Fisher. To understand why those contaminants are present in the sample, the phase diagram of iron oxide must be investigated, and is displayed in figure 4.14.

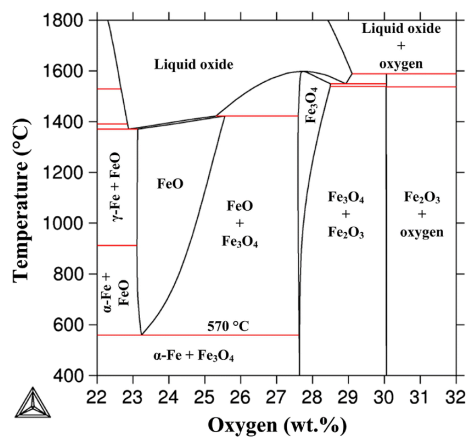


Figure 4.14: Phase diagram of FeO. Reproduced from [65]

As seen in figure 4.14, the wüstite phase, FeO, the investigated material is not thermodynamically stable at room temperature. It is only stable at temperatures above 600 °. Therefore, for production of FeO, the material is synthesised at high temperatures, and then quenched to room temperature. At this lower temperature, the FeO does not have enough energy to convert back to α -iron and Fe_3O_4 , and will maintain its structure [66]. If this quenching does not occur at a sufficient rate, the FeO will still decompose, yielding the contaminants present in both FeO samples used for this project. From there on we can speculate that the FeO of Merck was slower quenched, yielding more Fe_3O_4 , but as apparent from the phase diagram, and increased presence of oxygen also causes this. Due to this

phenomenon, the obtained can almost never be truly phase-pure, and the FeO obtained from Thermo Fisher is concluded to have sufficient quality to solely investigate the fluorination behaviour of FeO.

The fact that the FeO found is partially iron deficient is not uncommon either, as the FeO might slowly oxidise, causing the oxidation of some iron atoms in the FeO lattice from Fe^{2+} to Fe^{3+} . While these atoms will not be able to part-take in the electrochemical fluorination, as this also oxidises the iron, the percentage of atoms affected by this not significant enough to modify the structure nor the electrochemical activity of the ferrous oxide.

While two composites, FeO 1 and FeO BM, were deemed suitable to evaluate the electrochemical properties of the FeO due to their composition, particle size remains relevant. 5 to 50 μm is relatively big for ground particles of FeO 1. However, as shown for the PK10 electrolyte, the particle size of the electrolyte is very low, on average 0.4 μm . Therefore the electrolyte is able to fully encompass the FeO when a composite is made out of it. There is a possibility that this might convert the full surface, but only the surface of the bigger particles. As FeO is not a good fluoride-ion conductor naturally, the composite with the smaller particles, FeO BM is chosen as the most suitable composite to evaluate the electrochemical behaviour of the ferrous oxide.

Assuming that none of the FeO has reacted yet in this composition, as there is no evidence of this happening, the approximate capacity of this composite is 101.8 mAh/g. This is 2.5 times higher than the composite synthesised using the ferrous oxide supplied by Merck. Therefore, reactions observed using this composite will very likely be originating from the FeO phase of this composite, as long as the voltage range is within the ESW of the electrolyte. We can conclude that because of this, The FeO BM composite is most suitable to study whether FeO can be electrochemically fluorinated.

4.2. Electrochemical Performance

The electrochemical characteristics of all involved materials is evaluated and compared by integrating these materials in solid-state electrochemical cells. The Pb/PbF₂ anode has been assessed to compare the actual capacity of the composite, this was to verify that there is always an excess of fluoride ions or lead ions available to be oxidised. The electrochemical stability window (ESW) of the PK10 electrolyte has been evaluated as existing literature only reports thermodynamic calculations, and it must be confirmed that the electrolyte is stable in the voltage ranges the FeO gets fluorinated. After that the FeO composite was evaluated to assess its electrochemical behaviour.

4.2.1. Symmetrical PbF₂ Anode

We analysed the suitability of the Pb/PbF₂ composite as counter and reference electrode for the solid-state fluoride-ion battery cells. To do so, a series of 4 symmetric cells was fabricated as described in section 3.7. As the investigated electrochemical cell is symmetrical, a potential of zero volts should be observed during galvanostatic (dis)charging. This is because the separate redox materials are similar, and should have no electrochemical potential towards each other. The cells were prepared in such a manner that the capacity should exhibit around 1 mAh. Of the fabricated solid-state cells, cell 1 and 2 were discharged up to 2V, at a charge rate of 10 μA .

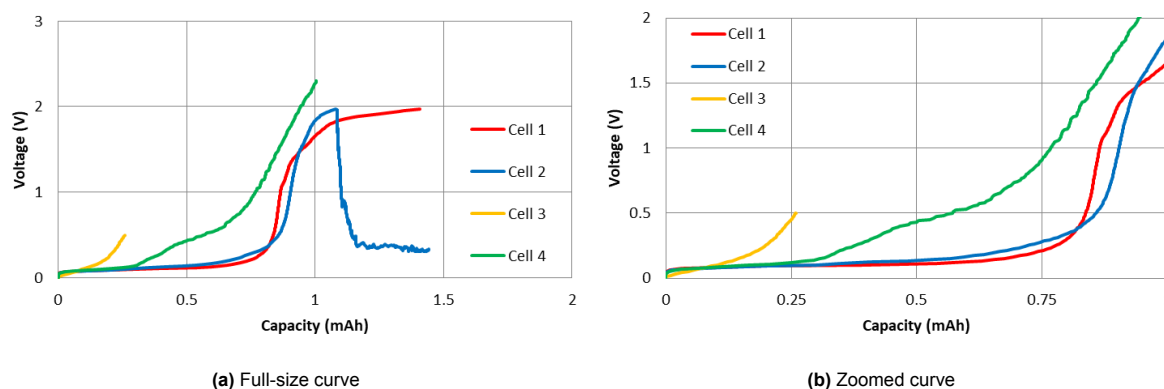


Figure 4.15: Voltage-capacity curve of the discharge of the Pb/PbF₂:PK10:Pb/PbF₂ cells

Figure 4.15 is the voltage capacity curve of cell 1 and 2, this represents the relationship between voltage levels and corresponding performance or capacity limits. As seen here, cell 1 and 2 display a plateau at 0.1V, This indicated that a redox reaction is taking place at this voltage level. It is expected to happen at such a low potential, because this is a symmetric cell, and there is not difference in the electrochemical potential between two like electrode compositions. Around the 0.8 mAh, the voltage increases for both cells to 2V, starting a second plateau, indicative for a second redox reaction. Cell 1 approaches the 2V mark, reaches this, but cell 2 suddenly drops in voltage at the 1.97V mark. This does not indicate short-circuiting, as the cell keeps discharging, but another phenomenon occurs. Despite this, the low voltage and gentle slope indicate that this composite is suitable both as counter and reference electrode.

figure 4.15 shows also cell 4. This cell was discharged, and the top and bottom electrodes were studied using XRD. This was performed to research what happens at the 2V mark. It was charged up to 2.3V to obtain information about the composition of both electrodes in a higher charge state. It exhibits less than 0.30 mAh, and does not behave like the previous two cells.

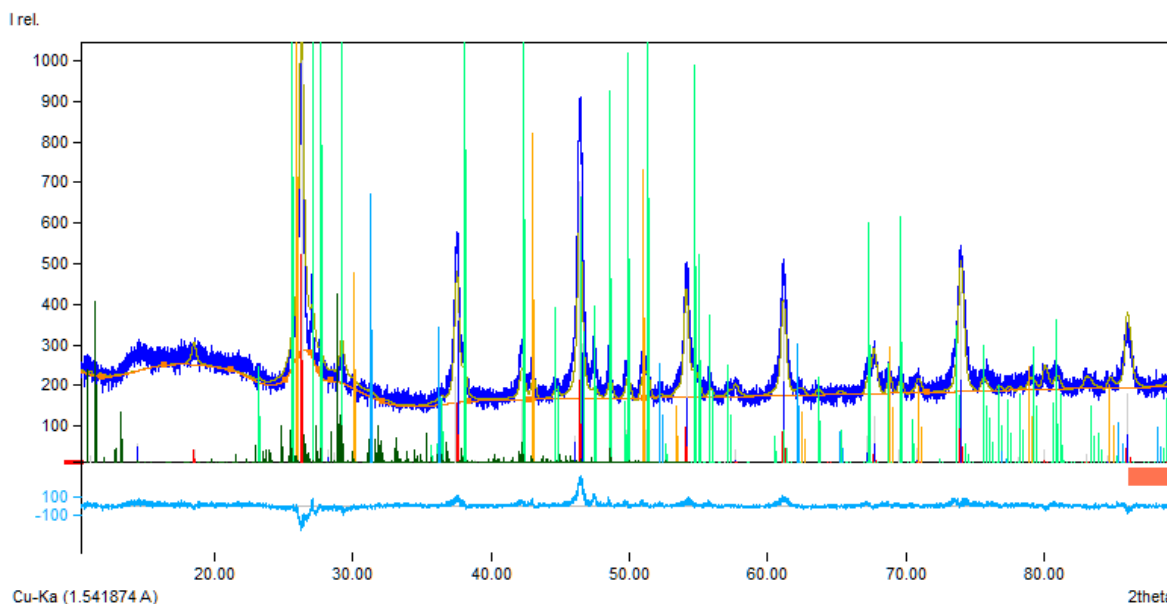


Figure 4.16: Refinement of top electrode composites of symmetric Pb/PbF₂:PK10:Pb/PbF₂ cell 4

Figure 4.16 shows the refined XRD patterns of cell 4. The composition of the different electrodes changed significantly compared to the initial composite. The composition in the top electrode changed from PK10:Pb:PbF₂ = 54:6:40, which was observed in the synthesised Pb/PbF₂ composite, to PK10:Pb:PbF₂:Cs₄Pb₉ 62:2:28:8. The new phase of Cs₄Pb₉ is predicted by Wang et al. at potentials lower than -1V [2]. As

observed, the PbF_2 content has dropped as expected, due to reduction. This formed the Cs_4Pb_9 , consuming some of the lead in the process, which explains the lower lead content despite this electrode having undergone reduction.

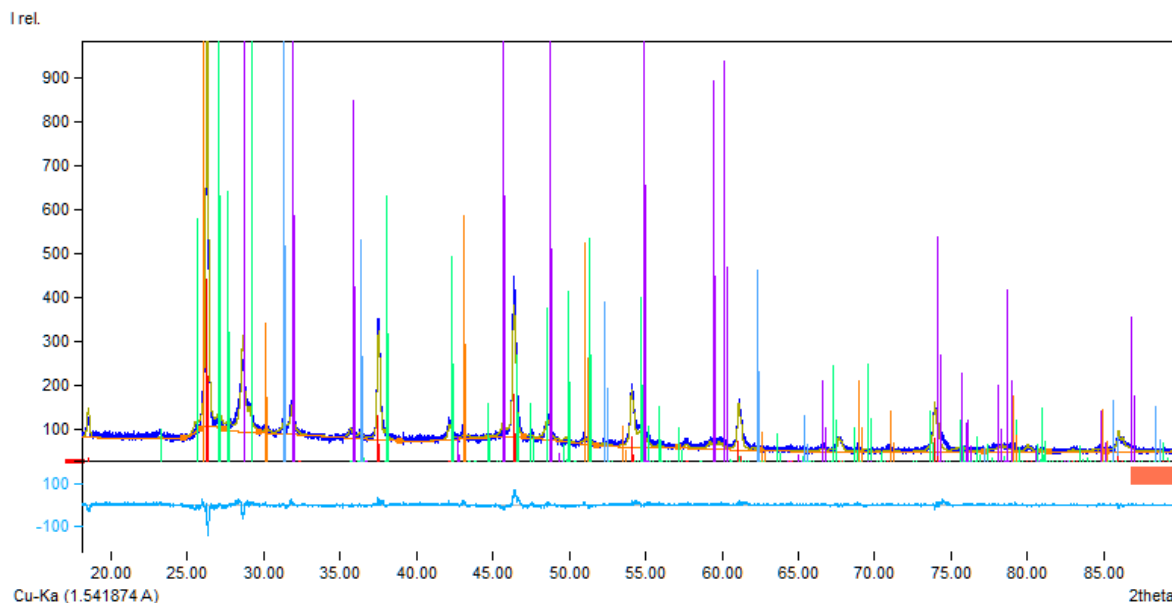


Figure 4.17: Refinement of XRD measurement of the bottom electrode composite of symmetric $\text{Pb}/\text{PbF}_2\text{:PK10:Pb}/\text{PbF}_2$ cell 4

The bottom electrode, figure 4.17, does exhibit a significant change in composition after the discharge cycle. This electrode underwent oxidation, and therefore a high amount of lead(II) fluoride was expected. However, the composition in the bottom electrode changed from $\text{PK10:Pb:PbF}_2 = 54:6:40$, to $\text{PK10:Pb:PbF}_2\text{:PbO} = 60:3:15:22$. While the lead was expected to oxidise in this electrode, formation of PbF_2 , and not PbO , is the phase that was expected. It has to be noted that figure 4.16 has a significantly higher background and broader peaks. This is because the pellet was intact when the measurement was taken, displacing it in height in the diffractometer.

Cell 3 was charged up to 0.5V, but exhibits less than 0.20 mAh capacity, significantly less than was accounted for. This is also displayed in figure 4.15. The composition of this cell was studied using XRD to further investigate the stability of PK10. At this voltage, no decomposition of the electrolyte is expected.

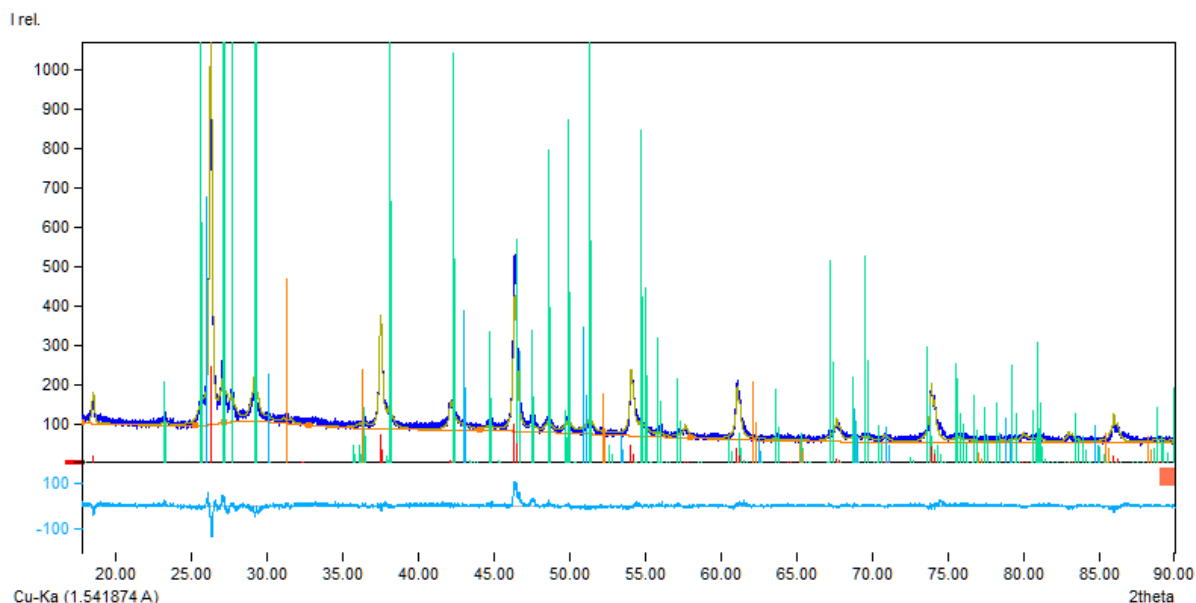


Figure 4.18: Refinement of XRD measurement of the top electrode composites of symmetric Pb/PbF₂:PK10:Pb/PbF₂ cell 3. With red bars being PK10, blue metallic lead, green orthorhombic PbF₂ and orange cubic PbF₂

In figure 4.18 the Rietveld refinement of the top electrode of cell 3 was studied. When the rough diffraction patterns are compared, no significant differences can be observed, also compared to the virgin Pb/PbF₂ composite. A composition of PK10:Pb:PbF₂ of 52:6:42 is observed.

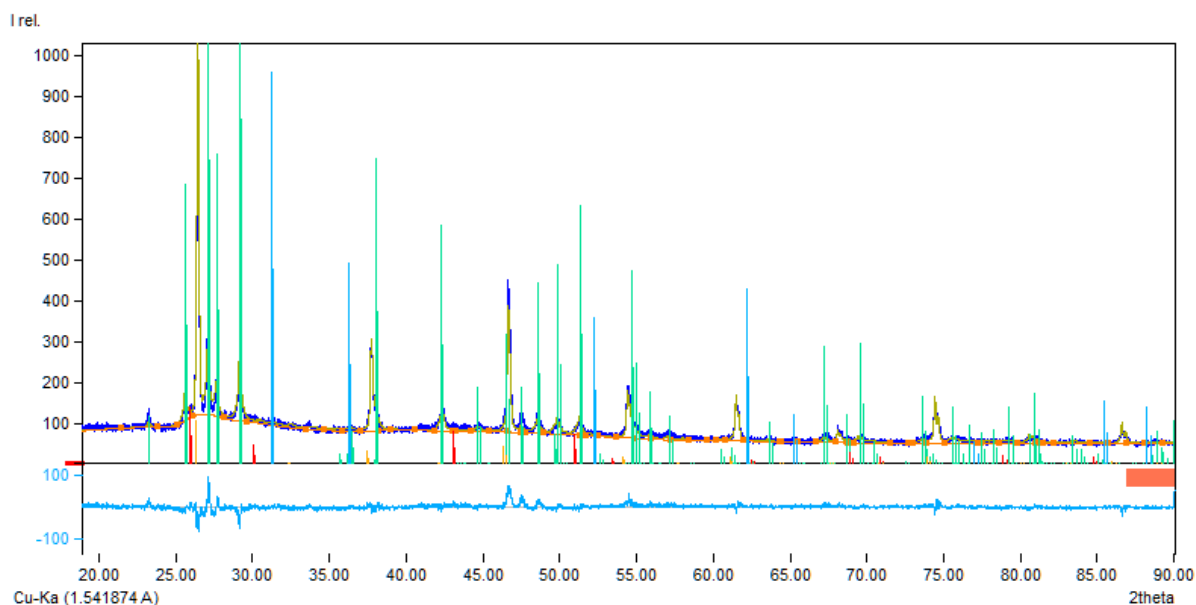


Figure 4.19: Refinement of XRD measurement of the bottom electrode composites of symmetric Pb/PbF₂:PK10:Pb/PbF₂ cell 3. With red bars being PK10, blue metallic lead, green orthorhombic PbF₂ and orange cubic PbF₂

In the bottom electrode, figure 4.19, the composition of PK10:Pb:PbF₂ is 54:5:41. Both compositions coincide with the initial anode composition of 54:6:40. From this result no apparent changes in composition upon partial discharging could be detected. This all indicates that no apparent change has occurred in this voltage range.

The discharge of cell 1 and 2 have shown expected behaviour in the galvanostat. While the capacity is not the full 1 mAh that was calculated, this lower capacity can be explained by different factors.

Surprisingly, the capacity of 0.8 mAh roughly matches the percentage of orthorhombic:cubic phases, 86.5:13.5 as established in the composite. However, as the cubic phase should be more conductive than the orthorhombic phase according to Scheiber et al., the phases do not affect the capacity in this material [67]. Apart from that, a 100% capacity is difficult to achieve with a solid-state electrolyte, as that would mean that every PbF_2 particle would have both a sufficient contact to the electrolyte, and to the carbon additives to allow both F^- and e^- conduction. As the particle size is relatively small, this negative effect should be diminished.

The plateau of 0.1 V is expected. Theoretically it should be 0V, but as explained in section 2.1, overpotentials in the cell and total circuit resistance increase this slightly. The constant and gentle slope makes this composite very suitable to be used as both counter and reference electrode.

The steep increase after this slope indicated that another redox reaction takes place at 2V. This is suspected to be the electrolyte. Which is why cell 4 was studied to investigate the composition of both electrodes after reaching this 2V mark. Interestingly one would expect an increase in the lead(II) fluoride content, or the eventual formation of higher lead fluorides due to the probable oxidation of the PK10 electrolyte. This is not the case however, and one explanation might be a leak in the cell. Causing the PbO , a litharge polymorph, to form.

A leak would cause the oxidised lead not to react with the fluoride ions, but with oxygen diffusing into the cell, especially at the electrode interface where the exposure to oxygen would be highest. The fluoride ions might have reacted with the lead deeper in the pellet, which are not visible on the XRD spectrum, as the Cu_α radiation has a typical penetration depth of a few tenths of microns. As the full cell was prepared under an argon atmosphere, this is an indication that the solid-state electrochemical cell is not fully air-tight. A recommendation to work with this specialised equipment would be to apply measures to prevent oxygen diffusion into the cell compartment.

Cell 3 shows that the cell is functional and does not show side reactions other than the intended (de)fluorination of lead in the designated voltage range. Therefore, based on the electrochemical data, the Pb/PbF_2 composite is fully suitable to be used as both counter and reference electrode to assess the electrochemical properties of FeO . The electrolyte itself is studied further in the next section.

4.2.2. PK10 Electrolyte

The ESW is the voltage range of a material where it remains electrochemically stable: it will not be reduced or oxidised, described in section 2.5. As the ESW of the PK10 solid-state electrolyte was determined using thermodynamic calculations in the work of [2], it is necessary to validate these values to ensure that the FeO and FeOF potentials vs Pb/PbF_2 are within this range. It is also needed to ensure whether the galvanostat settings, which are normally used for lithium-ion battery purposes, are properly configured. Two cells were constructed with the ECC composite as described in section 3.3. These cells were discharged up to 4V, and the voltage capacity curve can be seen in figure 4.20.

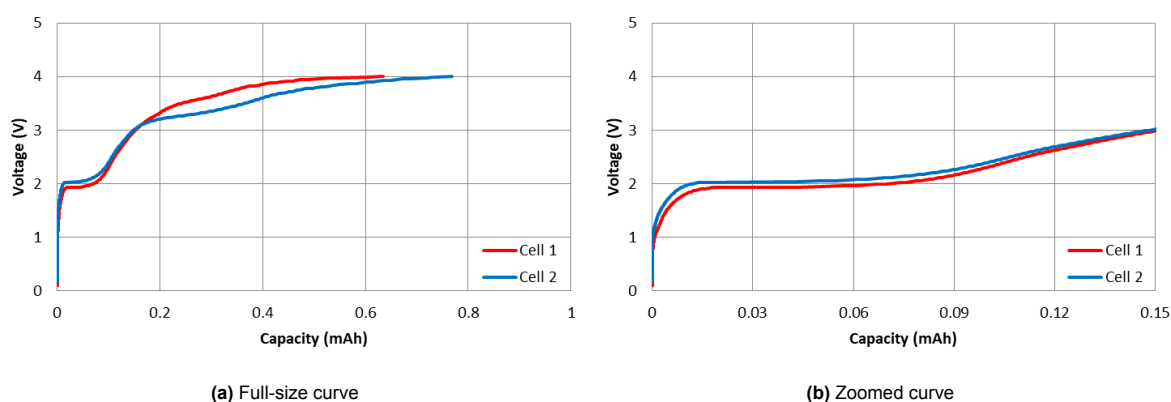


Figure 4.20: Voltage-capacity curve of the discharge of the ECC:PK10:Pb/PbF₂ cells.

Figure 4.20 displays the voltage-capacity curve for the ECC cell (assembled in duplicate). We observe a voltage plateau at 2V, with a capacity of 0.08 mAh. We also see a second plateau starting at 3.1V. This has a much higher capacity and flattens out at 4V. A slight discrepancy is observed between those two cells, where cell 1 reaches the 4V level earlier compared to cell 2. As all cells fabricated in this project, the calculated capacity is around 1 mAh, for both the cathode and anode composite. Therefore a capacity of 0.08 mAh is very low.

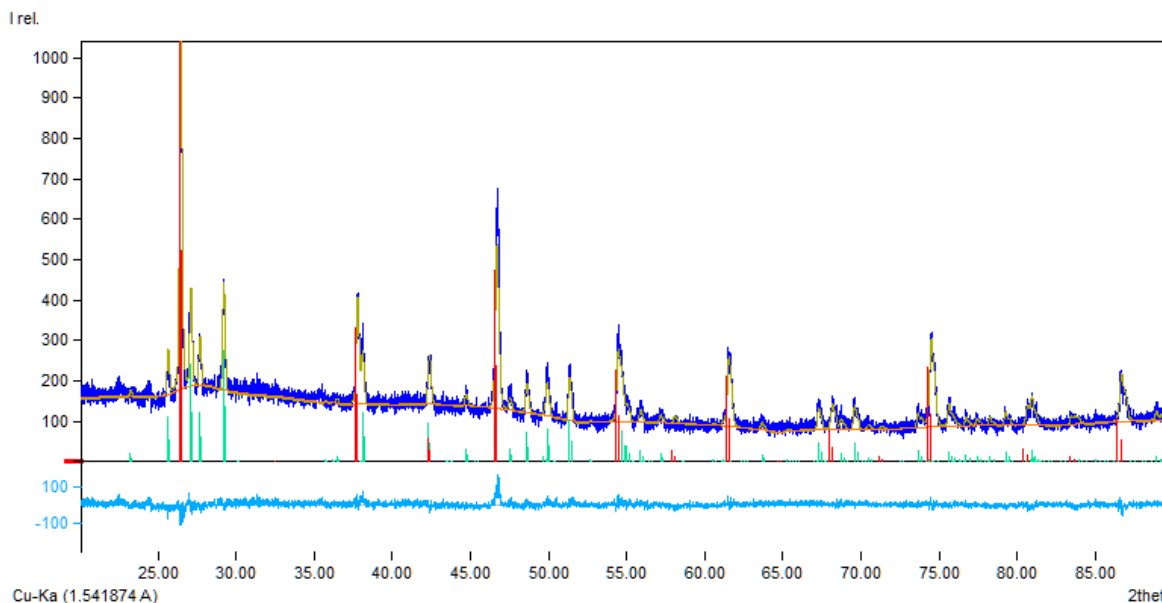


Figure 4.21: Refinement of XRD measurement of the bottom electrode (Pb/PbF₂) of the ECC:PK10:Pb/PbF₂ cells (combined spectrum). CsPbF₃ in red, PbF₂ in green.

Figure 4.21 shows the bottom Pb/PbF₂ electrode that has been measured using XRD. No reflexes are observed at $2\theta = 31.3^\circ$ and $2\theta = 36.3^\circ$. This indicates that no lead is present in this sample, as stated in section 4.1.1. Only CsPbF₃ (red, 66%) and orthorhombic PbF₂ (green, 34%) have been found. This indicates two things: first, the lead metal in the the composite has been fully fluorinated, and therefore oxidised. Secondly, as CsPbF₃ is observed, and not PK10, this could be the result of reduced PK10. While the difference is difficult to discern, refinement of the Biso parameters and lead vacancies indicate that this indeed concerns CsPbF₃. This is not conclusive evidence however.

From the obtained galvanostat, XRD and impedance results several phenomena can be observed. The voltage-capacity curves neatly indicate a plateau at 2V, which indicated the oxidation of the electrolyte. This is in the expected range of 1.7V vs. Pb/PbF₂ from the thermodynamic calculations as described by Wang et al. [2]. The low capacity of this plateau can be attributed to a certain degree of degradation, where the fluoride-ion conduction is insufficient to maintain the reaction, increasing the overpotential, leading to fluorination of other components in the cell. The second plateau starts at 3.1V vs. Pb/PbF₂. This is possibly related to the fluorination of the carbon additives, $C + F^- \longrightarrow CF + e^-$ as described by Nowroozi et al. [32]. As the carbon additives in this sample account for 22 mAh, further charging of this cell probably would have led to further fluorination of the carbon in the sample. This is not detectable in the XRD pattern for two reasons. First, the CF is in this sample present in such low concentrations that this would not be detectable, and second, the CF is probably amorphous, similar to the carbon nanotubes themselves.

The XRD pattern indicated presence of PbF₂ and CsPbF₃. PbF₂ is present, which is the result of reduction of the PK10 electrolyte in the top electrode, as this would be the only source of fluoride-ions in the cell. It is also worth to mention that the lead(II) fluoride that formed during fluorination of the lead metal, exists solely as orthorhombic PbF₂, as no cubic PbF₂ could be found in the pattern. The CsPbF₃ present in the measurement can be indicative of oxidation of the electrolyte in this electrode. Due to the small differences, no definite conclusion can be drawn from this. No other phases could be

detected in the pattern, no metallic lead and not even PbF_3 or PbF_4 , which are other phases that could form upon fluorination at higher voltages.

When looking at the impedance measurements as well, appendix A, after galvanostatic discharging, the cell exhibits a significantly lower electronic conductivity. This is most likely due to the reaction of the PK10 electrolyte, which naturally lowers the ionic conductivity. Degradation of the carbon as speculated earlier, would also decrease the electronic conductivity in the cell. The bigger semicircle of cell one would agree with this, as this is related to mass/charge transfer resistance, which is higher in a system where this conductivity is lower due to degraded electrolyte.

The PK10 electrolyte seems to be suitable for use as electrolyte in solid-state electrochemical cells at a voltage below 2V vs. Pb/PbF_2 . This is because the electrolyte shows no signs of degradation before reaching this point. This is in line with the thermodynamic calculations stated in literature. No side-reactions with the lead have been established either. With low certainty, the main product that might have been observed is CsPbF_3 . This verifies also that the galvanostat has the correct configuration for the different electrochemistry of the FIBs. Whether the plateau observed starting at 3.1V originates from further degradation of the PK10 electrolyte leading to further fluorination of the lead at higher voltages due to overpotentials, or fluorination of the carbon has not been determined with high certainty. However, as the cell is not supposed to operate at these higher voltages, this is less relevant to evaluate the electrochemical properties of FeO and FeOF .

4.2.3. FeO Cathode

As a proper solid-state electrolyte, PK10, and a suitable counter/reference electrode has been established, Pb/PbF_2 , the electrochemical properties of ferrous oxide is evaluated. The cells are fabricated as stated in section 3.7. This was done by constructing a cell using the FeO composite as top-electrode, and charging this at $10\mu\text{A}$ in the galvanostat. The FeO electrode was subsequently studied in XRD.

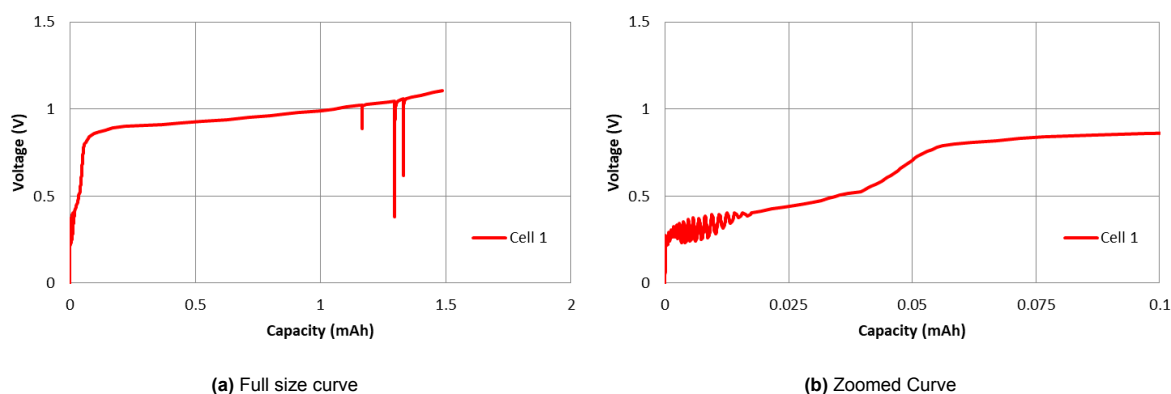


Figure 4.22: Voltage-capacity curve of FeO 1 cell charged to 1.1V

Figure 4.22 shows the voltage-capacity of the FeO cell. We observe two plateaus. The first starts at 0.28V and increases up to 0.53V. This is in range of the expected 0.27V that was found using thermodynamic calculations stated in section 3.4. This plateau has a capacity of just 0.04 mAh, which equates to 4% of the expected capacity. The plateau also shows some artefacts, which destabilise the measurement, but do not directly affect the accuracy nor functioning of the cell. A second plateau is observed at the 0.8V. This has a much higher capacity, but this is not related to the reaction under investigation.

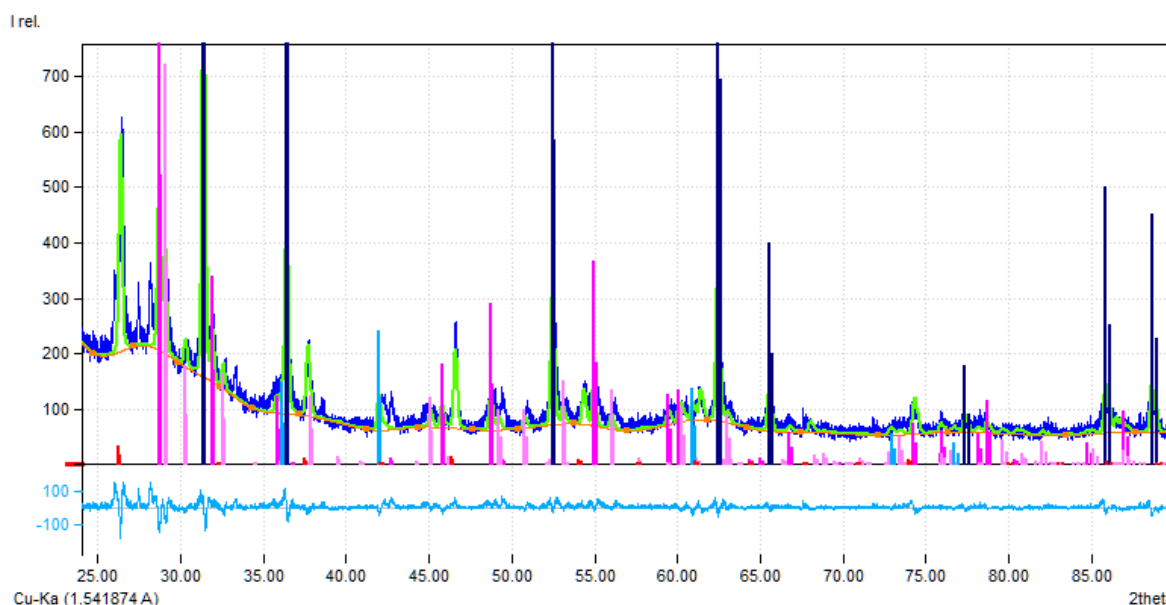


Figure 4.23: Refinement of XRD measurement of the top FeO electrode of the FeO:PK10:Pb/PbF₂ cell. Red indicated PK10, blue Fe_{0.944}, black metallic lead, and purple and pink respectively litharge and massicot.

Figure 4.23 displays the XRD measurement taken of the FeO electrode after galvanostatic charging the cell. A large amount of reflexes is observed. Peaks of the PK10 electrolyte are found at the expected diffraction angles, which are mentioned in section 4.1.2. Peaks of an iron deficient ferrous oxide are also found at $2\theta = 36.18^\circ$, $2\theta = 42.03^\circ$ and $2\theta = 61.00^\circ$. Both of these were part of the initial composite, which is expected. Despite that, strong peaks at $2\theta = 31.62^\circ$, $2\theta = 36.51^\circ$ and $2\theta = 52.52^\circ$ seem to indicate the presence of metallic lead (COD entry: 96-101-1120) in the sample. As well as both polymorphs of the lead oxides massicot and litharge, mentioned in section 4.1.1. The presence of these metals is unexpected as these are more expected in the Pb/PbF₂ composite. According to the Rietveld refinement, PK10 makes up 20% of the composition, 15% Fe_{0.944}, 40% metallic lead and 15% PbO. These high percentages of lead-based materials is not in line with the initial composition. There are also several non-indexed reflexes in the pattern at $2\theta = 27.41^\circ$, $2\theta = 28.23^\circ$, $2\theta = 33.31^\circ$, $2\theta = 38.72^\circ$, $2\theta = 42.70^\circ$ and more. These reflexes do not match any suitable compound based on Fe,Cs,K,Pb,O,F in the COD.

The electrochemical properties of FeO in a composite with carbon nanofibers and PK10 electrolyte were investigated. Figure 4.22 shows two plateaus, of which the first is in agreement with the thermodynamically calculated voltage of 0.27V vs. Pb/PbF₂. Therefore this is highly likely that this first plateau belongs to the fluorination of the iron oxide. However, the capacity of said reaction is 0.04 mAh, 4% of the calculated capacity. The second plateau is much larger, but at 0.8V. This is significantly above the calculated potential, and has a capacity almost 1.5x the calculated capacity for the conversion of FeO to FeOF. Despite that, there is no other materials that could have reacted. The PK10 is stable up to 2V vs. Pb/PbF₂, and the experiment in section 4.1.2 demonstrated that also the carbon is stable in this range. Therefore, another reaction is happening with higher capacity than the expected FeO. While, thermodynamic calculations of PbF₂ vs PbF₄ indicate a potential difference of 0.82V, lead(II) fluoride should not be present in the top electrode.

Refinement of the top electrode however, surprisingly did indicate the presence of metallic lead and lead oxides in significant amounts. No PbF₄ is found. The composition is highly unexpected due to several reasons. This concerns the top electrode containing the FeO composite, consisting of 60% PK10 and 30% FeO (with some iron-based side-phases). Therefore, this leads to two options. Either the PK10 electrolyte has reacted in a certain manner, or this concerns by accident the bottom, lead-based electrode. Considering the fact the PK10 should be stable in this voltage range, it is unlikely that this has reacted. However, the presence of both ferrous oxide and lead rules out the possibility of this being the bottom electrode. The presence of both lead(II) oxides in the electrode, indicates that

the cell was not airtight. This might lead to an unpredicted side-reaction, that yields the plateau in the voltage-capacity curve.

From the voltage-capacity curve we can conclude that the FeO is not able to be sufficiently fluorinated. While the observed voltage plateau at 0.27V vs. Pb/PbF₂ is in agreement with the thermodynamic calculations, the capacity is lacking. While a smaller particle size might be beneficial, the low capacity indicates that the material likely becomes passivated upon fluorination. This further prevents fluorination of the active material particles. Therefore this is not suitable for electrochemical fluorination.

4.3. Iron Oxyfluoride

4.3.1. FeOF Cathode Synthesis

Ferrous oxide, FeO, has been tried as cathode material, and electrochemical fluorination has been attempted. Therefore iron oxyfluoride, FeOF, needs to be evaluated as well. The purpose of this is to assess whether electrochemical defluorination of this material is possible, as both reactions are needed for a functioning battery cell.

While ferrous oxide can be obtained from suppliers such as Merck and Thermo Fisher in relatively high purity, this is not true for iron oxyfluoride. Zhai et al. describes a method to actually synthesise this material as described in section 4.3.1. After conducting the synthesis, the substrate had the same ochre colour as described, and was also studied using X-ray diffraction.

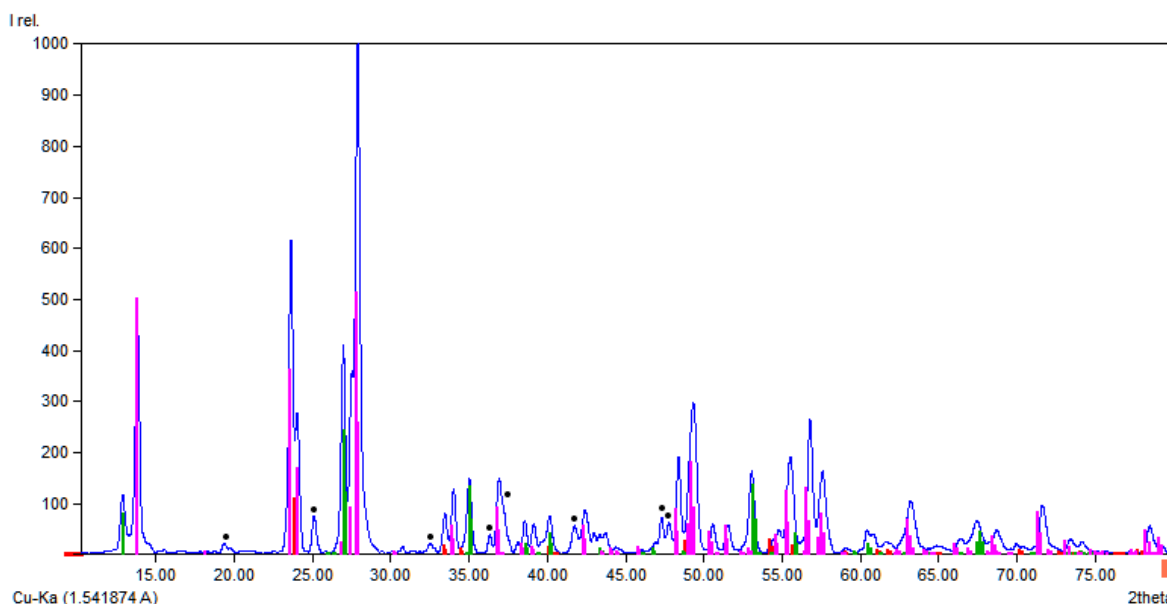


Figure 4.24: Indexed XRD pattern of the FeOF synthesis. Red bars indicate unreacted FeF₃, green bars indicate FeOF and pink indicates FeO_{0.55}F_{2.667}

Figure 4.24 displays the XRD pattern of the synthesised FeOF. This synthesis succeeded partially as the green peaks indicate FeOF, which according to a Rietveld refinement, make up 20% of the composition. There is also 2% unreacted FeF₃ present in the composition. But more interesting is the 57% hexagonal FeO_{0.55}F_{2.667}. While this has not fully reacted to FeOF, it is at least partially formed. This could have electrochemical activity. The unidentified reflexes are indicated in figure 4.24 by black circles, but based on the precursors they should be composed of other partially oxygenated iron(III) fluorides that have not been included in the XRD database, with a formula of FeO_xF_{3-3x}.

Two other synthesis methods were tried using the faster method of Zhu et al. as described in section 3.6. This differs in the fact that a mixture of pentanol and methanol is used instead of 1-propanol, as well as a shorter solvothermal reaction time. Both FeF₃ and FeF₃ · 3 H₂O were investigated, and both syntheses did not succeed.

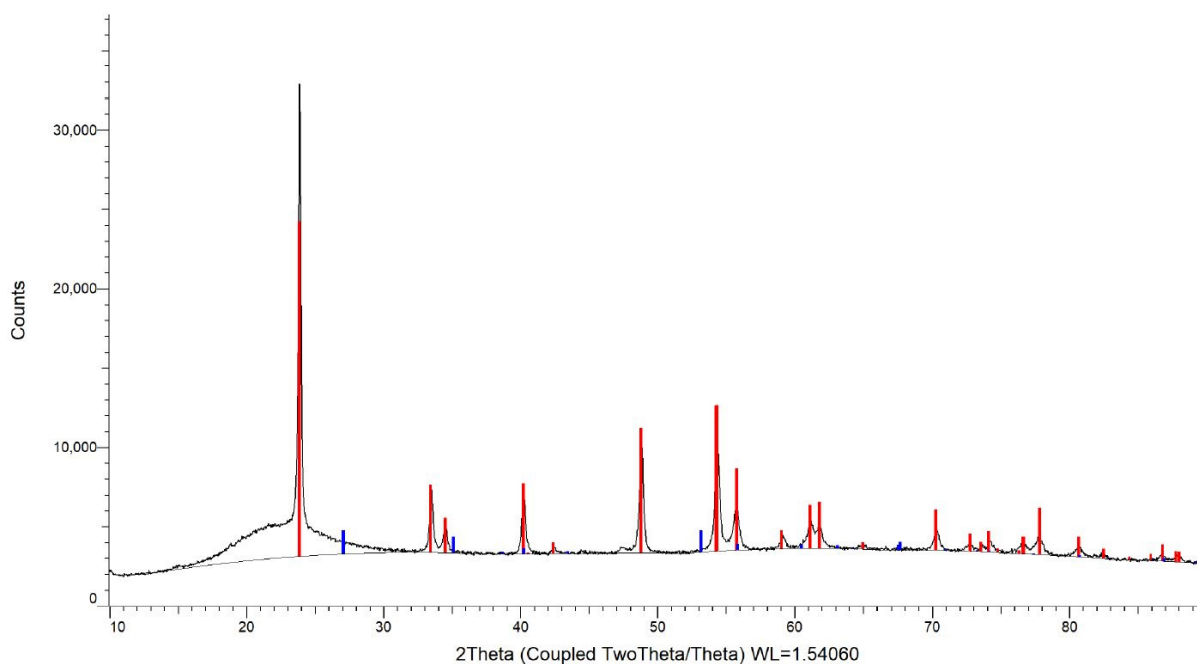


Figure 4.25: XRD measurement of the FeOF synthesis according to Zhu et al. using FeF₃. Red bars indicate reflexes of FeF₃, blue bars indicate where the FeOF reflexes should have been

Figure 4.25 displays the XRD measurement of the FeOF synthesis according to Zhu et al. using dehydrated FeF₃. It became evident that the sample did not contain any FeOF, and the dehydrated FeF₃ had not reacted with the methanol and 1-pentanol mixture. The red lines in the figure indicate reflexes of FeF₃, and the blue lines indicate the FeOF reflexes if they had been present. It is notable that there is a bump present around $2\theta = 20^\circ$.

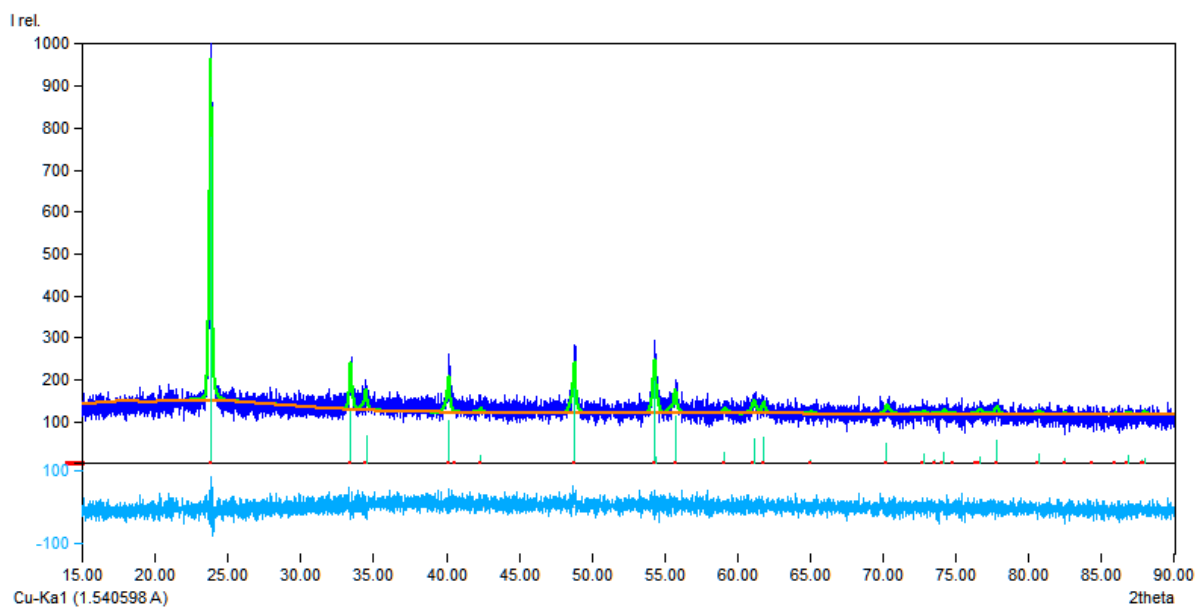


Figure 4.26: Refinement of XRD measurement of the FeOF synthesis according to Zhu et al. using FeF₃ · 3H₂O. All reflexes belong to FeF₃

Figure 4.26 displays the XRD measurement and subsequent refinement of hydrated FeF₃. The reflexes at $2\theta = 23.87^\circ$, $2\theta = 54.47^\circ$ and $2\theta = 48.82^\circ$ and others in decreasing intensity indicate FeF₃ (COD entry: 96-100-0477). Analysis indicates this is at least 95% purity. After synthesis, it was noticeable

that part of the $\text{FeF}_3 \cdot 3\text{H}_2\text{O}$ had not reacted at all. Absence of a ochre-coloured shell on some particles was a visual indication that this synthesis did not have the desired outcome. This is reinforced by X-ray diffraction and subsequent refinement of the pattern as described above.

Three attempts were made to synthesise this material. Two attempts using the synthesis method of Zhai et al., using methanol and 1-pentanol as co-solvent, described in section 4.3.1, and one attempt was by Zhu et al. The latter was partially successful, and yielded a composition with 2% FeF_3 , 20% FeOF , 57% $\text{FeO}_{0.55}\text{F}_{2.67}$ and 21% other iron(oxy)fluorides. Based on this, a capacity estimation was determined to be 400 mAh/g, based on the calculated gravimetric capacities of the individual components, assuming that both the FeOF and the $\text{FeO}_{0.55}\text{F}_{2.67}$ will react. The unidentified 21%, assumed to have a formula of $\text{FeO}_x\text{F}_{3-3x}$ are known to exist according to literature [68], as they have been synthesised using roll-quenching methods.

In the synthesis using the method by Zhu et al. and using dehydrated FeF_3 , there is a significant bump observed in the XRD pattern. The range and shape seem to be aligning with amorphous silica, figure 4.27, similar to the result of Maddalena et al. [69]. The origin of this is most probably residual SiO_2 that has been taken off by removing the presumed FeOF from the silicate glass of a Büchner funnel.

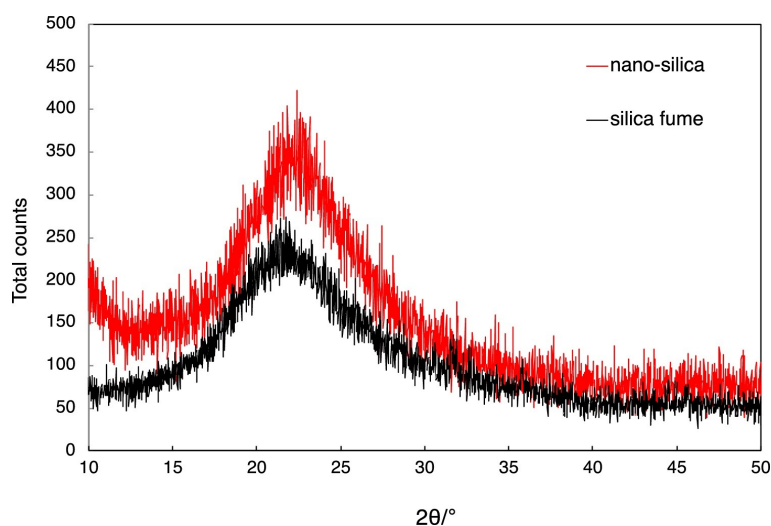


Figure 4.27: X-ray diffraction pattern characteristic for silica, SiO_2 . Reproduced from [69].

Using Zhu's method, it is not evident why this synthesis did not succeed. Two different types of iron(III) fluoride were tried, one hydrated, one dehydrated. It was observed that during the second synthesis, the iron salt did only dissolve slowly into the methanol, this might indicate solubility limits. Some sources state that the iron salt is ball-milled for half an hour to reduce particle size, and stirred for half an hour in 1-propanal to ensure the material was fully dissociated in Fe_3^+ and F^- ions [70]. The ball-milling and the longer stirring time might be tried in subsequent synthesis attempts to ensure that this is not the root of the issue.

In general, we can say that the method as described by Zhai et al. is successful in at least partially synthesising the FeOF , which is why this product has been used for assessing the defluorination performance of this material. While the method described by Zhu et al. is unsuccessful, this might be caused by insufficient preparation of the material, or faulty equipment, or a lapse in carrying out the proper procedure.

4.3.2. FeOF Electrochemical Performance

One FeOF synthesis partially succeeded and we can evaluate the electrochemical properties of this material. This was done by constructing the cell as described in section 3.7. The FeOF composite is the top-electrode and the cell was discharged at 10 μA in the galvanostat.

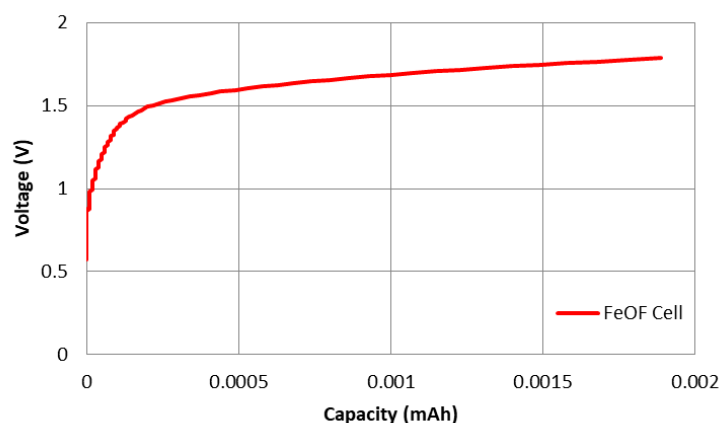


Figure 4.28: Voltage-capacity curve of FeOF, cut off at 1.8V and capacity of 0.0019 mAh

Figure 4.28 displays the voltage capacity curve of the FeOF cell. No plateau is observed around 0.27V vs. Pb/PbF₂. The only plateau is starting around 1.5V vs. Pb/PbF₂. This plateau has a capacity of 0.0019 mAh, which is almost 0.2% of the expected capacity. While voltage should still be inside the stability range according to earlier observations, it is on the higher end of this. The cut-off voltage of 1.8V vs. Pb/PbF₂ is reached quickly. This means that there is almost no reaction happening in the lower voltage range.

1.8V vs. Pb/PbF₂ is indicative of electrolyte decomposition. While it is just starting, the cell has probably not been damaged yet. We would expect a defluorination of the expected FeO_xF_{3-3x}. This would be expected below 1V vs. Pb/PbF₂, and no plateau is observed there. Therefore we can conclude from this measurement that the electrode composite of FeO_{0.55}F_{2.67} and FeOF is not able to be defluorinated. Due to this result, the cell was reversed. As the Pb/PbF₂ composite is used as bottom electrode, and the cell only reached 0.2% capacity, the cell was charged further to observe what might happen.

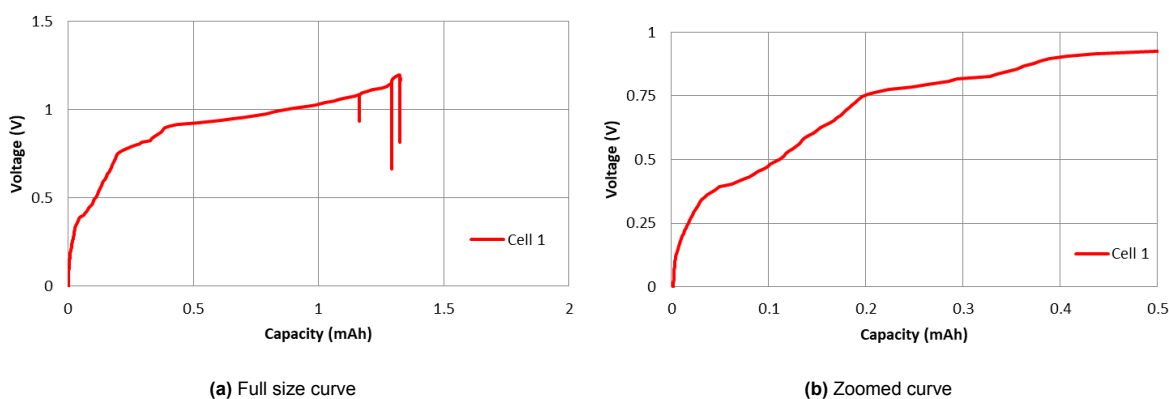


Figure 4.29: Voltage-capacity curve of reversed FeOF cell, cut off at 1.2V and capacity of 0.0019 mAh

Figure 4.29 displays the charge curve of the FeOF cell. It was charged up to 1.2V vs. Pb/PbF₂, and shows 3 plateaus. It concerns a plateau from 0.40V to 0.48V vs. Pb/PbF₂, from 0.75V to 0.82V vs. Pb/PbF₂ and a plateau starting at 0.89V vs. Pb/PbF₂. Where the first one has a capacity of 0.06 mAh, 0.12 mAh for the second one, and at least and more than 1 mAh capacity for the third.

The first plateau agrees with the observations in the FeO cell, and is probably coming from further fluorination of the FeO, or partially fluorinated FeO in the sample. The third plateau is of the same origin as speculated for FeO, as the cell is not airtight, this would lead to a similar lead-based side reaction. The second plateau is of unknown origin. This comparison is even more clear in figure 4.30 below, that displays the voltage capacity curve of both FeO, and the reversed FeOF cell.

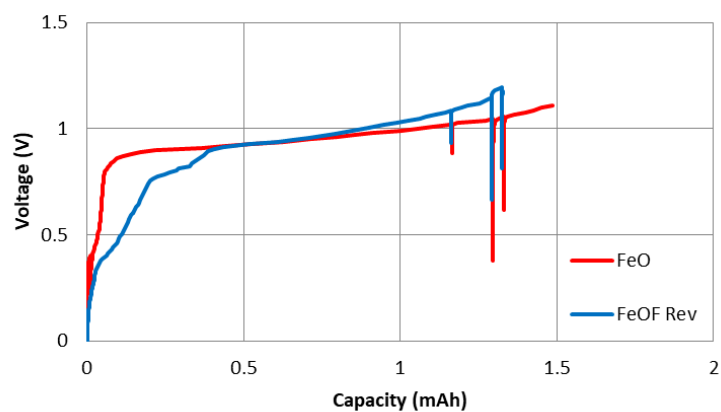


Figure 4.30: Voltage-capacity curve of FeOF, cut off at 1.8V and capacity of 0.0019 mAh

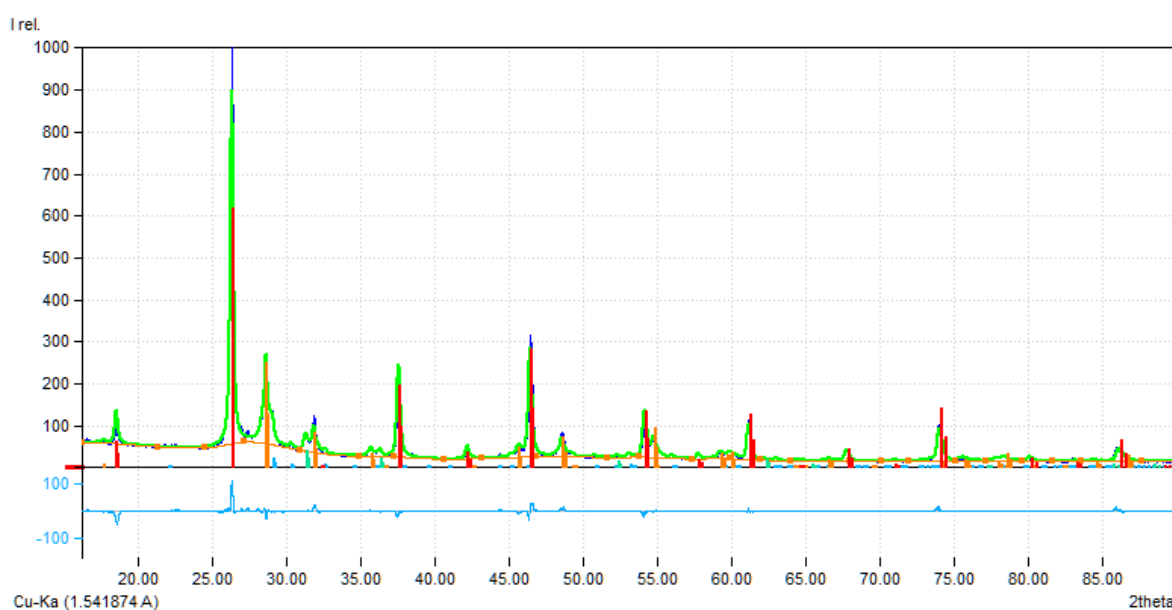


Figure 4.31: Refinement of XRD measurement of top-electrode of FeOF cell. Red bars indicate the PK10 electrolyte, orange and blue PbO and green is metallic lead

Figure 4.31 displays the refinement of the XRD measurement of the top electrode of the FeOF cell. Indexing of the reflexes indicate the presence of PK10 electrolyte, metallic lead, and both polymorphs of the lead oxide. While the percentage of PK10 electrolyte, 66.8%, matches, a significant amount of metallic lead and lead oxides is observed, 18.6% tetragonal litharge, 5% orthorhombic massicot and 4% metallic lead.

The presence of the lead(II) oxide indicate that also this cell is not airtight. It can also indicate that a similar reaction has taken place at the third voltage plateau, probably a conversion to lead(II) oxide. It is surprising to see that no iron was visible in the XRD pattern, as well as this significant amount of lead-based phases. Despite this result, the voltage-capacity curve indicates that the FeOF could not be defluorinated sufficiently. This conclusion is drawn from the lack of capacity at the desired voltage range.

5.1. Conclusion

The intermittent nature of renewable energy systems poses a problem for grid stability to ensure an adequate supply of electricity. To solve this, electrochemical energy storage might provide a solution, especially in the form of batteries. Currently, lithium-based batteries are the most widespread commercial option for this storage, but this material suffers from scarcity, which is why alternatives must be sought. A suitable replacement can be the fluoride-ion battery (FIB) due to the abundance of fluorine in the form of fluorite. This FIB still needs to be explored, especially in the sense of fluoride-conducting electrolyte materials, but even more in the sense of suitable electrode materials.

Due to the abundance of iron in the Earth's crust, and the positive results of this material booked in the lithium-ion battery sector, an iron-based electrode material is very interesting. Despite earlier work in the use of conversion-based iron fluorides and intercalation-based Ruddlesden-Popper phases, both materials were either lacking in stability or energy density. Therefore oxyfluorides were explored, as in these structures the oxygen anions provide a scaffolding function, reducing the expansion and contraction of the material upon fluorination and defluorination.

The main goal of this research was to evaluate the eligibility of FeOF as cathode material for fluoride-ion batteries. To find the answer to this question, FeO was made into an electrode composite, which was incorporated in a solid-state electrochemical cell which was galvanostatically charged to understand its behaviour. The electrode composites were studied using SEM and X-ray diffraction to investigate the properties of the materials before and after the (dis)charging of the cell. To be suitable, the material must be able to be fluorinated and defluorinated for a significant part of its theoretical capacity. To investigate whether this is feasible, various research questions were investigated.

A suitable testing environment was established for the assessment of this material. Using a composite of lead/lead(II) fluoride as both counter- and reference electrode, as well as the $\text{CsPb}_{1-x}\text{K}_x\text{F}_{3-x}$ electrolyte, the FeO composite was tested. It was found that there was activity in the expected voltage range, most likely originating from the fluorination of FeO. It was found that a capacity of almost 0.0019 mAh was reached, which corresponds to 0.2% of the theoretical capacity.

To evaluate the defluorination of iron oxyfluoride, this material first needed to be synthesised. Two methods were assessed, and only one of these was just partially successful. Further research is needed to find a more suitable chemical synthesis method. The partially synthesised FeOF underwent an attempt of defluorination. This is considered impossible as it showed no signs of electrochemical reactivity in the voltage range of 0V - 1.8V vs. Pb/PbF₂, while the defluorination is expected at 0.27V vs. Pb/PbF₂.

All in all, due to the low capacity of FeO upon fluorination, and the inability of the FeOF to become defluorinated, we can conclude that this pioneering work in the suitability of iron oxyfluoride as cathode for fluoride-ion batteries comes out negative. Iron oxyfluoride is not a suitable material for this purpose.

5.2. Recommendations

While it is found that FeO and FeOF are not suitable as electrode materials, a wide array of other materials might be. This work evaluated the suitability of an ambivalent Pb/PbF₂ electrode composite that can function both as a reference electrode and as a counter electrode. The electrochemical stability window of the PK10 electrolyte was also determined against the Pb/PbF₂ electrode. This combined with the finding that the air-tight cells are not as impermeable as initially thought, builds a strong foundation for future research. By using a similar setup, several different electrode materials might be evaluated and a systematic approach with a theoretical or computational basis can quickly assess a broad range of possible electrode materials.

Further recommendations and modifications would be the possibility of in-situ XRD. By using this technology, information might be obtained concerning the actual phase changes in the active material upon reaction and provide insight into the processes happening inside the electrochemical cell. Concerning other equipment, maintaining an argon atmosphere inside of the cell is critical to prevent unfavourable side reactions. Therefore in future research, it is recommendable to make modifications to the cell to ensure the impermeability of the cell structure.

References

- [1] Harshita Bhatia et al. "Conductivity Optimization of Tysonite-type $\text{La}_{1-x}\text{Ba}_x\text{F}_3$ -x Solid Electrolytes for Advanced Fluoride Ion Battery". In: *ACS Applied Materials & Interfaces* 9.28 (July 2017), pp. 23707–23715. DOI: 10.1021/acsami.7b04936. URL: <https://doi.org/10.1021/acsami.7b04936>.
- [2] Jinzhu Wang et al. "A Fluoride-Ion-Conducting Solid Electrolyte with Both High Conductivity and Excellent Electrochemical Stability". In: *Small* 18.5 (Nov. 2021), p. 2104508. DOI: 10.1002/smll.202104508. URL: <https://doi.org/10.1002/smll.202104508>.
- [3] Yanchang Wang et al. "Oxyfluoride Cathode for All-Solid-State Fluoride-Ion Batteries with Small Volume Change Using Three-Dimensional Diffusion Paths". In: *Chemistry of Materials* 34.23 (2022), pp. 10631–10638.
- [4] Jiali Liu et al. "Constructing a $\text{BiF}_3/\text{Bi}_7\text{F}_{11}\text{O}_5$ multiple-phase composite as advanced cathode for room-temperature all-solid-state fluoride-ion batteries". In: *Journal of Electroanalytical Chemistry* 928 (2023), p. 117073.
- [5] Datong Zhang et al. "Reversible and Fast (De) fluorination of High-Capacity Cu_2O Cathode: One Step Toward Practically Applicable All-Solid-State Fluoride-Ion Battery". In: *Advanced Energy Materials* 11.45 (2021), p. 2102285.
- [6] Martin Winter and Ralph J. Brodd. "What Are Batteries, Fuel Cells, and Supercapacitors?" In: *Chemical Reviews* 104.10 (2004). PMID: 15669155, pp. 4245–4270. DOI: 10.1021/cr020730k. URL: <https://doi.org/10.1021/cr020730k>.
- [7] Paul Meister et al. "Best Practice: Performance and Cost Evaluation of Lithium Ion Battery Active Materials with Special Emphasis on Energy Efficiency". In: *Chemistry of Materials* 28.20 (2016), pp. 7203–7217. DOI: 10.1021/acs.chemmater.6b02895. URL: <https://doi.org/10.1021/acs.chemmater.6b02895>.
- [8] S. Koochi-Fayegh and M.A. Rosen. "A review of energy storage types, applications and recent developments". In: *Journal of Energy Storage* 27 (2020), p. 101047. ISSN: 2352-152X. DOI: <https://doi.org/10.1016/j.est.2019.101047>. URL: <https://www.sciencedirect.com/science/article/pii/S2352152X19306012>.
- [9] Storm William D Gourley, Tyler Or, and Zhongwei Chen. "Breaking free from cobalt reliance in lithium-ion batteries". In: *Iscience* 23.9 (2020), p. 101505.
- [10] Jason R Croy, Brandon R Long, and Mahalingam Balasubramanian. "A path toward cobalt-free lithium-ion cathodes". In: *Journal of Power Sources* 440 (2019), p. 227113.
- [11] Wangda Li, Steven Lee, and Arumugam Manthiram. "High-nickel NMA: a cobalt-free alternative to NMC and NCA cathodes for lithium-ion batteries". In: *Advanced materials* 32.33 (2020), p. 2002718.
- [12] Xue-Ping Gao and Han-Xi Yang. "Multi-electron reaction materials for high energy density batteries". In: *Energy & Environmental Science* 3.2 (2010), pp. 174–189.
- [13] Qi Liu et al. "Rechargeable anion-shuttle batteries for low-cost energy storage". In: *Chem* 7.8 (2021), pp. 1993–2021.
- [14] Dechao Wang et al. "LaF₃-BaF₂-KF derived electrolyte in solid state fluoride-ion battery". In: *MRS Online Proceedings Library (OPL)* 1266 (2010).
- [15] M Anji Reddy and Max Fichtner. "Batteries based on fluoride shuttle". In: *Journal of Materials Chemistry* 21.43 (2011), pp. 17059–17062.
- [16] Xiangyu Zhao et al. "Chloride ion battery: a new member in the rechargeable battery family". In: *Journal of Power Sources* 245 (2014), pp. 706–711.

- [17] Hang Li et al. "A novel type of chloride ion battery that can change the structure of electric vehicle". In: *Journal of Power Sources* 512 (2021), p. 230507.
- [18] Ryo Sakamoto et al. "All-Solid-State Chloride-Ion Battery with Inorganic Solid Electrolyte". In: *ChemElectroChem* 8.23 (2021), pp. 4441–4444.
- [19] Hang Li et al. "A novel rechargeable bromine-ion battery and the induction of bromine ions on metal electrodes". In: *Sustainable Energy & Fuels* 4.8 (2020), pp. 3871–3878.
- [20] Sumol V Gopinadh et al. "Fluoride-ion batteries: State-of-the-art and future perspectives". In: *Sustainable Materials and Technologies* (2022), e00436.
- [21] Jinzhu Wang et al. "A Fluoride-Ion-Conducting Solid Electrolyte with Both High Conductivity and Excellent Electrochemical Stability". In: *Small* 18.5 (Nov. 2021), p. 2104508. DOI: 10.1002/smll.202104508. URL: <https://doi.org/10.1002/smll.202104508>.
- [22] Michael D Slater et al. "Sodium-ion batteries". In: *Advanced Functional Materials* 23.8 (2013), pp. 947–958.
- [23] Ya-Tao Liu et al. "Strategy of enhancing the volumetric energy density for lithium–sulfur batteries". In: *Advanced Materials* 33.8 (2021), p. 2003955.
- [24] Chengcheng Fang, Xuefeng Wang, and Ying Shirley Meng. "Key issues hindering a practical lithium-metal anode". In: *Trends in Chemistry* 1.2 (2019), pp. 152–158.
- [25] Yanguang Li and Jun Lu. "Metal–air batteries: will they be the future electrochemical energy storage device of choice?" In: *ACS Energy Letters* 2.6 (2017), pp. 1370–1377.
- [26] M. Anji Reddy and M. Fichtner. "Batteries based on fluoride shuttle". In: *J. Mater. Chem.* 21 (43 2011), pp. 17059–17062. DOI: 10.1039/C1JM13535J. URL: <http://dx.doi.org/10.1039/C1JM13535J>.
- [27] Albert W. Xiao, Giulia Galatolo, and Mauro Pasta. "The case for fluoride-ion batteries". In: *Joule* 5.11 (2021), pp. 2823–2844. ISSN: 2542-4351. DOI: <https://doi.org/10.1016/j.joule.2021.09.016>. URL: <https://www.sciencedirect.com/science/article/pii/S254243512100444X>.
- [28] U.S. Geological Survey. "Fluorspar". In: *Mineral Commodity Summaries* (2023). DOI: <https://pubs.usgs.gov/periodicals/mcs2023/mcs2023-fluorspar.pdf>.
- [29] Irshad Mohammad et al. "Room-Temperature, Rechargeable Solid-State Fluoride-Ion Batteries". In: *ACS Applied Energy Materials* 1.9 (Aug. 2018), pp. 4766–4775. DOI: 10.1021/acsaem.8b00864. URL: <https://doi.org/10.1021/acsaem.8b00864>.
- [30] Saeed Shafiei Kaleibari, Qiang Ye, and Meng Ni. "Towards the high energy density batteries via fluoride ions shuttling in liquid electrolytes: A review". In: *International Journal of Energy Research* 46.13 (Aug. 2022), pp. 17848–17872. DOI: 10.1002/er.8468. URL: <https://doi.org/10.1002/er.8468>.
- [31] F Gschwind et al. "Fluoride ion batteries: Theoretical performance, safety, toxicity, and a combinatorial screening of new electrodes". In: *Journal of Fluorine Chemistry* 182 (2016), pp. 76–90.
- [32] Mohammad Ali Nowroozi et al. "LaSrMnO₄: reversible electrochemical intercalation of fluoride ions in the context of fluoride ion batteries". In: *Chemistry of Materials* 29.8 (2017), pp. 3441–3453.
- [33] Hiroyuki Nakano et al. "Fluoride-ion shuttle battery with high volumetric energy density". In: *Chemistry of Materials* 33.1 (2020), pp. 459–466.
- [34] Yongqiang Shen et al. "A reversible conversion and intercalation reaction material for Li ion battery cathode". In: *Materials Letters* 180 (2016), pp. 260–263.
- [35] Jun Haruyama et al. "Two-phase reaction mechanism for fluorination and defluorination in fluoride-shuttle batteries: a first-principles study". In: *ACS applied materials & interfaces* 12.1 (2019), pp. 428–435.
- [36] Mohammad Ali Nowroozi et al. "LaSrMnO₄: reversible electrochemical intercalation of fluoride ions in the context of fluoride ion batteries". In: *Chemistry of Materials* 29.8 (2017), pp. 3441–3453.

- [37] Oliver Clemens et al. "Electrochemical fluorination of perovskite type BaFeO 2.5". In: *Dalton Transactions* 43.42 (2014), pp. 15771–15778.
- [38] Mohammad Ali Nowroozi et al. "La₂CoO₄: a new intercalation based cathode material for fluoride ion batteries with improved cycling stability". In: *Journal of Materials Chemistry A* 6.11 (2018), pp. 4658–4669.
- [39] Mohammad Ali Nowroozi et al. "High cycle life all-solid-state fluoride ion battery with La₂NiO₄+ d high voltage cathode". In: *Communications Materials* 1.1 (2020), p. 27.
- [40] Yanchang Wang et al. "Anion substitution at apical sites of Ruddlesden–Popper-type cathodes toward high power density for all-solid-state fluoride-ion batteries". In: *Chemistry of Materials* 34.2 (2022), pp. 609–616.
- [41] Nicholas H Bashian et al. "Electrochemical oxidative fluorination of an oxide perovskite". In: *Chemistry of Materials* 33.14 (2021), pp. 5757–5768.
- [42] Wasif Zaheer et al. "Reversible room-temperature fluoride-ion insertion in a tunnel-structured transition metal oxide host". In: *ACS Energy Letters* 5.8 (2020), pp. 2520–2526.
- [43] Jessica L Andrews et al. "Room-Temperature Electrochemical Fluoride (De) insertion into CsMnFeF₆". In: *ACS Energy Letters* 7.7 (2022), pp. 2340–2348.
- [44] Xiao-Yong Yang, Wei Luo, and Rajeev Ahuja. "Fluoride ion batteries: Designing flexible M₂CH₂ (M= Ti or V) MXenes as high-capacity cathode materials". In: *Nano Energy* 74 (2020), p. 104911.
- [45] Antonin Grenier et al. "Electrochemical reactions in fluoride-ion batteries: mechanistic insights from pair distribution function analysis". In: *Journal of Materials Chemistry A* 5.30 (2017), pp. 15700–15705.
- [46] Hiroaki Konishi et al. "Improvement of cycling performance in bismuth fluoride electrodes by controlling electrolyte composition in fluoride shuttle batteries". In: *Journal of Applied Electrochemistry* 48 (2018), pp. 1205–1211.
- [47] Zishuai Zhang et al. "Aqueous rechargeable dual-ion battery based on fluoride ion and sodium ion electrochemistry". In: *Journal of Materials Chemistry A* 6.18 (2018), pp. 8244–8250.
- [48] Xianhua Hou et al. "An aqueous rechargeable fluoride ion battery with dual fluoride electrodes". In: *Journal of The Electrochemical Society* 166.12 (2019), A2419.
- [49] Hiroaki Konishi et al. "Improved electrochemical performances in a bismuth fluoride electrode prepared using a high energy ball mill with carbon for fluoride shuttle batteries". In: *Journal of Electroanalytical Chemistry* 839 (2019), pp. 173–176.
- [50] Hiroaki Konishi et al. "Reversible electrochemical reaction of a fluoride shuttle battery with a bismuth (III) fluoride electrode and electrolyte containing Triphenylboroxine as an anion acceptor". In: *ChemistrySelect* 5.21 (2020), pp. 6237–6241.
- [51] Tsuyoshi Takami et al. "A new Bi_{0.7}Fe_{1.3}O_{1.5}F_{1.7} phase: Crystal structure, magnetic properties, and cathode performance in fluoride-ion batteries". In: *APL Materials* 8.5 (2020), p. 051103.
- [52] Martin Wilkening et al. "Structure and ion dynamics of mechanosynthesized oxides and fluorides". In: *Zeitschrift für Kristallographie - Crystalline Materials* 232.1-3 (Sept. 2016), pp. 107–127. DOI: 10.1515/zkri-2016-1963. URL: <https://doi.org/10.1515/zkri-2016-1963>.
- [53] L.N. Patro. "Role of mechanical milling on the synthesis and ionic transport properties of fast fluoride ion conducting materials". In: *Journal of Solid State Electrochemistry* 24.10 (July 2020), pp. 2219–2232. DOI: 10.1007/s10008-020-04769-x. URL: <https://doi.org/10.1007/s10008-020-04769-x>.
- [54] Anubhav Jain et al. "Commentary: The Materials Project: A materials genome approach to accelerating materials innovation". In: *APL Materials* 1.1 (July 2013), p. 011002. DOI: 10.1063/1.4812323. URL: <https://doi.org/10.1063/1.4812323>.
- [55] I. Minkoff. "Applications of the scanning electron microscope in materials science". In: *Journal of Materials Science* 2.4 (July 1967), pp. 388–394. DOI: 10.1007/bf00572424. URL: <https://doi.org/10.1007/bf00572424>.

- [56] Serena Carrara. "Towards new efficient nanostructured hybrid materials for ECL applications". PhD thesis. Apr. 2017.
- [57] Dale E. Newbury and Nicholas W. M. Ritchie. "Elemental mapping of microstructures by scanning electron microscopy-energy dispersive X-ray spectrometry (SEM-EDS): extraordinary advances with the silicon drift detector (SDD)". In: *Journal of Analytical Atomic Spectrometry* 28.7 (2013), p. 973. DOI: 10.1039/c3ja50026h. URL: <https://doi.org/10.1039.c3ja50026h>.
- [58] Jingru Zhai et al. "MXene enabled binder-free FeOF cathode with high volumetric and gravimetric capacities for flexible lithium ion batteries". In: *Electrochimica Acta* 423 (2022), p. 140595.
- [59] Jian Zhu and Da Deng. "Wet-Chemical Synthesis of Phase-Pure FeOF Nanorods as High-Capacity Cathodes for Sodium-Ion Batteries". In: *Angewandte Chemie International Edition* 54.10 (Jan. 2015), pp. 3079–3083. DOI: 10.1002/anie.201410572. URL: <https://doi.org/10.1002/anie.201410572>.
- [60] Pooja Vadhva et al. "Electrochemical Impedance Spectroscopy for All-Solid-State Batteries: Theory, Methods and Future Outlook". In: *ChemElectroChem* 8.11 (May 2021), pp. 1930–1947. DOI: 10.1002/ce1c.202100108. URL: <https://doi.org/10.1002/ce1c.202100108>.
- [61] Antonin Grenier et al. "Electrochemical reactions in fluoride-ion batteries: mechanistic insights from pair distribution function analysis". In: *Journal of Materials Chemistry A* 5.30 (2017), pp. 15700–15705. DOI: 10.1039/c7ta04005a. URL: <https://doi.org/10.1039/c7ta04005a>.
- [62] Hayat Khan et al. "Experimental methods in chemical engineering: X-ray diffraction spectroscopy—XRD". In: *The Canadian Journal of Chemical Engineering* 98.6 (Apr. 2020), pp. 1255–1266. DOI: 10.1002/cjce.23747. URL: <https://doi.org/10.1002/cjce.23747>.
- [63] Asif Ali, Yi Wai Chiang, and Rafael M. Santos. "X-ray Diffraction Techniques for Mineral Characterization: A Review for Engineers of the Fundamentals, Applications, and Research Directions". In: *Minerals* 12.2 (Feb. 2022), p. 205. DOI: 10.3390/min12020205. URL: <https://doi.org/10.3390/min12020205>.
- [64] Parakevi Kesapidou. *CsPbKF3 solid state electrolyte for Fluoride ion batteries: Synthesis and characterisation*. Tech. rep. TUDelft, 2023.
- [65] Li Zhi-feng et al. "High-efficiency reduction behavior for the oxide scale formed on hot-rolled steel in a mixed atmosphere of hydrogen and argon". In: *Journal of Materials Science* 55 (Feb. 2020). DOI: 10.1007/s10853-019-04027-0.
- [66] Paul L. Günther and Hildegard Rehaag. "Über Die thermische Zersetzung von Oxalaten II. Mitteilung. Darstellung von reinem Ferrooxyd". In: *Zeitschrift für anorganische und allgemeine Chemie* 243.1 (Nov. 1939), pp. 60–68. DOI: 10.1002/zaac.19392430106. URL: <https://doi.org/10.1002/zaac.19392430106>.
- [67] Thomas Scheiber et al. "Fluoride ion dynamics in nanocrystalline PbF₂: On the tremendous impact of structural disorder on F⁻ anion hopping in poor ion conductors". In: *Solid State Ionics* 387 (Dec. 2022), p. 116077. DOI: 10.1016/j.ssi.2022.116077. URL: <https://doi.org/10.1016/j.ssi.2022.116077>.
- [68] Ayuko Kitajou et al. "Synthesis of FeOF using roll-quenching method and the cathode properties for lithium-ion battery". In: *Journal of Power Sources* 243 (Dec. 2013), pp. 494–498. DOI: 10.1016/j.jpowsour.2013.06.053. URL: <https://doi.org/10.1016/j.jpowsour.2013.06.053>.
- [69] Riccardo Maddalena, Christopher Hall, and Andrea Hamilton. "Effect of silica particle size on the formation of calcium silicate hydrate [C-S-H] using thermal analysis". In: *Thermochimica Acta* 672 (Feb. 2019), pp. 142–149. DOI: 10.1016/j.tca.2018.09.003. URL: <https://doi.org/10.1016/j.tca.2018.09.003>.
- [70] Chuan-Fu Lin et al. "Highly Reversible Conversion-Type FeOF Composite Electrode with Extended Lithium Insertion by Atomic Layer Deposition LiPON Protection". In: *Chemistry of Materials* 29.20 (Oct. 2017), pp. 8780–8791. DOI: 10.1021/acs.chemmater.7b03058. URL: <https://doi.org/10.1021/acs.chemmater.7b03058>.

A

Extra Data

A.1. PK10 data

$\text{CsPb}_{1-x}\text{K}_x\text{F}_{3-x}$	Lattice parameter Å	Potassium Content (x)	χ^2
Literature PK00	4.79807	0.00	-
Literature PK10	4.79407	0.10	-
Batch 1	4.79315	0.089	13.6
Batch 2	4.79191	0.066	3.4
Batch 3	4.79607	0.009	3.4
Batch 4	4.79236	0.087	6.6
Batch 5	No measurement	-	-
Batch 6	4.79656	0.070	18.7

Table A.1: Rietveld refinement results of the synthesised $\text{CsPb}_{1-x}\text{K}_x\text{F}_{3-x}$ batches, excluding batch 5, no measurement was taken. Batch 1 was obtained from an earlier project.

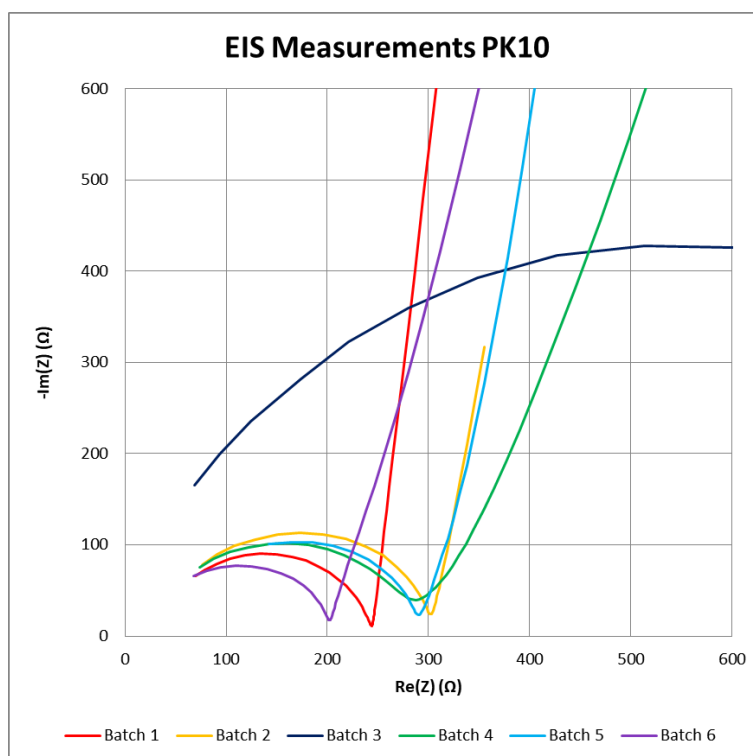


Figure A.1: Measured Nyquist plots of the PK10 measurements. The x-axis is the real impedance, the y-axis the imaginary impedance

A.2. FeO Precursor Data

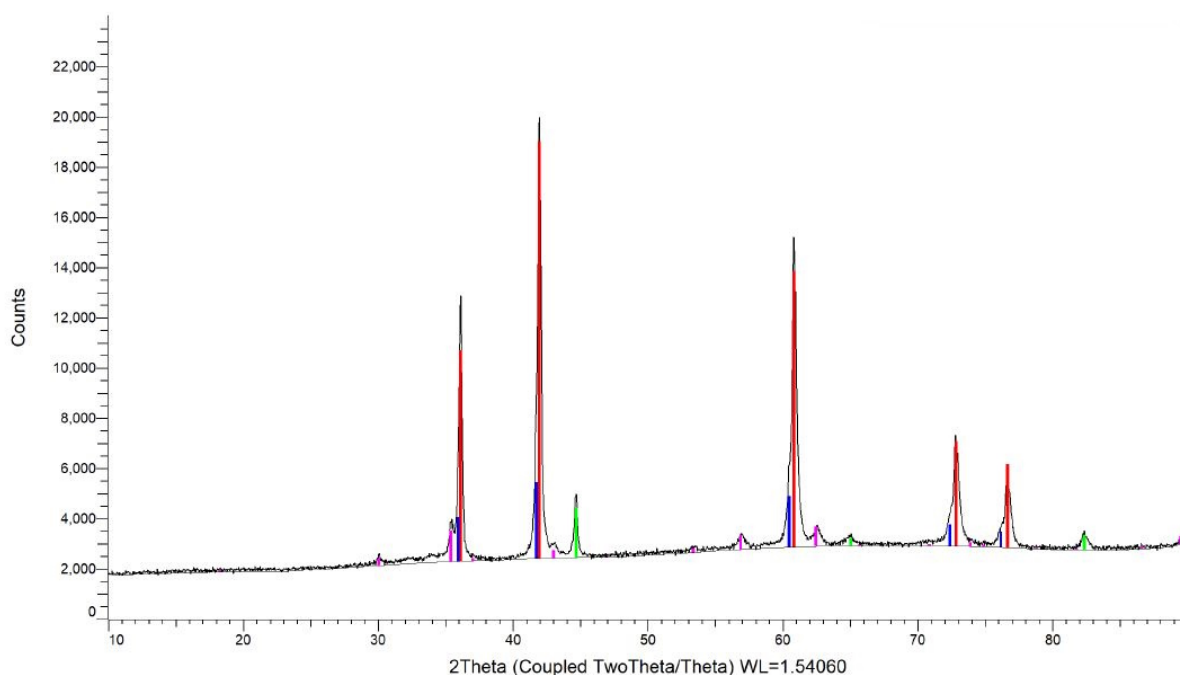


Figure A.2: X-ray diffraction measurement of FeO, obtained from Thermo Fisher using a Bruker diffractometer. Red bars indicate $\text{Fe}_{0.91}\text{O}$, blue bars FeO, green bars α -iron and purple Fe_3O_4 .

The X-ray diffraction measurement on the Bruker diffractometer yielded significantly different results. According to those measurements the sample contains FeO, Fe and Fe_3O_4 in a ratio of 91:4:5. However, as refinement is not possible, the other measurement will be taken as standard for all tests.

A.3. Pb/PbF₂ symmetric cells

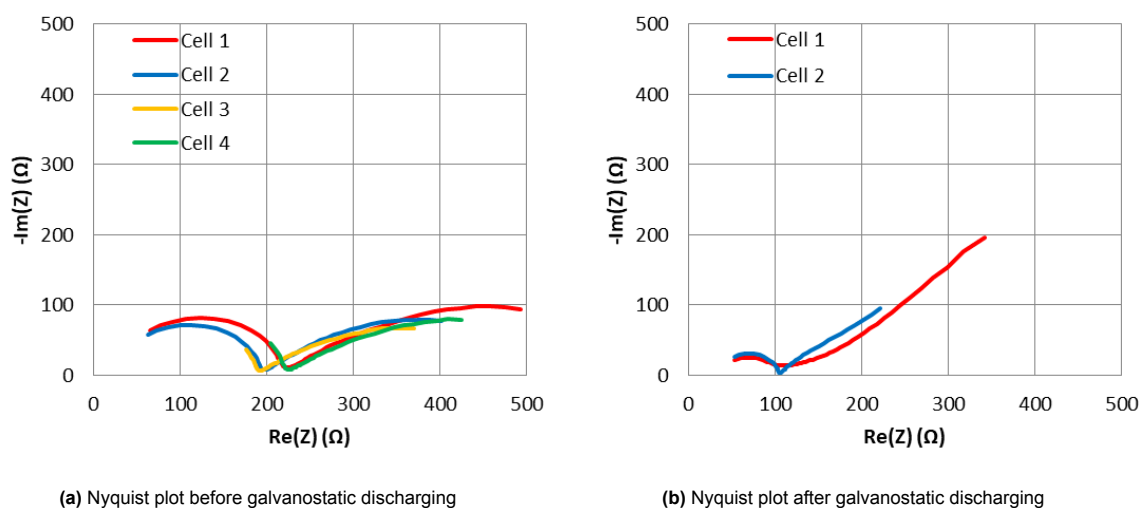


Figure A.3: Impedance measurements of Pb/PbF₂:PK10:Pb/PbF₂ cell. a) Impedance before galvanostatic discharging. b) Impedance after galvanostatic discharging.

The initial impedance measurements do not show any anomalies for both cells. An up to 10% deviation is an accepted inaccuracy, and this is dependent on the thickness of the pellet, and the thickness of

the electrolyte layer within the pellet. The resistance is slightly higher compared to the earlier PK10 impedance measurements. This is due to the cathode and anode also contributing to the overall thickness. The second impedance measurement for cell 1 and 2 exhibit interesting behaviour. Cell 1 has a blend between the first and second semicircle, indicating that several processes happen in the same frequency range. In this case it seems that the second semicircle, the charge/mass transfer resistance, has become spread out. The bulk resistance in both cells has significantly reduced, practically halved. The behaviour of cell 2 has a very clear 45° Warburg impedance part after $Z = 100\Omega$. In figure A.3b, the second impedance measurements of cell 3 and 4 have been omitted due to a procedural lapse occurring, resulting in the inadvertent exclusion of the impedance measurements for these cells.

A.4. PK10 Performance

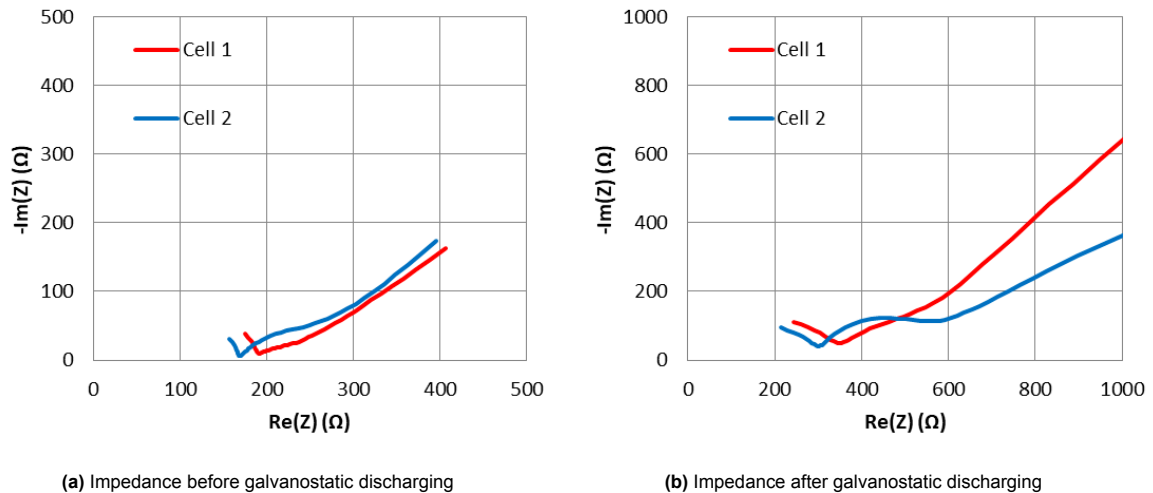


Figure A.4: Impedance measurements of ECC:PK10:Pb/PbF₂ cell

The impedance measurements before discharge figure A.4a indicate that cell 1 already had a slightly worse ionic conductivity, and a larger charge/mass transfer resistance compared to cell 2. This can indicate that either the electrolyte layer is thicker or inconsistent in cell 1, or a worse contact between the different internal interfaces, leading to a higher internal resistance. Inhomogeneity in the electrode distribution can also cause the second semicircle to manifest itself before the first one is properly finished. This effect is even stronger in the impedance measurement after galvanostatic discharging, figure A.4b.

B

Experimental Method

B.1. Electrolyte

Electrolyte Name	PK10 EK-100-02	PK10 PBR-004-02	PK01 PBR-004-03	PK10 PBR-004-04	PK10 PBR-004-05	PK10 PBR-004-06
Date Created	01/01/2023	03/04/2023	03/04/2023	11/04/2023	11/04/2023	14/06/2023
CsF	1481.0 mg	1516.8 mg	1524.4 mg	1469.3 mg	1492.4 mg	1482.3 mg
Weighted	1481.0 mg	1519.5 mg	1515.1 mg	1488.0 mg	1498.5 mg	1489.1 mg
Loss		2.7 mg	-9.3 mg	18.7 mg	6.1 mg	6.8 mg
PbF2	2139.0 mg	2199.5 mg	2204.4 mg	2150.0 mg	2161.8 mg	2154.1 mg
Weighted	2139.0 mg	2213.0 mg	2209.8 mg	2162.0 mg	2164.2 mg	2162.2 mg
Loss		13.5 mg	5.4 mg	12.0 mg	2.4 mg	8.1 mg
KF	56.0 mg	58.0 mg	5.9 mg	55.9 mg	58.3 mg	65.9 mg
Weighted	56.0 mg	58.0 mg	5.9 mg	57.3 mg	60.0 mg	67.0 mg
Loss	0.0 mg	0.0 mg	0.0 mg	1.4 mg	1.7 mg	1.1 mg
Total	3676.0 mg	3774.3 mg	3734.7 mg	3675.2 mg	3712.5 mg	3702.3 mg
Weighted	2000.0 mg	2900.0 mg	2900.0 mg	3153.0 mg	3179.9 mg	3304.0 mg
Loss	1676.0 mg	874.3 mg	834.7 mg	522.2 mg	532.6 mg	398.3 mg
Pellet (avg.)	0.601 mm	0.602 mm	0.493 mm	0.505 mm	0.569 mm	0.570 mm
M1	0.601	0.594	0.484	0.52	0.608	0.577
M2		0.588	0.494	0.505	0.525	0.538
M3		0.58	0.501	0.488	0.53	0.566
M4		0.645		0.503	0.593	0.555
M5				0.508	0.587	0.615
Impedance	212	305	1020	287	290	202
Conductivity	0.36 mS/cm	0.25 mS/cm	0.06 mS/cm	0.22 mS/cm	0.25 mS/cm	0.36 mS/cm
Notes		Extra KF added				

B.2. FeO Composite

Composite Name	FeO Cath PBR-100-01	FeO Cath PBR-100-02	FeO Cath PBR-100-03	FeO Cath PBR-100-04
Specific capacity (mAh/mg) Date Created	0.11 mAh/mg 10/01/2023	0.11 mAh/mg 06/04/2023	0.11 mAh/mg 04/05/2023	0.11 mAh/mg 04/05/2023
FeO Weighted Loss Name	27.7 mg 28.4 mg 0.7 mg PBR-003-01	161.8 mg 162.3 mg 0.5 mg PBR-003-02	81.7 mg 82.1 mg 0.4 mg PBR-008-01	221.8 mg 222.0 mg 0.2 mg PBR-003-02
C-tubes Weighted Loss	9.1 mg 9.5 mg 0.4 mg	53.6 mg 53.8 mg 0.2 mg	26.5 mg 27.1 mg 0.6 mg	74.0 mg 74.0 mg 0.0 mg
Electrolyte Weighted Loss Name	53.8 mg 54.1 mg 0.3 mg EK-100-02	321.7 mg 321.9 mg 0.2 mg PBR-004-02	161.5 mg 162.1 mg 0.6 mg PBR-004-05	444.0 mg 444.3 mg 0.3 mg PBR-004-05
Total Weighted Loss	90.6 mg 84.3 mg 6.3 mg	537.1 mg 531.6 mg 5.5 mg	269.7 mg 248.4 mg 21.3 mg	739.8 mg 546.0 mg 193.8 mg

B.3. Pb/PbF₂ Composite

Composite Name	PbF₂ An PBR-300-01	PbF₂ An PBR-300-02	PbF₂ An PBR-300-03
Specific capacity (mAh/mg) Date Created	0.03 mAh/mg 10/01/2023	0.03 mAh/mg 05/04/2023	0.03 mAh/mg 21/04/2023
PbF ₂ Weighted Loss Name	46.2 mg 46.3 mg 0.1 mg PBR-001-01	122.6 mg 123.8 mg 1.2 mg PBR-001-02	122.1 mg 123.6 mg 1.5 mg PBR-001-03
Pb Weighted Loss Name	45.8 mg 46.5 mg 0.7 mg PBR-002-01	120.4 mg 122.5 mg 2.1 mg PBR-002-01	122.7 mg 123.0 mg 0.3 mg PBR-002-01
C-tubes Weighted Loss Name	30.7 mg 31.3 mg 0.6 mg PBR-005-01	81.2 mg 81.3 mg 0.1 mg PBR-005-01	81.3 mg 82.0 mg 0.7 mg PBR-005-02
Electrolyte Weighted Loss Name	184.1 mg 184.2 mg 0.1 mg EK-100-02	487.4 mg 487.5 mg 0.1 mg PBR-004-02	494.0 mg 496.0 mg 2.0 mg PBR-004-04
Total Weighted Loss	306.8 mg 295.1 mg 11.7 mg	811.6 mg 787.5 mg 24.1 mg	820.1 mg 803.0 mg 17.1 mg

B.4. FeOF Composite

Composite Name	FeOF cath PBR-200-01
Specific capacity (mAh/mg)	0.03 mAh/mg
Date Created	10/06/2023
FeOF	16.0 mg
Weighted	16.1 mg
Loss	0.1 mg
Name	PBR-006-03
C-tubes	4.9 mg
Weighted	5.2 mg
Loss	0.3 mg
Name	PBR-005-01
Electrolyte	30.5 mg
Weighted	30.9 mg
Loss	0.4 mg
Name	PBR-004-06
Total	51.4 mg
Weighted	48.3 mg
Loss	3.1 mg

B.5. Symmetrical Cells

Cell Name	PbF2/PbF2 PBR-4000-01	PbF2/PbF2 PBR-4000-02	PbF2/PbF2 PBR-4000-04	PbF2/PbF2 PBR-4000-05
Capacity (mAh)	0.962 mAh	1.018 mAh	1.046 mAh	1.018 mAh
Date Created	18/04/2023	18/04/2023	07/05/2023	07/05/2023
Active Material Cath	4.6 mg	4.7 mg	4.8 mg	4.7 mg
Top	30.5 mg	31.4 mg	31.9 mg	31.8 mg
Weighted	31.0 mg	31.4 mg	32.2 mg	32.3 mg
Loss	0.5 mg	0.0 mg	0.3 mg	0.5 mg
Name	PBR-300-02	PBR-300-02	PBR-300-03	PBR-300-03
Electrolyte	215.1 mg	202.1 mg	199.8 mg	199.1 mg
Weighted	215.6 mg	202.6 mg	202.8 mg	200.7 mg
Loss	0.5 mg	0.5 mg	3.0 mg	1.6 mg
Name	PBR-004-04	PBR-004-04	PBR-004-06	PBR-004-06
Active Material An	4.4 mg	4.5 mg	4.8 mg	4.7 mg
Bottom	29.2 mg	30.1 mg	32.0 mg	31.3 mg
Weighted	29.2 mg	30.9 mg	34.0 mg	32.0 mg
Loss	0.0 mg	0.8 mg	2.0 mg	0.7 mg
Name	PBR-300-02	PBR-300-02	PBR-300-03	PBR-300-03
Cathode cap	1.004 mAh	1.034 mAh	1.046 mAh	1.018 mAh
Anode cap	0.962 mAh	1.018 mAh	1.046 mAh	1.018 mAh

B.6. FeO Cells

Cell Name	FeO 1 PBR-8000-01	FeO 2 PBR-8000-02
Capacity (mAh)	0.89	1.05
Date Created	12/06/23	12/06/23
Shown Capacity	0.02%	
Active Material Cath	FeO	FeO
Top	7.9 mg	9.3 mg
Weighted	9.2 mg	9.7 mg
Loss	1.3 mg	0.4 mg
Name	PBR-100-04	PBR-100-04
Electrolye	204.5 mg	201.8 mg
Weighted	206.5 mg	203.0 mg
Loss	2.0 mg	1.2 mg
Name	PBR-004-06	PBR-004-06
Active Material An	PbF ₂	PbF ₂
Bottom	57.1 mg	59.5 mg
Weighted	61.2 mg	61.3 mg
Loss	4.1 mg	1.8 mg
Name	PBR-300-03	PBR-300-03
Cathode cap	0.89	1.05
Anode cap	1.87	1.94

B.7. FeOF Cells

Cell Name	FeOF/PbF2 PBR-9000-01	FeOF/PbF2 PBR-9000-02
Capacity (mAh)	1.09 mAh	1.09 mAh
Date Created	18/04/2023	18/04/2023
Active Material Cath	2.2 mg	2.2 mg
Top	7.3 mg	7.3 mg
Weighted	7.8 mg	8.5 mg
Loss	0.5 mg	1.2 mg
Name	PBR-300-02	PBR-300-02
Electrolye	203.1 mg	206.4 mg
Weighted	204.1 mg	211.0 mg
Loss	1.0 mg	4.6 mg
Name	PBR-004-04	PBR-004-04
Active Material An	mg	mg
Bottom	49.1 mg	54.0 mg
Weighted	50.2 mg	59.3 mg
Loss	1.1 mg	5.3 mg
Name	PBR-300-02	PBR-300-02
Cathode cap	1.09 mAh	1.09 mAh
Anode cap	1.60 mAh	1.76 mAh